



저작자표시-비영리-변경금지 2.0 대한민국

이용자는 아래의 조건을 따르는 경우에 한하여 자유롭게

- 이 저작물을 복제, 배포, 전송, 전시, 공연 및 방송할 수 있습니다.

다음과 같은 조건을 따라야 합니다:



저작자표시. 귀하는 원저작자를 표시하여야 합니다.



비영리. 귀하는 이 저작물을 영리 목적으로 이용할 수 없습니다.



변경금지. 귀하는 이 저작물을 개작, 변형 또는 가공할 수 없습니다.

- 귀하는, 이 저작물의 재이용이나 배포의 경우, 이 저작물에 적용된 이용허락조건을 명확하게 나타내어야 합니다.
- 저작권자로부터 별도의 허가를 받으면 이러한 조건들은 적용되지 않습니다.

저작권법에 따른 이용자의 권리는 위의 내용에 의하여 영향을 받지 않습니다.

이것은 [이용허락규약\(Legal Code\)](#)을 이해하기 쉽게 요약한 것입니다.

[Disclaimer](#)

A THESIS  
FOR THE DEGREE OF DOCTOR OF PHILOSOPHY

# **Development of Piezoelectric Barium Titanate Nanoparticles based Smart Biosensing Systems**



SOPHIA SELVARAJAN

Department of Advanced Convergence Technology and Science

GRADUATE SCHOOL  
JEJU NATIONAL UNIVERSITY

February 2018

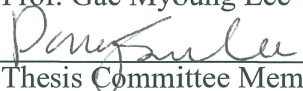
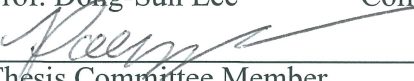
# Development of Piezoelectric Barium Titanate Nanoparticles based Smart Biosensing Systems

**SOPHIA SELVARAJAN**

(Supervised by Professor Sang Jae Kim)

A thesis submitted in partial fulfillment of the requirement for the degree of  
Doctor of Philosophy  
2017.12

The thesis has been examined and approved.

 Thesis Director, Prof. Gae Myoung Lee	Professor, Department of Electrical Engineering, College of Engineering, Jeju National University
 Thesis Committee Member, Prof. Dong-Sun Lee	Professor, Department of Biomaterials College of Applied Life Sciences, Jeju National University
 Thesis Committee Member, Prof. Dong-Guk Paeng	Professor, Department of Ocean System Engineering, College of Ocean Sciences, Jeju National University
 Thesis Committee Member, Dr. K. Karthikeyan	Research Professor, Department of Mechatronics Engineering, College of Engineering, Jeju National University
 Thesis Committee Member, Prof. Sang-Jae Kim	Professor, Department of Mechatronics Engineering, College of Engineering, Jeju National University

December, 2017

**Department of Advanced Convergence Technology and Science  
GRADUATE SCHOOL  
JEJU NATIONAL UNIVERSITY  
Republic Korea**

## **Acknowledgements**

*First and foremost, I am grateful to the God for the good health and wellbeing that were necessary to complete this thesis.*

*I would like to thank my advisor Prof. Sang-Jae Kim for accepting nothing less than excellence from me. I am always grateful for his continuous support of my Ph.D study and related research, for his patience, motivation, and immense knowledge. His guidance helped me in all the time of research and writing of this thesis.*

*Besides my advisor, I would like to thank the rest of my well-wishers, professors here as well as back at my home country for their insightful comments and encouragement.*

*I thank my fellow lab mates for the stimulating discussions, for the sleepless nights we were working together before deadlines, and for all the fun we have had in the last three and a half years.*

*Most importantly, none of this could have happened without my family, who offered their encouragement through phone calls and messages each day despite my own limited devotion to correspondence. To my parents, sister and my spouse it would be an understatement to say that, as a family, you have been my foundation. Every time I was ready to quit, you did not let me and I am forever grateful. This dissertation stands as a testament to your unconditional love and encouragement.*

**SOPHIA SELVARAJAN**

# Thesis overview

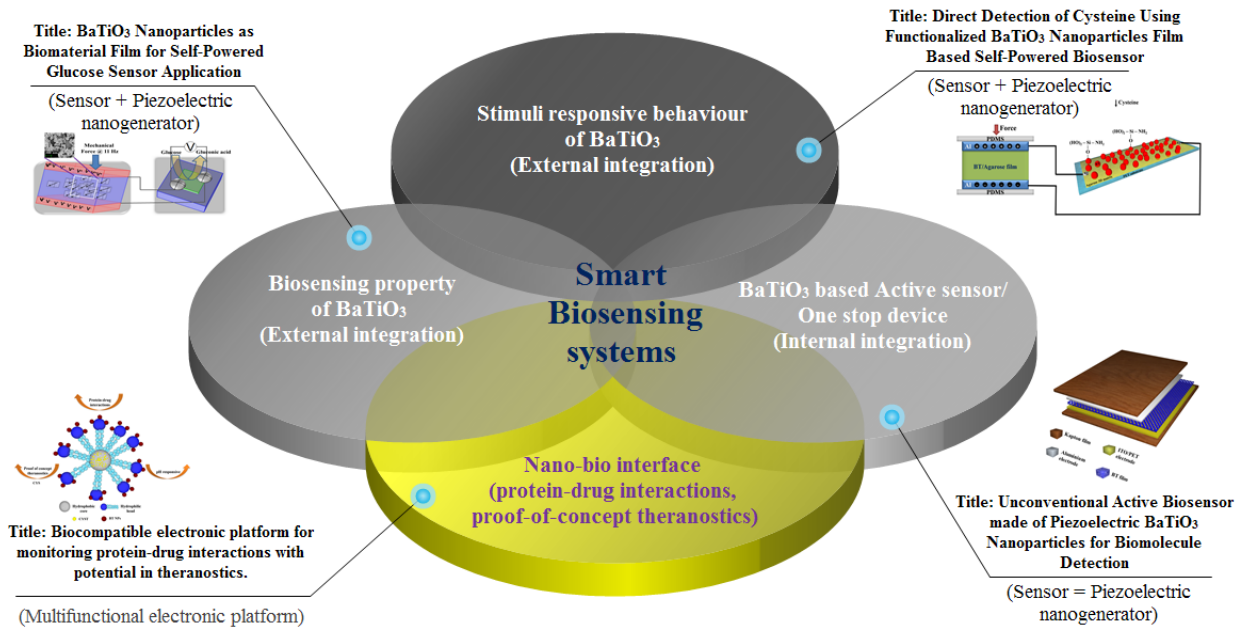


# Table of contents

<b>Contents</b>	<b>i</b>
<b>Nomenclature</b>	<b>vi</b>
<b>List of Tables</b>	<b>vii</b>
<b>List of Figures</b>	<b>viii</b>
<b>Abstract – Hangul</b>	<b>xvi</b>
<b>Abstract</b>	<b>xx</b>
<b>CHAPTER I: Introduction</b>	
1.1. Background	1
1.2. Biosensors	3
1.3. Properties of Barium titanate (BaTiO <sub>3</sub> )	6
1.4. Piezoelectric nanogenerators	9
1.5. Self-powered systems	10
1.6. Research objectives/ scope of thesis	14
1.7. Structure of this thesis	15
1.8. References	18
<b>CHAPTER II: Materials and characterization techniques</b>	
2.1. Chemicals	21
2.2. Synthesis method	21
2.2.1. Solid state reaction	22
2.2.2. Hydrothermal synthesis	22
2.2.3. Functionalization of nanoparticles	24
2.3. Characterization techniques	24

2.3.1. X-ray diffraction (XRD)	24
2.3.2. Raman spectroscopy	25
2.3.3. Fourier transform infrared (FT-IR) spectrometer	25
2.3.4. Field-emission scanning electron microscopy	26
2.3.5. High-resolution transmission electron microscopy	26
2.3.6. X-ray photoelectron spectroscopy (XPS)	26
2.3.7. UV-Vis spectrophotometer (UV-Vis)	27
2.3.8. Frequency variable CV-IV System	27
2.3.9. Linear motor	27

### **CHAPTER III: BaTiO<sub>3</sub> Nanoparticles as Biomaterial Film for Self-Powered Glucose Sensor Application**

3.1. Introduction	29
3.2. Experimental section	32
3.2.1 Synthesis of BaTiO <sub>3</sub> Nanoparticles	32
3.2.2. Fabrication of BaTiO <sub>3</sub> NP's film based glucose sensor	32
3.2.3 Fabrication of piezoelectric nanogenerator (PNG)	33
3.2.4 Characterization and measurement	34
3.3. Results and discussion	35
3.3.1. BTO NP's film based sensor's structural characterization	35
3.3.2. I-V characterization for glucose measurement	38
3.3.3 Proposed working mechanism of BTO NP's film based sensor	40
3.3.4. I-T characteristics of the sensor	43
3.3.5. Interference and real sample analysis	45
3.3.6. Working mechanism of PNG	47

3.3.7. Integration of PNG and glucose sensor	50
3.4. Conclusions	55
3.5. References	56
<b>CHAPTER IV: Direct Detection of Cysteine Using Functionalized BaTiO<sub>3</sub> Nanoparticles Film Based Self-Powered Biosensor</b>	
4.1. Introduction	63
4.2. Experimental section	65
4.2.1. Synthesis of BT NPs	65
4.2.2. NH <sub>2</sub> functionalization of BT NPs	66
4.2.3. Fabrication of the cysteine sensor	67
4.2.4. Fabrication of the BT/Ag PNG	68
4.2.5. Instrumentation	69
4.3. Results and discussion	70
4.3.1. Structural characterisation	70
4.3.2. Device characterisation and investigation of its sensing feasibility	74
4.3.3. Cysteine detection by an I–V technique	77
4.3.4. Proposed working mechanism of the Ag/BT-NH <sub>2</sub> film-based cysteine sensor	79
4.3.5. Real-time analysis and interference studies	81
4.3.6. BT/Ag PNG	85
4.3.7. Working mechanism of PNG	86
4.3.8. Integration of the cysteine sensor and BT/Ag PNG	89

4.4. Conclusions	90
4.5. References	91

**CHAPTER V: Unconventional Active Biosensor made of Piezoelectric BaTiO<sub>3</sub> Nanoparticles for Biomolecule Detection**

5.1. Introduction	96
5.2. Experimental section	98
5.2.1. Synthesis of BT NPs	98
5.2.2. Fabrication of Al/BT/ITO NG	99
5.2.3. Instrumentation	100
5.3. Results and discussion	101
5.3.1. Structural characterization	101
5.3.2. NG device optimization and characterization	103
5.3.3. Self-powered/ active glucose sensor	109
5.3.4. Proposed working mechanism of Al/BT/ITO NG as active glucose biosensor	114
5.3.5. Interference studies	117
5.4. Conclusions	118
5.5. References	119

**CHAPTER VI: Biocompatible electronic platform for monitoring protein-drug interactions and proof-of-concept theranostics.**

6.1. Introduction	126
6.2. Experimental section	128
6.2.1. BT NPs synthesis	128
6.2.2. Functionalization of BT NPs with NH <sub>2</sub> group	129

6.2.3. Casein micelle preparation	129
6.2.4. Preparation of Cysteamine (CYST) drug solution	129
6.2.5. Preparation of conjugates	129
6.2.6. Fabrication of CAS film based devices	130
6.2.7. Fabrication of PNGs (Piezoelectric Nanogenerators)	130
6.2.8. Instrumentation	131
6.3. Results and discussion	132
6.3.1. Structural characterization and spectroscopic confirmation of bioconjugate formation	132
6.3.2. pHstimuli-responsive studies	140
6.3.2. Protein-drug interactions through <i>I-V</i> characteristics	142
6.3.4. Proof of concept theranostic platform	146
6.3.5. Piezoelectric response of PNGs for self-powered applications	148
6.4. Conclusions	151
6.5. References	152
<b>CHAPTER VII: Conclusions and Future Outlook</b>	
7.1 Conclusions	158
7.2. Suggestions for future work	161
<b>APPENDIX A: List of Publications</b>	164
<b>APPENDIX B: Conference Presentations</b>	166

## Nomenclature

AA	Ascorbic acid
APTES	(3-aminopropyl) triethoxysilane
Ag	Agarose
BT	Barium Titanate
BT-NH <sub>2</sub>	Amine functionalized Barium Titanate
CAS	Casein micelle
CYST	Cysteamine
CYS	Cysteine
DNA	Deoxyribonucleic acid
FET	Field effect transistors
FT-IR	Fourier transform infrared spectrometer
FESEM	Field-emission scanning electron microscopy
ITO	Indium tin oxide
<i>I-V</i>	Current-voltage
LEDs	Light emitting diodes
LOD	Limit of detection
MEMS	Micro electro mechanical systems
NEMS	Nano electromechanical systems
NPs	Nanoparticles
PNG	Piezoelectric nanogenerators
PVA	Poly vinyl alcohol
PDMS	Polydimethylsiloxane
PZT	Lead zirconium titanate
PVDF	polyvinylidene fluoride
QCM	Quartz crystal microbalance
RNA	Ribonucleic acid
SHG	Second-harmonic generation
SAW	Surface acoustic waves
UV-Vis	UV-Vis spectrophotometer
W/V	weight/volume
(XRD)	X-ray diffractometer

## List of Tables

- Table 3.1. Comparison of analytical parameters of proposed BTO NP's film based glucose sensor with well reported glucose biosensors (different detection techniques) 53
- Table 4.1. Comparison between cysteine sensors based on different detection techniques 88
- Table 5.1 Comparison among glucose sensors based on different detection techniques 113

## List of Figures

Fig. 1.1.	Overview of smart biomedical devices	2
Fig. 1.2.	Schematic representation of the elements of a typical biosensor	3
Fig. 1.3.	Multifunctional properties of Barium titanate ( $\text{BaTiO}_3$ )	6
Fig. 1.4.	Tetragonal crystal structure of Barium Titanate ( $\text{BaTiO}_3$ )	7
Fig. 1.5.	External integration between energy conversion devices and biomedical devices	11
Fig. 1.6.	Power consumption value of generic integrated circuit components and sensors as well as implantable devices	13
Fig 2.1.	Autoclave apparatus used for hydrothermal synthesis	23
Fig. 3.1.	Schematic of BTO NP's film based glucose sensor.	33
Fig. 3.2. (a)	X-ray diffraction patterns of pure crystalline BTO NP's (> 100 nm) and BTO NP's film <i>via</i> PVA matrix. (b) Raman spectrum of pristine BTO NP's and BTO-PVA film (after heat treatment at 150 °C/ 1hr).	
Fig. 3.3.	FE-SEM images of (a) BTO film (cross-sectional view) having thickness ~ 200 $\mu\text{m}$ and (b) Surface morphology of BTO film after heat treatment at 150 °C for 1 hr. (c) Random structured BTO nanoparticles at 1 $\mu\text{m}$ scale. (d) FESEM image of PVA film at 10 $\mu\text{m}$ scale.	37
Fig. 3.4.	Electrical response of BTO NP's film based glucose sensor. (a) I-V characterization of glucose sensor (20 % W/V of BTO NP's) in absence (inset Fig.) and presence of glucose (50 $\mu\text{M}$ to 1 mM) . (b) 3D graphical analysis of sensor's current response under different concentrations of BTO NP's (5, 10, 15, 20 % (W/V)) and glucose.	38
Fig. 3.5.	I-V curves of BTO NP's film based glucose sensor (different weight ratios) under various glucose concentrations ranging from 0 $\mu\text{M}$ to 1000 $\mu\text{M}$ . (a) 5 % (W/V) of BTO NP's film based device (b) 10 % (W/V) of BTO NP's film based device (c) 15 % (W/V) of BTO NP's film based device. (d) 2D graph depicting the correlation between BTO NP's concentration and glucose sensing efficiency with respect to the sensor's current output at a bias voltage of + 4 V for lower (50 $\mu\text{M}$ ) and higher (1000 $\mu\text{M}$ ) glucose concentrations.	40
Fig. 3.6.	Proposed working mechanism (using energy band diagram) of	42

- BTO NP's film based glucose sensor. (a) Energy band diagram in absence of glucose (presented as solid black lines in Fig. 3.6 a and dashed yellow lines in Fig. 3.6 b). (b) Energy band diagram in presence of glucose (presented as solid black lines in Fig. 3.6 b).
- Fig. 3.7. Current-time response of BTO NP's film based glucose sensor at an applied bias voltage of +0.5 V. (a) For lower glucose concentration range (0  $\mu$ M to 30  $\mu$ M) having correlation coefficient of 0.9843. (b) For higher glucose concentration range (50  $\mu$ M to 1000  $\mu$ M) having correlation coefficient of 0.9913. (c) Single calibration plot including two linear fittings for lower and higher glucose concentration ranges (0.1  $\mu$ M – 1000  $\mu$ M). (d) I-T curve for interference study with 5 mM glucose and interferents such as 0.1 mM galactose and 0.1 mM uric acid. (Inset shows the current response of the sensor for human saliva spiked with 100  $\mu$ M of glucose). 44
- Fig. 3.8. Interference study (glucose vs ascorbic acid). I-V curves of BTO NP's film based glucose sensor at a potential window of 0 to +4V under (a) 5 mM glucose (b) 0.1 mM ascorbic acid. (c) Comparative analysis for current response of BTO NP's film based glucose sensor measured at +4V under 5 mM glucose and 0.1mM ascorbic acid. 46
- Fig. 3.9. Electrical response of PNG device. (a) Schematic diagram represents the measurement of PNG device output upon mechanical force of 11N. (b, c) Frequency dependent open circuit voltage and short circuit current of composite PNG device upon the mechanical load (11N). (d) Comparative open circuit voltage of PVDF and PVDF/BTO nanocubes upon on mechanical load (11 N) at a frequency of 21 Hz. 48
- Fig. 3.10. (a) Comparison of short circuit current for PVDF and composite film (PVDF/BTO nanocubes) based PNG devices upon the mechanical force 11 N at a cyclic frequency 21 Hz. (b) Stability test for the composite PNG device during 500 seconds upon the mechanical force 11 N at a cyclic frequency 21 Hz. 50
- Fig. 3.11. (a) Schematic representation of self-powered glucose sensor by establishing parallel connection between the PNG device (BaTiO<sub>3</sub>nanocubes / PVDF film) and BTO NP's film based glucose sensor. The inset shows the BTO nanocubes at 200 nm 51

scale. (b) The open circuit potential drop across glucose sensor was measured as a function of different glucose concentrations (0  $\mu\text{M}$  to 1 mM). (c) The non-linear behavior of self-powered glucose sensor under different glucose concentrations (0  $\mu\text{M}$  to 1 mM).

Fig. 3.12.	Open circuit voltage ( $V_{OC}$ ) of PNG device and self-powered glucose sensor (under 0 $\mu\text{M}$ glucose concentration) upon the mechanical load 11 N at frequency 11 Hz.	54
Figure 4.1.	Schematic illustration of the as-fabricated cysteine sensor.	68
Figure 4.2.	Schematic illustration of the as-fabricated BaTiO <sub>3</sub> /agarose (BT/Ag) nanogenerator.	69
Figure 4.3.	(A) Fourier-transform infrared spectra of BT nanoparticles (NPs) before and after NH <sub>2</sub> functionalization and (B) X-ray diffraction spectra for pristine BT NPs, BT-NH <sub>2</sub> NPs, Ag/BT-NH <sub>2</sub> film, and pristine Ag.	71
Figure 4.4.	Raman spectra for pristine BT NPs, BT-NH <sub>2</sub> NPs, pristine Ag film and Ag/BT-NH <sub>2</sub> film.	71
Figure 4.5.	Scanning electron microscopy images of (A) pristine Ag film, (B) Ag/BT-NH <sub>2</sub> film (inset shows BT-NH <sub>2</sub> NPs of size $\leq 200$ nm), Ag/BT-NH <sub>2</sub> film at (C) 1 $\mu\text{m}$ scale (D) 200 nm scale.	72
Figure 4.6.	FE-SEM images of (A) BT NPs at 200 nm scale, (B) a cross-sectional view of Ag/BT-NH <sub>2</sub> film with a film thickness of $\sim 50$ $\mu\text{m}$ .	73
Figure 4.7.	I-V curves of (A) Ag/BT film based device and (B) Ag film based device under different pH values (pH 7 to 3) at a bias voltage of $\pm 1$ V.	74
Figure 4.8.	I-V curves of Ag/BT-NH <sub>2</sub> film based cysteine sensor under different cysteine concentrations (100 $\mu\text{M}$ to 400 $\mu\text{M}$ ) in (A) presence and (B) absence of UV at $\pm 4$ V.	75
Figure 4.9.	Cysteine detection using a current-voltage ( $I$ - $V$ ) technique. (A) Two-dimensional (2D) graph depicting the performance of a cysteine sensor in the absence and presence of ultraviolet (UV) light (365 nm). (B) Three-dimensional (3D) graphical representation of the cysteine sensor's relative change in current ( $I-I_0/I_0$ ) with respect to BT-NH <sub>2</sub> NP and cysteine concentrations. (C) $I$ - $V$ curves of Ag/BT-NH <sub>2</sub> film-based cysteine sensor (0.2% w/v) in response to various cysteine concentrations (10–1000 $\mu\text{M}$ ). (D) Normalized current value ( $ I-I_0 $ ) of the sensor at $-4$ V	76

- for different cysteine concentrations (10–1000  $\mu\text{M}$ ; calibration plot obtained from  $I$ – $V$  curves).
- Figure 4.10. I– $V$  curves of Ag/BT– $\text{NH}_2$  film based cysteine sensor in presence of different concentrations of (A) PBS buffer and (B) cysteine (100  $\mu\text{M}$  to 400  $\mu\text{M}$ ) (C) Comparison between their relative change in current (%) at –4V. 78
- Figure 4.11. Schematic representation. (A) Proposed mechanism of cysteine detection (B) Reaction scheme for amine functionalization of BT NPs using (3-aminopropyl) triethoxysilane (APTES, a silane coupling agent). 79
- Figure 4.12. Real sample analysis and interference studies. (A)  $I$ – $V$  response of the Ag/BT– $\text{NH}_2$  film-based cysteine sensor in the presence of a urine sample spiked with different cysteine concentrations (10–500  $\mu\text{M}$ ). (B) Normalized current value ( $|I-I_0|$ ) of the sensor at –4 V in the presence of different concentrations of cysteine-spiked urine sample (10–500  $\mu\text{M}$ ; calibration plot obtained from  $I$ – $V$  curves). (C) Current change ratio of cysteine sensor measured at –4 V in 0.1 M PBS (pH 7) with the addition of 1 mM Cys, His, Gln, AA, and UA. 82
- Figure 4.13. Interference study. I– $V$  curves of Ag/BT– $\text{NH}_2$  film based cysteine sensor at  $\pm 4\text{V}$  in presence of 1mM concentration of interferents namely (A) AA, (B) UA, (C) Gln and (D) His (inset shows the enlarged view of the I– $V$  curve at –4V). 83
- Figure 4.14. Interference study for self-powered cysteine sensor. (A) The open circuit potential drop across the sensor in the presence of 1 mM cysteamine and 1 mM cysteine (@2N load; inset shows the enlarged view of the open circuit potential drop for 1 mM cysteine ). (B) The response of the self-powered cysteine sensor to 1mM concentration of cysteamine and cysteine respectively. 84
- Figure 4.15. (A) Open circuit voltage ( $V_{oc}$ ) and (B) short circuit current ( $I_{sc}$ ) of 0, 0.1, 0.2 and 0.4 % (W/V) of BT/Ag NG at a mechanical load of 2N. 86
- Figure 4.16. Self-powered cysteine sensor. (A) Output voltage and current of BT/Ag nanogenerator as a function of different concentrations of BT NPs (% w/v) at a mechanical load of 2 N. (B) Open circuit voltage ( $V_{oc}$ ) and (C) short-circuit current ( $I_{sc}$ ) of BT/Ag nanogenerator (0.4% w/v) at 2 N. (D) Demonstration of commercial green light-emitting diodes (LEDs) lit using the 87

	piezoelectric potential generated. (E) Stable output voltage of the nanogenerator (under a load of 2 N) for a period of 1000 s with no degradation.	
Figure 4.17.	(A) Output voltage of the nanogenerator (NG) and self-powered cysteine sensor (NG/cysteine sensor) under a load of 2 N. (B) The open-circuit potential drop across the sensor as a function of different cysteine concentrations ( $10^{-2}$ mM to $4 \times 10^{-1}$ mM) at 2 N (inset shows the calibration plot where the potential drop across the sensor has a monotonic functional relationship with the cysteine concentration).	89
Figure 5.1.	Schematic diagram of the BaTiO <sub>3</sub> (BT) film-based piezoelectric nanogenerator (PNG) used in this research.	100
Figure 5.2.	Structural characterization. (a) Raman spectrum and (b) X-ray diffraction (XRD) pattern of the as-synthesized BaTiO <sub>3</sub> nanoparticles (BT NPs). Field-emission scanning electron microscopy (FE-SEM) micrographs of (c) BT NPs film at 2 $\mu$ m scale (inset shows BT NPs $\leq$ 200 nm) (d) a cross-sectional view of BT NPs film with film thickness of $\sim$ 50 $\mu$ m.	102
Figure 5.3.	Fourier-transform infrared (FTIR) spectrum of as-synthesized BT nanoparticles.	103
Figure 5.4.	(a) Open circuit voltage ( $V_{oc}$ ) and (b) short-circuit current ( $I_{sc}$ ) of BT film-based NGs fabricated with 5, 10, and 20% w/v BT NPs at a mechanical load of $F = 0.2$ N.	104
Figure 5.5.	Electrical characterization of NG. (a) Output voltage and current of BT film-based nanogenerator (NG) as a function of different concentrations of BT NPs (% w/v) under a mechanical load ( $F = 0.2$ N). (b) Open circuit voltage ( $V_{oc}$ ) (inset: enlarged image of a single peak-to-peak voltage graph; commercial green light-emitting diodes (LEDs) lit using the piezoelectric potential generated and (c) short-circuit current ( $I_{sc}$ ) of BT-film based NG (20% w/v). (d) Stable output voltage of NG (20% w/v; under a load of $F = 0.2$ N) for a period of 600 s with no degradation.	105
Figure 5.6.	(a) The $V_{oc}$ and (b) $I_{sc}$ of BT film-based NGs (20% w/v BT NPs) before and after poling at an electric field of 5 kV for 15 h (at a mechanical load of $F = 0.2$ N).	106
Figure 5.7.	Polarity switching test. The $V_{oc}$ of BT film-based NG (20% w/v BT NPs) during (a) forward connection and (b) reverse connection (at a mechanical load of $F = 0.2$ N).	106

Figure 5.8.	The Open circuit voltage ( $V_{oc}$ ) of the PNG (a) subjected to different accelerations $0.1 \text{ ms}^{-2}$ , $1 \text{ ms}^{-2}$ , $5 \text{ ms}^{-2}$ and $10 \text{ ms}^{-2}$ (time dependence of the compressive and decompressive load action on PNG). (b) representing number of cycles (n; sinusoidal peaks) for a time period of 5 seconds when subjected to different accelerations.	107
Figure 5.9.	Active (self-powered) glucose sensor. The piezoelectric output of the NG (20% w/v) in the presence of different glucose concentrations (0 to $800 \mu\text{M}$ ) at $F = 0.2 \text{ N}$ (the piezoelectric output voltage of the device was linearly dependent on the concentration of glucose).	108
Figure 5.10.	(a) Relationship between the piezoelectric output of NG and the concentration of glucose. (b) Dependence of the response $r$ on the concentration of glucose.	110
Figure 5.11.	Resolution of peak amplitude. (a) The Open circuit voltage ( $V_{oc}$ ) of the PNG (5 peak cycles) divided into discrete levels by Discrete Fourier transform (DFT) (b) enlarged image of one peak cycle.	111
Figure 5.12.	Schematic representation of the proposed mechanism of BT film-based NG during active biosensing of glucose.	115
Figure 5.13.	Interference study. (a) The piezoelectric output of the NG in the presence of $1 \text{ mM}$ glucose and interferents such as $1 \text{ mM}$ uric acid (UA), $1 \text{ mM}$ ascorbic acid (AA) and $1 \text{ mM}$ galactose (Gal). (b) Response of NG based on the voltage variation in the presence of glucose and interferents.	117
Figure 6.1.	Schematic representation of CAS-CYST-BT conjugate and overview of the proposed work.	132
Figure 6.2.	$514 \text{ nm}$ excited Raman spectra (a) and FTIR spectra (b) of pristine (CAS, CYST, BT) and their conjugate (CAS-CYST-BT).	134
Figure 6.3.	XRD spectra of pristine and $\text{NH}_2$ functionalized BT NPs.	136
Figure 6.4.	$514 \text{ nm}$ excited Raman spectra (a) and FTIR spectra (b) of CAS-BT and CAS-CYST conjugates.	137
Figure 6.5.	Absorbance spectra of (a) CAS, BT (inset) and their conjugate CAS-BT (b) CAS, CYST, and their conjugate CAS-CYST ( $200\text{-}800 \text{ nm}$ range).	138
Figure 6.6.	FESEM micrographs and corresponding EDAX spectrum of (a) CAS, (b) BT, (c) CAS-BT.	138

Figure 6.7.	The schematic representation of the device structure.	139
Figure 6.8.	<i>I-V</i> studies for pH stimuli. <i>I-V</i> curves of (a) CAS and (b) CAS-BT film based devices in response to pH stimuli (range: pH7 to pH1).	140
Figure 6.9.	Comparison between CAS and CAS-BT film based devices' current response to pH stimuli (range: pH7 to pH1; @ +4V).	141
Figure 6.10.	<i>I-V</i> studies for protein-drug interaction. (a) <i>I-V</i> curves of CAS film based device in response to different CYST drug concentration (100mg to 600mg). (b) Three-dimensional (3D) graphical representation of the response of CAS, CAS-BT (CBT) and BT film based devices to different CYST drug concentration (100mg to 600mg) [relative change in current is denoted as $(I-I_0/I_0)$ ].	142
Figure 6.11.	(a) The calibration curve obtained from figure 5a shows the monotonic functional relationship between CYST drug concentration and output current (current response of the device at +4V). (b) <i>I-V</i> curves of the CAS-BT film based device in response to various CYST drug concentration (100 mg to 600 mg). (c) <i>I-V</i> curves of the BT film based device in response to various CYST drug concentration (100 mg to 600 mg). (d) <i>I-V</i> curves of the CAS-BT film based device showing no response to various concentrations of CYS (10 $\mu$ M to 300 $\mu$ M; physiological range).	144
Figure 6.12.	Proof of concept theranostic platform: (a) <i>I-V</i> curve of CAS-CYST film based device in response to different CYS concentrations (10 $\mu$ M to 500 $\mu$ M). (b) The current response of the device at -4V for different CYS concentrations (10 $\mu$ M to 500 $\mu$ M) (calibration plot obtained from <i>I-V</i> curves).	145
Figure 6.13.	Schematic representation of the interaction between CYST and CYS (disulfide bond formation).	147
Figure 6.14.	Piezoelectric response of CAS and CAS-BT film based PNGs with prospects in self-powered applications: Schematic representation of working mechanism of PNG (a) before and (b) after poling. Open circuit voltage ( $V_{oc}$ ) of PNGs (c) before and (d) after poling (Force = 2N). (e) Short circuit current ( $I_{sc}$ ) of PNGs after poling at an applied force of 2N. (f) Comparative graph depicting the output voltage and current of PNGs at a mechanical load of 2N.	149

Figure 6.15. Effect of electrical poling time: Open circuit voltage ( $V_{oc}$ ) of 150 CAS (a) and CAS-BT (b) film based PNGs at different poling period (time) at an electric field of 1kV (at a mechanical load of  $F = 0.2$  N).

Figure 6.16. Polarity switching test. (a) Open circuit voltage ( $V_{oc}$ ) and (b) 150 Short circuit current ( $I_{sc}$ ) of CAS-BT film based PNG during reverse connection (at a mechanical load of  $F = 0.2$  N).

## Abstract – Hangul

스마트 바이오 센서는 생물 의학, 환경 및 식품 분야에서 잠재적 인 응용 분야를 찾습니다. 기존 바이오 센서와 달리 스마트 바이오 센서는 다 기능성을 보유하고있어 무수히 많은 이점을 제공합니다. 바륨 티타 네이트 나노 입자는 압전 특성뿐만 아니라 유전 특성으로 잘 알려진 다기능 물질 중 하나입니다. 그것은 유전체 세라믹 재료로 널리 이용되고 있습니다. BT NPs의 반도체 및 압전 특성은 에너지를 수확하기위한 압전 나노 발전기를 통해 잘보고됩니다. 무연이기 때문에이 생체 적합 형 압전 재료는 PZT (지르코니아 티 타늄 산 납)와 달리 생물학적 응용 분야에서 더욱 유용합니다. 최근에는 벡터, 나노 캐리어, 이미징 프로브 (2 차 고조파 생성, SHG) 조직 공학, 이식 가능 장치 등과 같은 생물학에서의 BT NPs 적용에 관한 연구는 거의보고되지 않았다. 이러한 흥미로운 사실은 바이오 센싱 응용 분야에서이 물질을 조사하게 만들었다. BT NPs의 바이오 센싱 특성을 발견하기위한 광범위한 연구는 이전에 수행되지 않았다. 따라서 현재의 논문 작업은 BT NP의 바이오 센싱 특성과 스마트 바이오 센싱 시스템에서의 적용에 초점을 맞추었다.

이에 초점을 맞춘 첫 번째 연구는 BT NP의 비 효소 포도당 감지 특성이보고 된 자체 구동 식 포도당 센서를 개발하는 것이 었습니다. 이 장의 주요 초점은 포도당을 감지 할 때 BT NPs의 반도체 특성을 조사하는 것이다. 고체상 반응을 통해 합성 된 BT NPs가이 연구에 사용되었다. 다른 글루코스 농도의 도입에 따른 장치의 저항 변화는 (전류 - 전압) I-V 기술을 통해 분석되었다. BT NPs의 루이스

산 부위와 포도당의 루이스 염기 사이의 상호 작용은 포도당을 글루 콘산으로 산화시켜 자유 전자의 방출로 인한 장치의 저항을 변화시킨다. 또한 자체 구동 식 포도당 센서는 센서를 압전 나노 발전기의 외부 통합과 함께 구현했습니다. 글루코오스 농도가 증가함에 따라 센서를 가로 질러 잠재적 인 강하는 자체 구동 식 바이오 센싱 신호로서 얻어졌다. 이것은 BT NPs 필름 기반 자체 구동 식 포도당 센서의 첫 번째 보고서입니다.

Biosensing 에서의 BT NPs 능력에 대한 예비 조사는 자극 반응 행동을 연구하도록 자극했다. BT NP 가 pH 와 같은 다른 자극에 반응하는 능력은 스마트하고 다기능 인 바이오 센서를 개발하는 데 엄청난 도움이 될 것입니다. 따라서, NH<sub>2</sub> 작용 화 된 NP 는 IV 장에서 논의 된 바와 같이 시스테인 분자 검출에 사용되었다. 시스테인의 직접 검출은 현재 이용 가능한 접근법에 대해 상당한 중요성을 가질 수있다. 이 장에서는자가 구동 시스테인 센서에 대한 연구가 압전 나노 발전기 (BT / Ag PNG)와 aAg / BT-NH<sub>2</sub> (아가로 오스 / 아민 관능 화 된 BaTiO<sub>3</sub> NPs) 필름 기반 시스테인 센서를 외부 적으로 통합함으로써 입증되었다. 위의 두 장이 센서와 압전 나노 발전기의 외부 통합에 초점을 맞추었기 때문에, V 장은 센서와 압전 나노 발전기의 내부 통합에 대해 설명합니다. 여기서는 독립형, 완전 통합 된 원 스톱 장치를 사용하여 생체 분자 (포도당)를 검출했습니다. 글루코오스 분자를 검출하기위한 능동형 바이오 센서로 Al / BT / ITO 압전 나노 발전기 (알루미늄 (Al) / 티탄산 바륨 (BT) / ITO)를 제조 하였다. 바이오 센서와

에너지 수확기의 겸용 기능이 센서는 작동을위한 외부 전원을 필요로하지 않고 능동 센서로 작동합니다.이 나노 발전기에서 생성 된 압전 출력은 바이오 소스 신호뿐만 아니라 에너지 원 역할을합니다. 압전 기반 감지는 BT 필름에 생체 분자의 화학 흡착이 자유 캐리어 밀도를 변화시키고 궁극적으로 NG 의 압전 출력에 영향을 미친다는 것입니다. 이것은 생체 분자 검출을위한 BT NP 기반 활성 센서에서 최초로 보고됩니다.

제 6 장은 개념 증명 theranostic 응용 프로그램의 증명에 BT NPs 의 조사를 다룹니다. COSIN, 구형 phosphoprotein 은 잘 자체 세포 - 미셀 구조를 활용하여 기존의 약물 전달 응용 프로그램에 사용되었습니다. 단백질 - 약물 상호 작용과 개념 증명 theranostics 를 명료하게하기 위해 고안된 카세인 미셀 (CAS) 기반의 고체 상태의 금속 - 단백질 - 금속 전기 접합부가이 장의 하이라이트입니다 VI.이 생체 적합 전자 플랫폼은 다 기능성, 상호 작용 단백질과 약물 / 분석 물질을 전기 신호로 변환시켜 나노 전자 공학과 생물 정보 처리 시스템 사이의 정교한 인터페이스를 제공합니다. 아가로 오스 바이오 폴리머는 3 차원 네트워크를 형성하고 생체 분자에 비활성 인 동시에 대체 전극 재료로 사용되기 때문에 현재 작업에서 디바이스 제조를위한 매트릭스 역할을합니다. 전류 - 전압 (I-V) 기술을 통해 확인 된 CAS, 시스 테 아민 (CYST; 모델 약물) 및 아민 관능 화 된 바륨 티타네이트 나노 입자 (BT NP) 사이의 성공적인 접합은 분광 결과에 잘 부합한다. 이 다기능 바이오 센싱 플랫폼을 통해 반응 단백질과 CAS 와 CYST (단백질 - 약물)

간의 상호 작용이 확인되었습니다. 또한 CAS-CYST 접합체 기반 고체 상태 장치는 I-V 곡선을 통해 관찰된 시스테인 (CYS) 분석 물에 대한 우수한 반응을 나타내어 개념 증명 theranostics 의 실현을 유도했습니다. 또한, 압전 나노 발전기 (PNG)를 사용하여 생체 접합체의 잠재성에 대한 생체 접합 물의 피에조 전기 응답을 조사한 결과, 압전 나노 발전기 (PNG)를 사용하여 입증되었습니다. 논문에서 제시된 모든 연구 결과는 진단 및 치료 응용 분야에 대한 비 전통적이고 쉬운 대안을 제공하며 향후 전망은 브리핑됩니다 마지막 장 VII 에서.

## Abstract

Smart biosensors find potential applications in biomedical, environmental as well as in food sectors. Unlike their conventional counterparts, smart biosensors possess multifunctionality rendering them myriads of advantages. Barium titanate nanoparticle is one such multifunctional material well known for its piezoelectric as well as dielectric properties. It has been widely exploited as a dielectric ceramic material. The semiconducting and piezoelectric properties of BT NPs are well reported by means of piezoelectric nanogenerators for harvesting energy. Being lead free, this biocompatible piezoelectric material seems to be more useful in biological applications unlike its counterpart, PZT (Lead zirconatetitanate). Only recently, few studies have been reported on BT NPs application in biology such as vectors, nanocarriers, imaging probes (second harmonic generation; SHG) tissue engineering, implantable devices etc. These interesting facts have prompted to investigate this material for biosensing applications. No extensive research has been undertaken previously for discovering the biosensing property of BT NPs. Hence, the present thesis work was framed with the focus on unraveling the biosensing properties of BT NPs and its application in smart biosensing systems.

With this in focus, the first study was to develop a self-powered glucose sensor, where the non-enzymatic glucose sensing property of the BT NPs is reported. The main focus in this chapter III is to investigate the semiconducting properties of the BT NPs in

sensing glucose. BT NPs synthesized through solid state reaction were used for this study. The change in resistance across the device with the introduction of different glucose concentrations were analyzed through (current-voltage) *I-V* technique. The interaction between lewis acid sites in BT NPs and lewis base in glucose leads to the oxidation of glucose to gluconic acid, thus changing the resistance across the device due to release of free electrons. Further, self-powered glucose sensor was realized by external integration of the sensor to that of a piezoelectric nanogenerator. The potential drop across the sensor with increase in glucose concentration was obtained as the self-powered biosensing signal. This is the first report of BT NPs film based self-powered glucose sensor.

This preliminary investigation of the BT NPs ability in biosensing further prompted to study its stimuli responsive behavior. The ability of the BT NPs to respond to different stimuli such as pH will be of immense help in developing smart, multifunctional biosensors. Therefore, the  $\text{NH}_2$  functionalized BT NPs were employed in detecting Cysteine molecules as discussed in chapter IV. Direct detection of cysteine could have considerable significance over the currently available approaches. In this chapter, investigation on the self-powered cysteine sensor is demonstrated by externally integrating a Ag/BT- $\text{NH}_2$  (Agarose/amine-functionalized  $\text{BaTiO}_3$  NPs) film-based cysteine sensor with a piezoelectric nanogenerator (BT/Ag PNG).

As the above two chapters were focused on external integration of the sensor and piezoelectric nanogenerator, chapter V describes about the internal integration of the

sensor and piezoelectric nanogenerator. Here, a stand-alone, fully integrated, one stop device was used for detecting biomolecule (glucose). Al/BT/ITO piezoelectric nanogenerator (Aluminum (Al)/Barium titanate (BT)/Indium Tin Oxide (ITO) was fabricated as an active biosensor for detecting glucose molecules. The novelty in this work lies in the fact that the active sensor has dual functions both as biosensor and energy harvester. The sensor does not require an external power source for operation rather functions as an active sensor. The piezoelectric output produced from this nanogenerator serves as the energy source as well as the biosensing signal. The principle behind this piezoelectric based sensing is that, the chemisorption of biomolecules on to the BT film will change its free-carrier density and eventually influence the piezoelectric output of the NG. This is first report as such on BT NPs based active sensor for biomolecule detection.

Chapter VI deals with the investigation of BT NPs in proof of concept theranostic application. Casein, a globular phosphoprotein, has been well utilized for conventional drug delivery applications taking advantage of its self-assembled micellar structure. Casein micelle (CAS) based solid-state device through metal-protein-metal electrical junctions designed for elucidating protein-drug interaction as well as proof-of-concept theranostics are the highlights of this chapter VI. This biocompatible electronic platform has multifunctionality, transducing interactions between protein and drug/analyte into electrical signals providing a sophisticated interface between nanoelectronics and biological information processing systems. Agarose biopolymer serves as the matrix for device fabrication in the present work because of its ability to

form a three-dimensional network and being inert to biomolecules at the same time serving as an alternate electrode material. The successful conjugation between CAS, cysteamine (CYST; model drug), and amine functionalized Barium titanate nanoparticles (BT NPs) confirmed through current-voltage (*I-V*) technique complies well with the spectroscopic results. Conjugates pH-responsive behavior and the interaction between CAS and CYST (protein-drug) were confirmed through this multifunctional biosensing platform. Moreover, CAS-CYST conjugate based solid-state device demonstrated a good response to cysteine (CYS) analyte observed through *I-V* curves, led to the realization of proof-of-concept theranostics. Additionally, investigation of the piezoelectric response of the bioconjugates for prospects in the self-powered application was demonstrated using piezoelectric nanogenerator (PNG). All of the above mentioned investigations presented in the thesis provide an unconventional and facile alternative for diagnostic and therapeutic applications and their future prospects are briefed in the final chapter VII.

# CHAPTER I

## Introduction

### 1.1 Background

In the era of personalized medicine and sophisticated diagnostic procedures, development of smart biosensing systems is much welcomed and more than just a necessity. Smart biosensing systems are nothing but biosensors having more than one function<sup>[1]</sup> and they are mostly integrated systems. It is evident from the term smart that it is different and advanced compared to its conventional counterparts. One such feature of smart biosensing system is the self-powered<sup>[2][3]</sup> concept where the sensor operates without a battery. Piezoelectric nanogenerators (PNG) are well utilized for harvesting energy and it can serve as the power source for these sensors<sup>[4]</sup>. Piezoelectric nanogenerators (PNG) are among the older, more established energy harvesters converting mechanical energy into electrical energy. Thus by either external integration<sup>[5][6]</sup> or internal integration<sup>[3,7]</sup>, the sensor devices can be coupled to PNGs which act as the power source to drive these sensors (Figure 1.1). Such battery free sensors are one such example of smart biosensing systems. Apart from this concept, combination of more than one application such as diagnostic and therapeutic; stimuli responsive behavior<sup>[8]</sup>; protein drug interactions; biomimetic sensing systems<sup>[8][9]</sup>; wireless diagnostic systems; intelligent logic aptasensors<sup>[10]</sup> etc contribute to smart sensing. The realization of such a smart nanosystem is quite challenging, but highly

desirable for next-generation diagnostic and theranostic applications. Such unconventional diagnostic tools can be realized from conventional principles existing in everyday applications, such as piezoelectricity. Barium titanate ( $\text{BaTiO}_3$ ) nanoparticles are one such multifunctional material well known for its dielectric and piezoelectric properties<sup>[11]</sup>. Though it has been much explored in materials aspect and related applications, detailed studies on biological applications such as biosensing have not been reported previously. Taking into account of its properties in advantage to biological applications<sup>[12,13]</sup>,  $\text{BaTiO}_3$  nanoparticles can serve as potent nanomaterial in developing smart biosensors. In this thesis, demonstration of such applications has been undertaken. These studies can further open up new avenues in biomedical sector as well as in advanced diagnostic approaches.



**Fig. 1.1.** Overview of smart biomedical devices (Image source: *Adv. Sci.* 2017, 4)

## 1.2. Biosensors

A biosensor is an analytical device comprising of a biological recognition element with a physio-chemical transducer. They are simple, inexpensive measurement systems that fuse the exquisite sensitivity and specificity of living systems with the processing power of microelectronics. It comprises of three main parts (Figure 1.2) namely,

- (i) Biological recognition element that renders specificity to the target molecule amidst potent interfering species,
- (ii) Transducer which converts these biorecognition events into a sensible measurable signals, and
- (iii) Signal processing system responsible for converting these signals into readable data.

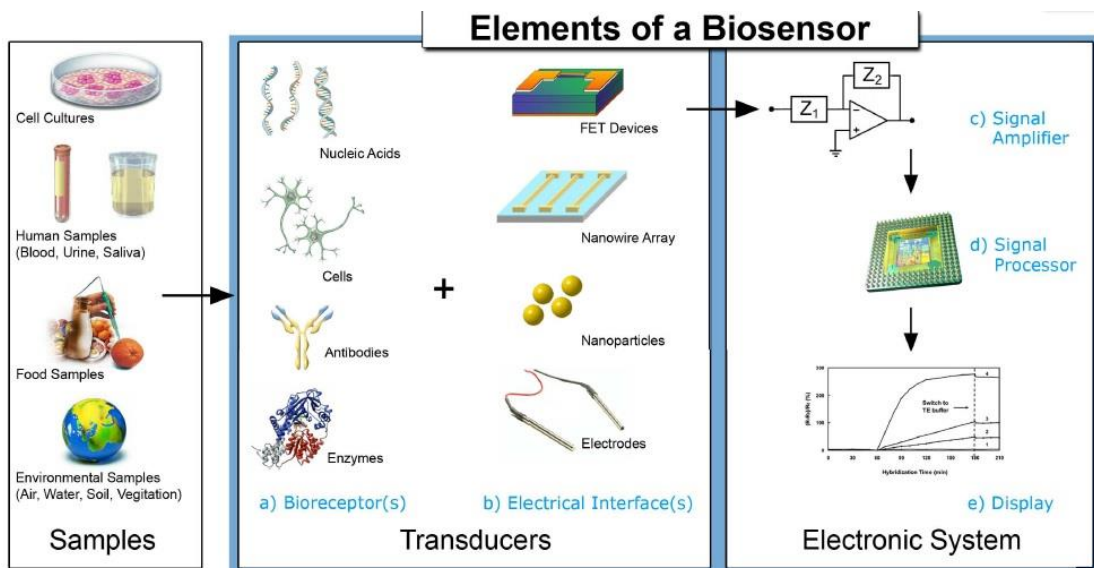


**Fig. 1.2.** Schematic representation of the elements of a typical biosensor

There are a huge class of biomolecules considered as molecular recognition elements which includes,

- Enzymes
- Receptors
- Antibodies
- Nucleic acids (RNA, DNA)
- Microbial organisms
- Clinically important analytes etc.

In general transducer can be classified in to five principle classes namely,

➤ **Electrochemical**

Generally, in electrochemistry, the biorecognition is either through generating a current (amperometric), a potential (potentiometric) or through altering the conductivity of a medium (conductometric) between electrodes. It typically consists of three electrodes namely a reference electrode, a counter and a working electrode. The reference electrode, is used to maintain a known, stable potential; working electrode serves as the transduction element in biochemical reaction; and counter electrode establishes a connection to the electrolytic solution so that a current can be applied to the working electrode. These electrodes should possess properties like both conductivity and chemical stability.

➤ **Optical transducer**

The optical biotransducers, use photons as source of information about the analyte after its interaction with the bio recognition element. The detection mechanism of optical biotransducer includes evanescent field detection principle which enables the detection of fluorophores in close proximity of the optical fiber. These transducers are highly specific and sensitive.

➤ **Thermometric**

These transducers are based on the thermostats. They monitor the temperature produced / changes due to the interaction of analyte with bio-recognition element. Such changes in temperature are monitored and given as sensing signal.

➤ **Piezoelectric transducer**

Piezoelectric based biosensors use the basic principle of a change in mass as observed in QCM (quartz crystal microbalance) and SAW (surface acoustic waves). Biomolecules, such as proteins or antibodies can bind and its change in mass gives a measurable signal proportional to the presence of the target analyte in the sample.

➤ **Electronic transducer**

Electronic transducers convert chemical or biological binding events into electrical signals favourable for highly sophisticated interface between nanoelectronics and biological information processing systems. Such examples include FET based and solid state devices (biosensors). The change in surface

charge of the material due to binding of target analyte or related properties are converted in to readable electronic signals as current or voltage.

### 1.3. Properties of Barium titanate (BaTiO<sub>3</sub>)



**Fig. 1.3.** Multifunctional properties of Barium titanate (BaTiO<sub>3</sub>)

The Barium titanate (BaTiO<sub>3</sub>) is a well-known, lead free, metal oxide with an ABO<sub>3</sub> perovskite structure, having (n-type) semiconducting and high level of inherent piezoelectric properties [3], [13].

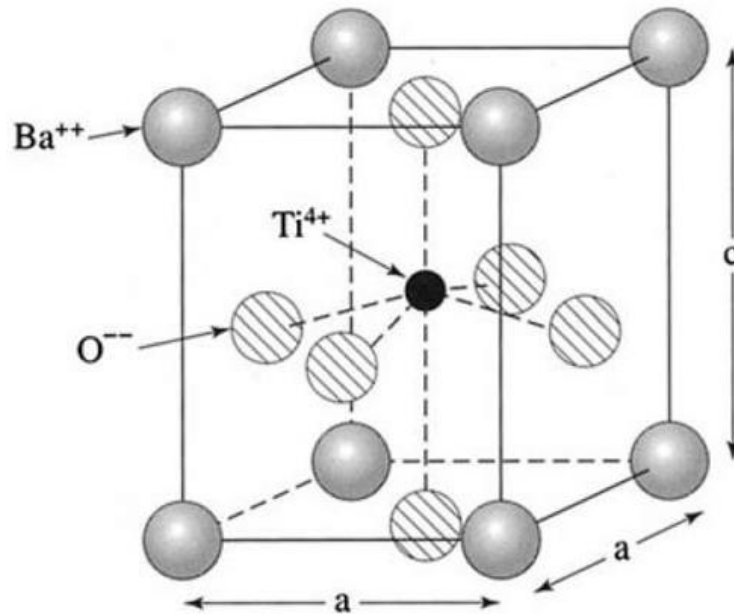


**Fig. 1.4.** Tetragonal crystal structure of Barium Titanate ( $\text{BaTiO}_3$ )

First detailed report on crystal structure of  $\text{BaTiO}_3$  ferroelectric phase at high temperature was proposed by Megaw (1945) [14] and its interrelationship between anomalous electromechanical, structural, and thermal properties was modeled phenomenology by A.F. Devonshire [15] (Figure 1.4).  $\text{BaTiO}_3$  (BT) is one of the most studied ferroelectrics. At room temperature it has a tetragonal structure, a dielectric constant equal to 200 in the  $c$  direction and 4000 in the  $a$  direction, a piezoelectric sensitivity ( $d_{33} = \sim 200 \text{pC/N}$ ), a permanent polarization of  $26 \mu\text{Ccm}^{-2}$ , a coercive field value between  $500$  and  $2000 \text{V cm}^{-1}$  and a refractive index of  $2.4^{[14]}$ . The piezoelectric coefficient can be enhanced even up to  $\sim 420 \text{pC/N}$ , almost equal to PZT by appropriate doping. However, the physical properties of thin films grown on a variety of substrates are affected by the surface tension, surface dipole layers, impurities and polycrystalline

nature so that they can be quite different from the bulk properties. As a well-known dielectric material it has been used as an insulating material to fabricate MIS structures. It exhibits several advantages by possessing properties such as high charge storage capacity, good insulating property, low leakage current density and high dielectric breakdown strength. Though it is well-known as piezoelectric, dielectric ceramic material, it still remains less exploited as a bio-sensing and theranostic agent. This invoked great interest to study its bio-sensing property by utilizing its semiconducting nature and to couple its piezoelectric property (for harnessing electrical energy) which can be used for driving (power source) the sensor. BTO nanostructures has comparable and better functional properties than well utilized ZnO nanostructures with respect to high piezoelectric coefficient [3], [13] low dielectric constant, stability at large electric fields and low electrical noise. In near future, BTO can find potential applications in various fields just as ZnO (semiconductor/piezoelectric) been greatly exploited for sensing [16], [17], self-powered systems [2], [18] for continuous monitoring and so on.

Apart from materials aspect, it has unique features, such as biocompatibility, second-harmonic generation (SHG) [13] etc. Unlike PZT, its counterpart, BT NPs are biocompatible, cytocompatible, making them a potential candidate for applications in biosensing [15], theranostics [11], bioimaging [16], and piezoelectric-based energy harvesting [17], drug delivery, *in vivo* imaging [13], cancer therapy [11], and self-powered nanosystems<sup>[17]</sup> (Figure 1.3). Furthermore, such ceramic perovskite-structured metal oxides have applications in electrical and electronic devices. As yet, the fact that this has still not been exploited extensively for biological applications renders great interest for

self-powered biosensing and theranostic applications. This background prompted us to investigate BT NPs in the field of biosensing for developing self-powered sensors.

#### **1.4. Piezoelectric nanogenerators (PNG)**

Piezoelectric nanogenerators (PNG) are among the older, more established energy harvesters converting mechanical energy into electrical energy <sup>[18]</sup>. Much research has been focused on harvesting mechanical energy in living environments, and scavenging biomechanical energy, and their conversion to electrical power for powering low-power electronic gadgets and sensors <sup>[19]</sup>. Few reports on PNGs as implantable devices for health monitoring are available <sup>[20],[21]</sup>. PNGs are made of piezoelectric materials such as BT NPs, ZnO NPs, PZT etc which has considerable piezoelectric coefficient. The piezoelectric material either deposited as a thin film or as a composite film is sandwiched in between two electrodes as current collectors. When a compressive force is applied, orientation of dielectric poles in the piezoelectric material will occur, generating a piezoelectric potential. The perpendicular force acting on the piezoelectric material (film) generates a piezopotential on both sides of the film, which, in turn, induces inductive charges on the top and bottom electrodes. The charge carriers create a potential difference, which drives electrons through the external circuitry. This potential difference in form of voltage or current can be collected through external leads. Thus they are useful as efficient energy harvesters.

## 1.5. Self-powered systems

Self-powered diagnostic systems have advantage over conventional sensors (MEMS/NEMS) in such a way that it can operate without a battery which is made up of highly toxic chemicals with limited life time. Self-powered systems with novel features, such as battery-less operation, portability, point-of-care diagnosis, and implantable applications<sup>[6]</sup>, can be developed using piezoelectric nanogenerators (PNG), a relatively old energy-harvesting technology in which mechanical energy is converted into electrical energy. Self-powered nanosensors combine the nanogenerator with a sensor, through internal or external integration. Thus, the energy harvested from the nanogenerator is used to drive the sensor either directly or by storing it in proper power management systems and then utilized later.

Multi-functional, self-powered, piezoelectric-based active sensors have potential in the development of medical devices for health-monitoring purpose<sup>[22,23]</sup>. The realization of such a smart nanosystem is quite challenging, but highly desirable for next-generation diagnostic and theranostic applications. Such unconventional diagnostic tools can be realized from conventional principles existing in everyday applications, such as piezoelectricity. Self-powered application can be achieved in either of two ways; through external integration or internal integration (Figure 1.5).

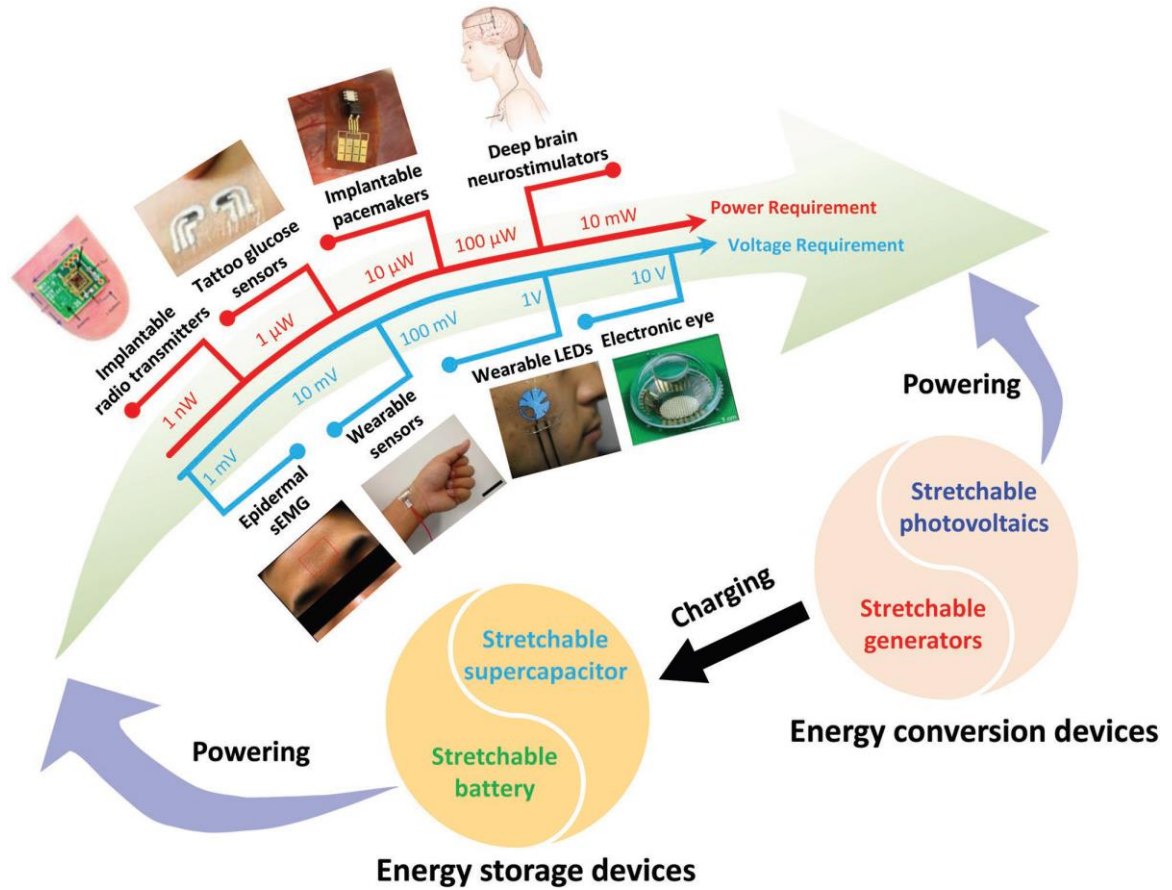


**Fig. 1.5.** External integration between energy conversion devices and biomedical devices. (Image source: *Adv. Energy Mater.* **2017**, 1700648)

Multi-functional, self-powered, piezoelectric-based active sensors have potential in the development of medical devices for health-monitoring purpose<sup>[22,23]</sup>. The realization of such a smart nanosystem is quite challenging, but highly desirable for next-generation diagnostic and theranostic applications. Such unconventional diagnostic tools can be realized from conventional principles existing in everyday applications, such as

piezoelectricity. Self-powered application can be achieved in either of two ways; through external integration or internal integration.

### **1.5.1. External and internal integration**

Operation any device needs appropriate energy (power consumption) as shown in Figure 1.6. In case of external integration, the power source (PNG) is externally integrated to the sensor/ lower power devices (through parallel connection). Thus the energy from the PNG can act as the power supply to drive the sensor. Instead of harvesting energy separately and integrating it externally with a sensor, a one-stop device having dual functions may be possible. This constitutes the internal integration where the PNG itself acts the sensor. This is highly desired in developing self-powered medical devices. Moreover, vital biomedical information could be determined from the piezoelectric output of a nanogenerator by tailoring its piezoelectric properties for monitoring or sensing biologically important molecules. This suggests a new era of piezo-based biosensing where piezoelectric, piezotronic, and semiconducting properties could play a major role <sup>[24], [25], [26]</sup>. Thus, tailoring these properties by means of biomolecules can result in a novel biosensing mechanism <sup>[24], [27], [7]</sup>.

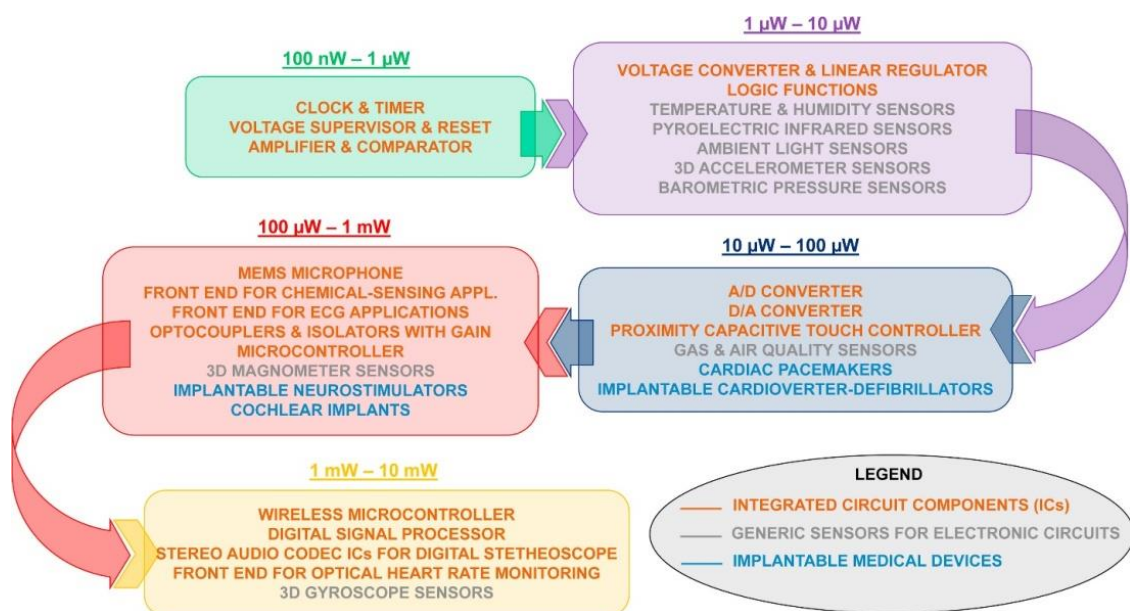


**Fig. 1.6.** Power consumption value of generic integrated circuit components and sensors as well as implantable devices (Image source: *Trends in Biotechnology* 2017, 35, 610-624)

With limitations in the operational lifetime of the conventional batteries used for powering implantable devices, continuous monitoring over long periods is almost impossible. Surgeries are needed to replace batteries, leading to complications and morbidity. Implantation of both an energy harvester and a monitoring system could be a solution but it would occupy more space inside the recipient animal or patient, involving complex surgical procedures. Thus, developing a stand-alone, fully integrated, one-stop device (an active biosensor) is a desirable solution<sup>[3]</sup>.

## 1.6. Research objectives/ scope of thesis

The objectives of the research undertaken in this thesis can be categorized as follows.

- The primary objective of this research is to realize BaTiO<sub>3</sub> nanoparticle for biosensing application.
- To develop self-powered glucose biosensor using BaTiO<sub>3</sub> nanoparticles by means of solid-state device (metal-semiconductor-metal configuration).
- Development of BaTiO<sub>3</sub> nanoparticles based piezoelectric nanogenerators (PNG) for self-powered biosensing application.
- To develop externally integrated systems by connecting the sensor to piezoelectric nanogenerator through parallel connection (self-powered systems).
- To functionalize BaTiO<sub>3</sub> nanoparticles with functional groups like -OH, -NH<sub>2</sub> (through, silane coupling agents) for stimuli responsive direct detection of cysteine biomolecule.
- Development of BaTiO<sub>3</sub> nanoparticles based composite film for fabricating PNGs which can serve as the power source for driving the sensor.
- To develop BaTiO<sub>3</sub> nanoparticles based internally integrated, one-stop device as an active sensor for biomolecule detection (glucose). Here, the PNG itself acts as both power source (energy harvester) and biosensor. The piezoelectric output from the device has dual functions as biosensing signal as well as energy source.
- Finally, to study BaTiO<sub>3</sub> nanoparticles in developing biocompatible electronic platform for analyzing protein-drug interactions and proof-of-concept thernostic

applications. This opens up new avenues for transducing chemical or biological binding events into electrical signals favourable for highly sophisticated interface between nanoelectronics and biological information processing systems.

### **1.7. Structure of this thesis**

The entire thesis is systematically divided in to seven chapters as follows:

Chapter I gives brief information about the overall thesis, background information on biosensors in general, the unique and general properties of Barium titanate nanoparticles with respect to the proposed thesis work, role of piezoelectric nanogenerators and self-powered systems and finally the scope and structure of the thesis.

Chapter II contains information about the chemicals and reagents used while carrying out this research work, general information on the synthesis methodology, functionalization of nanoparticles , techniques involved in characterization of the nanoparticles and instrumentation for device characterization and relevant electrical measurements.

Chapter III deals with exploring the biosensing property of BaTiO<sub>3</sub> nanoparticles. Here, for the first time, a self-powered BaTiO<sub>3</sub> nanoparticles film based nonenzymatic glucose sensor using a metal-semiconductor-metal (M-S-M) device structure has been demonstrated. *I-V* based detection technique was utilized for confirming the glucose sensing ability of the BaTiO<sub>3</sub> nanoparticles film based sensor

with constant bias voltage under different glucose concentrations. Self-powered glucose sensor was demonstrated by establishing a parallel connection between the sensor and a flexible piezoelectric nanogenerator (PNG). The PNG which serves as the external power source is made up of BaTiO<sub>3</sub> nanocubes along with PVDF polymer formed as a thin film and two electrodes were attached on both sides of the film for electrical connection. The proposed self-powered glucose sensor and BaTiO<sub>3</sub> nanoparticles film based glucose sensor have similar electrical behavior where conductivity increases with increase in glucose concentrations. A self-powered glucose sensor by means of an external integration between the sensor and PNG was achieved.

Chapter IV is about exploring the stimuli responsive behavior of functionalized BaTiO<sub>3</sub> nanoparticles in cysteine detection. Here, a self-powered cysteine sensor was demonstrated by externally integrating a cysteine sensor with a PNG. Ag/BT-NH<sub>2</sub> film-based cysteine sensor with metal–semiconductor–metal (MSM) configuration was connected in parallel to a BT/Ag film-based piezoelectric nanogenerator (BT/Ag PNG). The cysteine sensor's analytical outputs were analysed using a current–voltage (*I–V*) technique. In a self-powered cysteine sensor, the voltage across the sensor decreases with an increase in the cysteine concentration; this potential drop is measured as the sensing signal, in accordance with *I–V* studies.

Chapter V deals with the fabrication of Barium titanate nanoparticles (BT NPs) based piezoelectric nanogenerator (PNG) as an active sensor for biomolecule detection. This smart biosensor is based on piezoelectric and semiconducting properties of Barium titanate nanoparticles (BT NPs). An Al/BT/ITO NG (Aluminum (Al)/ Barium titanate

(BT) / Indium Tin Oxide (ITO) nanogenerator) was devised as a self-powered biosensor for actively detecting glucose. The piezoelectric output generated from this NG has dual functions, as both an energy source and a biosensing signal. The novel self-powered glucose biosensor has good selectivity (~6-fold increase in response vs. interferents) and the approach demonstrated here can serve as a prototype for the development of next-generation smart/self-powered nanosystems for theranostic applications.

Chapter VI deals with the investigation of BT NPs in proof of concept theranostic application. Casein micelle (CAS) based solid-state device through metal-protein-metal electrical junctions designed for elucidating protein-drug interaction as well as proof-of-concept theranostics are the highlights of this chapter VI. This biocompatible electronic platform has multifunctionality, transducing interactions between protein and drug/analyte into electrical signals providing a sophisticated interface between nanoelectronics and biological information processing systems. The successful conjugation between CAS, cysteamine (CYST; model drug), and amine functionalized Barium titanate nanoparticles (BT NPs) confirmed through current-voltage (*I-V*) technique complies well with the spectroscopic results. Conjugates pH-responsive behavior and the interaction between CAS and CYST (protein-drug) were confirmed through this multifunctional biosensing platform. Moreover, CAS-CYST conjugate based solid-state device demonstrated a good response to cysteine (CYS) analyte observed through *I-V* curves, led to the realization of proof-of-concept theranostics. Additionally, investigation of the piezoelectric response of the bioconjugates for

prospects in the self-powered application was demonstrated using piezoelectric nanogenerator (PNG).

Finally, in chapter VII, the summary and overall view of the thesis is briefed and the suggestions for future work is also discussed.

## 1.8. References

- [1] W. H. Suh, Y. H. Suh, G. D. Stucky, *Nano Today* **2009**, 4, 27.
- [2] D. Bradley, *Mater. Today* **2010**, 13, 10.
- [3] Y. Zhao, Y. Fu, P. Wang, L. Xing, X. Xue, *Nanoscale* **2015**, 7, 1904.
- [4] D.-M. Shin, H. J. Han, W.-G. Kim, E. Kim, C. Kim, S. W. Hong, H. K. Kim, J.-W. Oh, Y.-H. Hwang, *Energy Environ. Sci.* **2015**.
- [5] B. Saravanakumar, S. Soyoon, S. Kim, *ACS Appl. Mater. Interfaces* **2014**, 6, 13716.
- [6] R. Yu, C. Pan, J. Chen, G. Zhu, Z. L. Wang, *Adv. Funct. Mater.* **2013**, 23, 5868.
- [7] Y. Zhao, P. Deng, Y. Nie, P. Wang, Y. Zhang, L. Xing, X. Xue, *Biosens. Bioelectron.* **2014**, 57, 269.
- [8] Z. Sun, C. Han, M. Song, L. Wen, D. Tian, H. Li, L. Jiang, *Adv. Mater.* **2014**, 26, 455.
- [9] K. Aran, J. Parades, M. Rafi, J. F. Yau, A. P. Acharya, M. Zibinsky, D.

- Liepmann, N. Murthy, *Adv. Mater.* **2015**, *27*, 1433.
- [10] J. Sun, F. Yang, D. Zhao, C. Chen, X. Yang, *ACS Appl. Mater. Interfaces* **2015**, *7*, 6860.
- [11] E. FarrokhTakin, G. Ciofani, G. L. Puleo, G. de Vito, C. Filippeschi, B. Mazzolai, V. Piazza, V. Mattoli, *Int. J. Nanomedicine* **2013**, *8*, 2319.
- [12] M. Giannini, M. Giannaccini, T. Sibillano, C. Giannini, D. Liu, Z. Wang, A. Baù, L. Dente, A. Cuschieri, V. Raffa, *PLoS One* **2014**, *9*, e115183.
- [13] C.-L. Hsieh, R. Grange, Y. Pu, D. Psaltis, *Biomaterials* **2010**, *31*, 2272.
- [14] L. Dong, D. S. Stone, R. S. Lakes, **2012**, *84107*, 1.
- [15] S. Selvarajan, N. R. Alluri, A. Chandrasekhar, S.-J. Kim, *Sensors Actuators B Chem.* **2016**, *234*, 395.
- [16] J. Čulić-Viskota, W. P. Dempsey, S. E. Fraser, P. Pantazis, *Nat. Protoc.* **2012**, *7*, 1618.
- [17] N. R. Alluri, B. Saravanakumar, S. J. Kim, *ACS Appl. Mater. Interfaces* **2015**, *7*, 9831.
- [18] K. Park, J. H. Son, G. Hwang, C. K. Jeong, J. Ryu, M. Koo, I. Choi, S. H. Lee, M. Byun, Z. L. Wang, K. J. Lee, **2014**, *26*.
- [19] S. Kwon, W. K. Kim, J. Park, Y. Yang, B. Yoo, C. J. Han, Y. S. Kim, **2016**.

- [20] M. Alam, D. Mandal, **2016**.
- [21] G. Hwang, H. Park, J. Lee, S. Oh, K. Park, M. Byun, H. Park, G. Ahn, C. K. Jeong, K. No, H. Kwon, S. Lee, B. Joung, K. J. Lee, .
- [22] Q. Zheng, B. Shi, Z. Li, Z. L. Wang, *Adv. Sci.* **2017**, *4*, 1.
- [23] Q. Zheng, H. Zhang, B. Shi, X. Xue, Z. Liu, Y. Jin, Y. Ma, Y. Zou, X. Wang, Z. An, W. Tang, W. Zhang, F. Yang, Y. Liu, X. Lang, Z. Xu, Z. Li, Z. L. Wang, *ACS Nano* **2016**, *10*, 6510.
- [24] A. Manuscript, **2010**.
- [25] S. Selvarajan, N. Rao, A. Chandrasekhar, *Biosens. Bioelectron.* **2017**, *91*, 203.
- [26] R. Yu, S. Niu, C. Pan, Z. L. Wang, *Nano Energy* **2015**, 1.
- [27] P.-H. Yeh, Z. Li, Z. L. Wang, *Adv. Mater.* **2009**, *21*, 4975.

## CHAPTER II

### Materials and characterization techniques

For successful completion of the proposed work, the experimental work which includes material synthesis, device fabrication and characterization were carried out in the laboratory. The physico-chemical characterization of as prepared nanomaterials were also performed. Chapter II contains such relevant information. It includes information on synthesis methodology, materials, chemicals and apparatus used, the characterization techniques involved and so on.

#### 2.1. Chemicals and apparatus

High purity research grade chemicals were used for carrying out experiments discussed in this thesis work. Details on the chemicals and apparatus used in each experiment is given under the respective chapters.

#### 2.2. Synthesis method

The barium titanate ( $\text{BaTiO}_3$ ) nanoparticles used in this research were synthesized using solid state reaction method. Apart from solid state reaction method, attempts were also made to synthesize through hydrothermal method. But solid state reaction yielded higher quantity as well as quality of nanoparticles with good crystallinity and tetragonal phase<sup>[1]</sup>. Hence, throughout the research work  $\text{BaTiO}_3$  nanoparticles synthesized through solid state reaction were employed. The overall

synthesis methodology is briefed in this chapter and specific synthesis conditions are given in detail under each chapter respectively.

### **2.2.1. Solid state reaction**

Solid state reactions are usually performed in the absence of solvents by either grinding or melting the starting materials together or simply applying heat to a mixture of starting materials. This type of reaction is usually performed in order to obtain polycrystalline inorganic solids but may also be used in organic synthesis. Solid state reactions offer reduced costs, decreased amounts of chemical waste and, sometimes, an increase in yield. This is one of the established routes for synthesizing high crystalline BaTiO<sub>3</sub> nanoparticles. Solids do not react together at room temperature over normal time scales and it is necessary to heat them to much higher temperatures, often to 1000 to 1500 °C in order for the reaction to occur at an appreciable rate. The factors on which the feasibility and rate of a solid state reaction depend include, reaction conditions, structural properties of the reactants, surface area of the solids, their reactivity and the thermodynamic free energy change associated with the reaction.

### **2.2.2. Hydrothermal synthesis**

The most widely adopted method for synthesizing nanoparticles is hydrothermal method. Hydrothermal synthesis can be defined as a method of synthesis of single crystals that depends on the solubility of minerals in hot water under high pressure. The crystal growth is performed in an apparatus consisting of a steel pressure vessel called an autoclave, in which a nutrient is supplied along with water (Figure 2.1.). A

temperature gradient is maintained between the opposite ends of the growth chamber. At the hotter end the nutrient solute dissolves, while at the cooler end it is deposited on a seed crystal, growing the desired crystal. Advantages of the hydrothermal method over other types of crystal growth include the ability to create crystalline phases which are not stable at the melting point. Also, materials which have a high vapour pressure near their melting points can be grown by the hydrothermal method. The method is also particularly suitable for the growth of large good-quality crystals while maintaining control over their composition. Disadvantages of the method include the need of expensive autoclaves, and the impossibility of observing the crystal as it grows.



**Fig 2.1.** Autoclave apparatus used for hydrothermal synthesis.

For synthesis of BaTiO<sub>3</sub> nanoparticles equimolar concentration of precursors namely TiO<sub>2</sub> nanoparticles and BaCl<sub>2</sub> of high purity (99.9%) were dissolved in 20 ml of 10M NaOH. This mixture was then transferred to Teflon-lined stainless autoclave and maintained at 200 °C for 72 h. After completion of reaction, it was allowed to cool to

room temperature and washed multiple times with deionized water (centrifuge at 6000 rpm for 20 min). The as obtained powder is dried and further characterized for analyzing physico-chemical properties.

### **2.2.3. Functionalization of nanoparticles**

The functionalization of nanoparticles renders them specialized functions such as stimuli responsive behavior, specificity to target molecules etc. Linker agents like silane coupling agents can be used to link an inorganic particle to an organic particle. In this work, the as synthesized BaTiO<sub>3</sub> nanoparticles were functionalized with NH<sub>2</sub> group using silane coupling agent namely (3-aminopropyl) triethoxysilane (APTES). Detailed functionalization procedure is given in the corresponding chapters.

## **2.3. Characterization techniques**

Physico-chemical characterization techniques are important for analyzing the as synthesized materials (nanomaterials) properties like phase, structure, morphology, elemental composition, thickness, successful conjugation or interaction between materials, optical properties, electrical characteristics of the materials and so on. The detailed information on these characteristic tools used in this research project (thesis) and the relevant experimental conditions are given below.

### **2.3.1. X-ray diffraction (XRD)**

X-ray diffractometer (XRD) is one of the physico-chemical characterization tools which is non-destructive in nature, employed for determining the materials phase, size

and purity. The as synthesized samples were measured by using Rigaku X-ray diffractometer (XRD) operated at the power of 40 KeV and 40 mA with  $\text{CuK}\alpha$  radiation in the range of  $10\text{-}80^\circ$  with a step of  $0.02^\circ$ .

### **2.3.2. Raman spectroscopy**

Among the different spectroscopic methods that can efficiently characterize material structures (proteins) and phase, Raman spectroscopy has the potential to identify even ensemble of structures compared to single conformation. It is a non-destructive tool used for detecting the structural defects and disorders, phase of nanomaterial, the interaction or nature of bonding between materials or conjugates. The as prepared materials were measured using the Model: LabRam HR800 micro Raman spectroscope (manufacturer: Horiba Jobin-Yvon, France). The Raman spectrum was operated at an excitation wavelength of 514 nm at the different laser power using  $\text{Ar}^+$  ion laser. The spectral region used for study is  $100\text{-}3500\text{ cm}^{-1}$  and the data were collected using a 10-s data point acquisition time.

### **2.3.3. Fourier transform infrared (FT-IR) spectrometer**

FT-IR spectroscopy is one another characterization technique used for confirming the successful functionalization of nanomaterials or adsorption of molecules on to the material. The samples were measured at room temperature with an FT-IR spectrometer (Thermo Scientific Systems, Nicolet- 6700) using the KBr pellet technique in the range of  $400\text{ to }4000\text{ cm}^{-1}$ .

#### **2.3.4. Field-emission scanning electron microscopy**

FESEM is used for analyzing the as synthesized nanoparticles and materials morphology, structure, thickness (film) and size. The samples were analyzed using FE-SEM (Model: FE-SEM, JSM- 6700F, JEOL Ltd) with a 5 kV of acceleration voltage and 10  $\mu$ A of filament current. Prior to measurement, the as-prepared samples were fixed onto a double-face conductive tape mounted on a metal stud and coated with platinum with a sputter coater (Cressington sputter coater -108 auto).

#### **2.3.5. Energy dispersive X-ray spectroscopy analysis (EDS)**

The elemental composition of the prepared samples was measured using Energy Dispersive X-ray Spectroscopy (EDS). The EDS analysis was done with the Fieldemission Scanning Electron Microscopy (FE-SEM) instrument (Zeiss ultra FE-SEM instruments) with a separate EDS detector (INCA) connected to that instrument.

#### **2.3.6. X-ray photoelectron spectroscopy (XPS)**

The chemical composition and the state of elements present in the outermost part of samples can be determined using X-ray photoelectron spectroscopy (XPS) technique. It is also useful in confirming the successful binding or functionalization of materials by observing the presence of individual components. The samples were measured using the model ESCA- 2000, VG Microtech Ltd and Theta Probe AR-XPS system (Thermo Fisher Scientific, U.K). Here a monochromatic X-ray beam source at 1486.6 eV (Aluminum anode) and 14 kV was used to scan upon the sample surface. A high flux X-ray source with Aluminum anode was used for X-ray generation, and a quartz crystal monochromatic was used to focus and scan the X-ray beam on the sample.

### **2.3.7. UV-Vis spectrophotometer (UV-Vis)**

UV-Vis spectroscopy is one of the important spectroscopic techniques for detecting the optical properties of nanomaterials and also for confirming the interaction or type of bonding between materials by shift in the wavelength (blue or red shift). The samples were measured using (Hewlett Packard HP-8453) with a quartz cuvette path length of 1 cm. The data was collected in the wavelength range of 200 to 800 nm.

### **2.3.8. Frequency variable CV-IV System**

This semiconductor parameter analysis instrument is used for analyzing current-voltage characteristics of the devices. It can be either a two probe system or four probe system. The type of contact (ohmic or schottky) can be determined from the  $I$ - $V$  characteristics graph.  $I$ - $V$  measurements for the as fabricated devices were made using a Frequency Variable CV-IV System (B 1500A).

### **2.3.9. Linear motor**

Linear motor is an instrument used for giving a compressive force. Desired load (force) can be given by changing the acceleration with which the shaft hits the device. This is desirable for analyzing the piezoelectric response of devices (piezoelectric nanogenerators). When a compressive force is applied, the mechanical energy is converted in to electrical energy. The devices were measured using linear motor model (E1100).

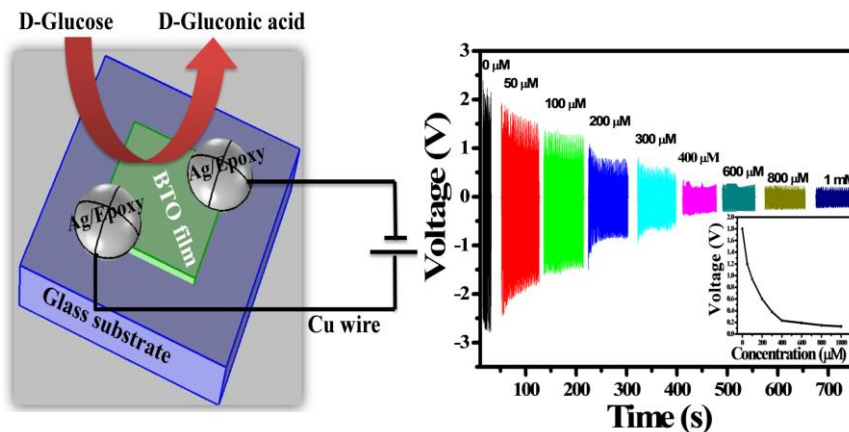
## CHAPTER III

# BaTiO<sub>3</sub> Nanoparticles as Biomaterial Film for Self-Powered Glucose Sensor Application

### Highlights

- ✚ Novel BTO NP's film based self-powered glucose sensor is proposed for the first time.
- ✚ Reasonable sensitivity, LOD ( $\approx 7.94\mu\text{M}$ ) and detection range ( $0.1\mu\text{M}$ - $1\text{mM}$ ) is achieved.
- ✚ Multifunctional properties of BTO NP's have been harnessed for bio-sensing as well as for energy harvesting.
- ✚ Realization of facile, solid-state devices for self-powered, theranostic applications.

### Graphical overview



### 3.1. Introduction

Combination of nanotechnology with biology and material science provides versatile platform for developing state of the art diagnostic devices[1], self-powered systems[2], energy harvesting devices[3], theranostic systems etc. Glucose, being a vital biomolecule in human metabolic process and source of energy, has to be regulated properly, if otherwise leads to diseases like diabetes mellitus. There is an ever-growing demand for glucose sensors with good sensitivity, selectivity, portability, low cost and practical applications. They are found to be inevitable with applications ranging from diagnostics to food industry [5]. Until now, glucose sensors (1<sup>st</sup> to 3<sup>rd</sup> generation) share 85% of the world market of bio-sensors [1] developed by various detection techniques namely electrochemical, chemiluminescence, phenylboronic acid based volumetric changes (hydrogels), solid state (conductivity-based, transistor-like switchable glucose sensing devices) techniques and so on. In recent years, field effect transistor (FET) based devices are been considered good candidates for sensor applications which operates based on the change in resistance across the device when chemical/biochemical species interacts with the biosensing element [6]. Enzymatic glucose sensors have limitations like instability, complicated enzyme immobilization process, sensitivity to pH, temperature and etc. Hence to complement these disadvantages, it is highly desirable to develop a non-enzymatic glucose sensor using eco-friendly and multifunctional metal oxide materials which has low cost, good reproducibility, facile fabrication, user friendly and higher stability resisting aggressive environments like high temperature and pH [7-9].

Numerous metal oxides namely CuO, NiO, MnO<sub>2</sub> were utilized for non-enzymatic glucose detection which have their own merits. In our present work, polycrystalline barium titanate nanoparticles (BaTiO<sub>3</sub>) NP's having transition metal centers making it a potential candidate for non-enzymatic glucose sensor has been harnessed for sensing as well as for energy harvesting (power source). BaTiO<sub>3</sub> NP's find interesting application in the field of energy harvesting [3], drug delivery, in-vivo imaging [10] cancer therapy [11-12] and so on. BTO is a well-known, lead free, ABO<sub>3</sub> perovskite material with high level of inherent piezoelectric properties [3], [13]. First detailed report on crystal structure of BaTiO<sub>3</sub> ferroelectric phase at high temperature was proposed by Megaw (1945) [14] and its interrelationship between anomalous electromechanical, structural, and thermal properties was modeled phenomenology by A.F. Devonshire [15]. Though it is well-known as piezoelectric, dielectric ceramic material, it still remains less exploited as a bio-sensing and theranostic agent. This invoked great interest to study its bio-sensing property by utilizing its semiconducting nature and to couple its piezoelectric property (for harnessing electrical energy) which can be used for driving (power source) the glucose sensor. Self-powered diagnostic systems have advantage over conventional sensors (MEMS/NEMS) in such a way that it can operate without a battery which is made up of highly toxic chemicals with limited life time. BTO nanostructures has comparable and better functional properties than well utilized ZnO nanostructures with respect to high piezoelectric coefficient [3], [13] low dielectric constant, stability at large electric fields and low electrical noise. In near future, BTO can find potential applications in various fields just as ZnO

(semiconductor/piezoelectric) been greatly exploited for sensing [16], [17], self-powered systems [2], [18] for continuous monitoring and so on. Recent report from our group shows BTO nanocubes along with polyvinylidene fluoride (PVDF) matrix has better energy harvesting capability than ZnO and its suitability as self-powered fluid sensor [19].

In our present work, for the first time, a self-powered BTO film based glucose sensor using a metal-semiconductor-metal (M-S-M) device structure has been demonstrated. A high temperature conventional solid state reaction was employed to prepare tetragonal crystalline phase of BaTiO<sub>3</sub> nanoparticles ( $\geq 100$  nm). I-V based detection technique was utilized for confirming the glucose sensing ability of the BTO film based glucose sensor with constant bias voltage under different glucose concentrations. We further extended to self-powered glucose sensor studies by establishing parallel connection between BTO film based glucose sensor and flexible piezoelectric nanogenerator (PNG). The PNG was made up of BTO nanocubes along with PVDF polymer formed as a thin film and two electrodes were attached on both sides of the film for electrical connection. Frequency dependent energy harvesting of PNG with constant mechanical load (11 N) is reported. Generated piezoelectric potential was used to drive the BTO film based sensor and with increasing glucose concentrations the sensor exhibits voltage decrement behavior. The proposed self-powered glucose sensor and conventional glucose sensor have similar electrical behavior where conductivity increases with increase in glucose concentrations. Proposed working mechanism for glucose sensor using energy band diagram of M-S-M device structure

has been discussed. This work demonstrates a promising approach for other relevant theranostic applications in the near future.

## **3.2. Experimental details**

### **3.2.1 Synthesis of BaTiO<sub>3</sub> Nanoparticles**

BTO nanoparticles used in this experiment were synthesized via conventional solid state reaction method. The High-purity precursors BaCO<sub>3</sub> (99.95%, High purity chemicals) and TiO<sub>2</sub> (98%, DAEJUNG chemicals) were taken according to the atomic ratio of BaTiO<sub>3</sub>. Raw materials were mixed well by hand-grinding using a pestle and mortar in acetone medium for 30 minutes to achieve the homogeneous powder and placed inside a combustion alumina boat, heated to 1200 °C for 2 hr in the open tube furnace at a heating rate of 2.5 °C/min. The obtained final product was taken out of the furnace after reaction and allowed to cool naturally. The as synthesized particles have random shape ranging few 100 nm in size with tetragonal phase, confirmed by Raman and XRD analysis.

### **3.2.2. Fabrication of BaTiO<sub>3</sub> NP's film based glucose sensor**

The schematic representation of BTO film based glucose sensor is given in Fig.3.1. BTO NP's film based glucose sensor was fabricated by attaching two silver electrodes onto the BTO film. PVA (poly vinyl alcohol) polymer was used as a matrix to assist in BTO film formation. A facile, drop casting method was adopted to fabricate a thick film of BTO nanoparticles on a glass slide. A homogeneous solution was achieved by dispersing highly crystalline BTO NP's of 20 % (W/V) (>100 nm) in 5% (W/V) of PVA matrix.

This composite solution was then drop casted on to a clean glass slide within a pre-defined area (1 cm x 1 cm) and heat treated at 150 °C for 1 hour in a hot oven so that a uniform, polycrystalline film is formed with maximum amount (95%) of PVA matrix been removed. Silver paste was used to make contacts diagonally with the film and electrical contacts were made using copper wires. An epoxy layer was used to cover the electrodes completely in order to avoid possible contacting between electrodes and glucose solution. This Ag-BTO-Ag device could be treated as a metal-semiconductor-metal (M-S-M) structure[1],[20-21].

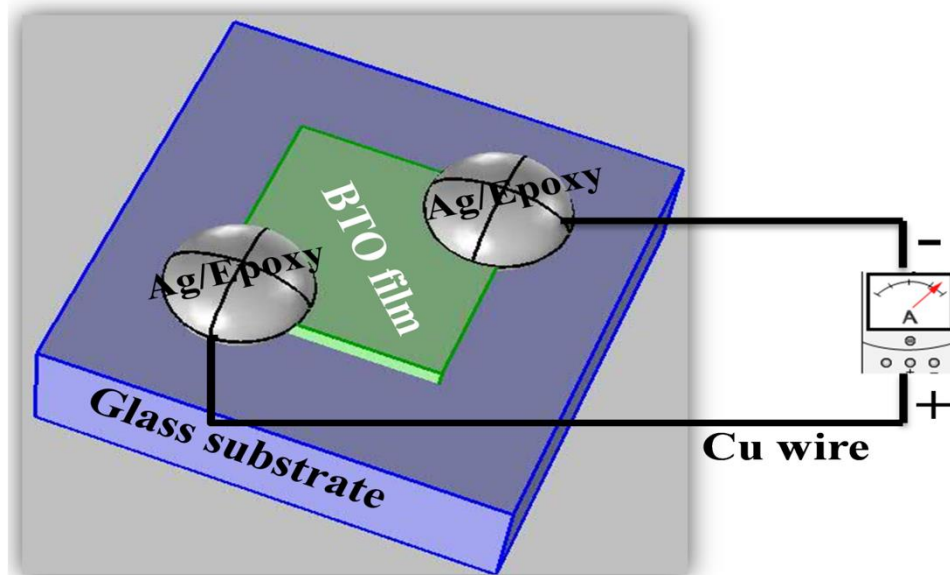


**Fig. 3.1.** Schematic of BTO NP's film based glucose sensor.

### 3.2.3 Fabrication of piezoelectric nanogenerator (PNG)

The PNG comprises of piezoelectric composite film (BTO nanocubes/PVDF matrix), two Al electrodes and a packaging layer[19]. The composite film was fabricated using

the solution cast technique. Initially, clear, transparent PVDF solution was prepared by mixing 1 gm PVDF powder, 5 ml DMF solution and 3 ml acetone by subjecting to 1 hr ultrasonication. After cooling down to room temperature, the prepared PVDF solution was mixed with 25 wt% of BTO nanocubes and ultrasonicated for 1 hr to achieve homogeneous white solution. As synthesized composite solution was poured into a clean glass petridish and heat treated at 70 °C for overnight in a hot oven. The obtained composite film was peeled off from the petri dish and taken according to the required dimensions for fabricating PNG device. Highly crystalline BTO nanocubes were synthesized via molten salt method [19]. In present work, PVDF is considered as supporting polymer for BTO nanocubes to fabricate a composite film. The fabricated composite film was taken according to the PNG device dimensions (2.5 cm X 2.5 cm). Two Al electrodes were deposited (by thermal evaporation) on top and bottom of composite film for acquiring the developed charge carriers. For external circuitry, two copper wires were attached on top and bottom of the Al electrodes by using the silver paste and heat treated at 60 °C for 15 minutes. Finally, the fabricated Al/PVDF-BTO nanocubes/Al has been packed with PDMS matrix layer and heat treated at 70 °C for 30 minutes to protect the device from physical damage, interactions with environments such as humidity and temperature. The fabricated device was electrically poled by applying 8 kV for 24 hr at room temperature for improving polarization property. Similar method was adopted to fabricate pure PVDF (without BTO nanocubes) based nanogenerator.

### 3.2.4 Characterization and measurement

The crystalline phase formation of BTO nanoparticles and BTO-PVA film were confirmed with an X-ray diffractometer (XRD, Rigaku) operated at 40 kV and a current of 10 mA pattern recorded using Cu K $\alpha$  radiation ( $2\theta$  range from  $20^\circ$  to  $80^\circ$ ) at room temperature. Raman spectra for all samples were recorded from 100 to 3000  $\text{cm}^{-1}$  with an excitation source of 514 nm using a high throughput single stage spectrometer (Lab RAM HR Evaluation, Japan). The surface morphology of as prepared samples were characterized by a field emission-scanning electron microscope (FE-SEM, JEOL, and JSM-6700F). The I-V measurements were made using Frequency Variable CV-IV System (B 1500A). The open circuit voltage ( $V_{oc}$ ) and short circuit current ( $I_{sc}$ ) of PNG were recorded by a nanovoltmeter (Keithley 2182A) and picoammeter (Keithley 6485) respectively. Measurement of PNG's output was triggered by an electrodynamic shaker (ET-126) with different frequencies (3, 11, and 21 Hz) at fixed input amplitude of 5 V.

### 3.3. Results and discussion

#### 3.3.1. BTO NP's film based sensor's structural characterization

The crystalline phase of BTO NP's was confirmed by XRD pattern and Raman spectra. The XRD spectra of BTO NP's matched well with the reference ICDD 98-001-3771 pattern and tetragonal phase of BTO has been confirmed by the splitting nature of diffraction peak at  $45^\circ$  represented as (200/002) [22] as shown in Fig.3.2 a . At the same time, strong peaks at 305  $\text{cm}^{-1}$  and 518  $\text{cm}^{-1}$  in Raman spectra of BTO NP's indicates the presence of  $\text{Ti}^{4+}$  ion in parent lattice and confirms the tetragonal phase [19] as given in

Fig.3.2 b. There is no crystalline phase variation between the diffraction peaks of BTO and BTO-PVA composite film which indicates that most of the PVA matrix has been removed during the heat treatment as shown in Fig.3.2 a.

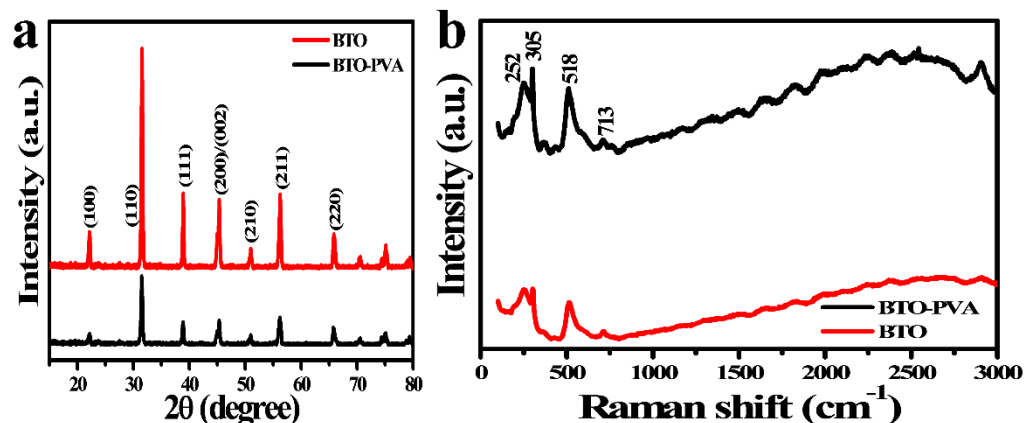


**Fig. 3.2.** (a) X-ray diffraction patterns of pure crystalline BTO NP's (> 100 nm) and BTO NP's film *via* PVA matrix. (b) Raman spectrum of pristine BTO NP's and BTO-PVA film (after heat treatment at 150 °C/ 1hr).

The active area of glucose sensor is 1 cm<sup>2</sup> and the solubility of the film was tested by immersing in 0.1M PBS (pH =7) bath for 24 hr. The film was highly stable without any dispersion in PBS bath. The thickness of the film was measured to be around ~ 200 μm using FE-SEM (Fig. 3.3 a). Fig. 3.3 b shows the surface morphology of as synthesized BTO-PVA film with good crystallinity and random particle size ≥ 100 nm been well distributed. FE-SEM images showing surface morphology of polycrystalline BTO NP's and PVA film is given in Fig. 3.3 c, d respectively. The XRD

pattern and Raman spectra for both BTO NP's and film has good correlation confirming the single tetragonal phase without any secondary impurity peaks (like BaCO<sub>3</sub>).

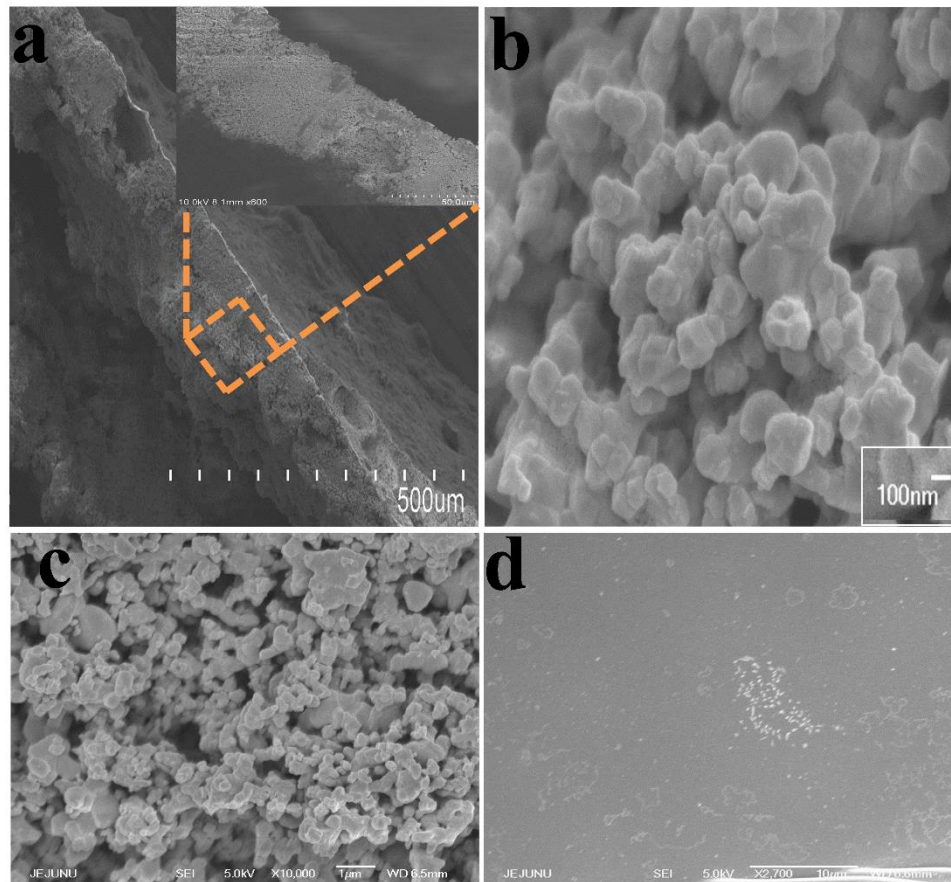


**Fig. 3.3.** FE-SEM images of (a) BTO film (cross-sectional view) having thickness ~ 200 μm and (b) Surface morphology of BTO film after heat treatment at 150 °C for 1 hr. (c) Random structured BTO nanoparticles at 1 μm scale. (d) FESEM image of PVA film at 10 μm scale.

### 3.3.2. I-V characterization for glucose measurement

The electrical response (I-V curves) of BTO film based glucose sensor in the absence and presence of glucose at an applied bias voltage of  $\pm 4$  V is given in Fig. 3.4 a. Initially, in the absence of glucose, the device I-V curve shows ohmic contact behavior (resistor) with 150 pA current at an applied bias voltage of  $\pm 4$  V. The ohmic nature of sensor deviated to non-ohmic nature (schottky) in the presence of glucose molecules (0.1  $\mu$ M to 1 mM), as shown in Fig. 3.4 a. The current response of the sensor increased significantly from pA to several  $\mu$ A with increase in glucose concentrations (0  $\mu$ M to 1 mM). BTO films with different weight ratio of BTO NP's (5, 10, 15 and 20% weight/volume (W/V)) in fixed PVA weight percentage were made and their corresponding glucose sensing behavior was observed (Fig. 3.5 a-c). Correlation between the sensor's current response, BTO NP's concentration and glucose concentration is illustrated in the form of 3D graph in Fig. 3.4 b.

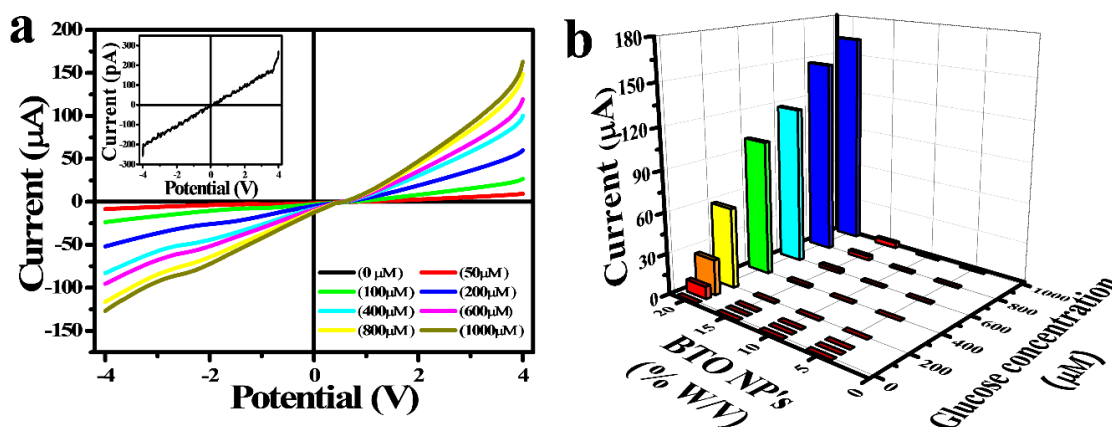


**Fig. 3.4.** Electrical response of BTO NP's film based glucose sensor. (a) I-V characterization of glucose sensor (20 % W/V of BTO NP's) in absence (inset Fig.) and

presence of glucose (50  $\mu\text{M}$  to 1 mM) . **(b)** 3D graphical analysis of sensor's current response under different concentrations of BTO NP's (5, 10, 15, 20 % (W/V)) and glucose.

As expected, BTO film based sensor with 20% W/V has higher current response (pA to several  $\mu\text{A}$ ) for glucose concentrations (0 $\mu\text{M}$  to 1mM) compared to BTO film based sensor with 5% W/V which has lower current response (pA to several nA) for similar glucose concentration range (Fig. 3.5 a-c). This indicates that 20% W/V based device has higher sensing ability as compared to other three devices. Here, the % W/V of BTO NP's was fixed not only based on sensor performance but also by factors like uniform film formation capability. BTO NP's greater than 20% W/V, resulted in non-uniform film formation and thickness due to agglomeration of particles in limited amount of PVA matrix (wt%). Hence, BTO film based sensor with 20% W/V was used for further experiments. The correlation between BTO NP's concentration and glucose sensing efficiency with respect to the sensor's current output at a bias voltage of + 4 V for lower (50  $\mu\text{M}$ ) and higher (1000  $\mu\text{M}$ ) glucose concentrations is depicted as 2D graph in Fig. 3.5 d.

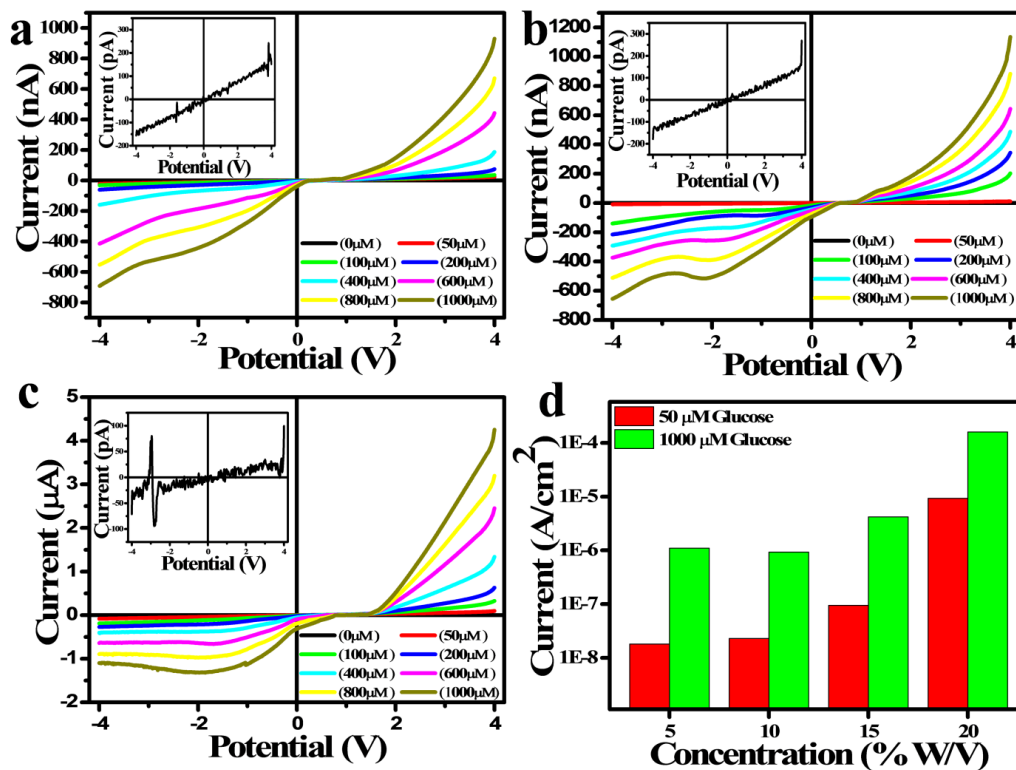


**Fig. 3.5.** I-V curves of BTO NP's film based glucose sensor (different weight ratios) under various glucose concentrations ranging from 0  $\mu\text{M}$  to 1000  $\mu\text{M}$ . (a) 5 % (W/V) of BTO NP's film based device (b) 10 % (W/V) of BTO NP's film based device (c) 15 % (W/V) of BTO NP's film based device. (d) 2D graph depicting the correlation between BTO NP's concentration and glucose sensing efficiency with respect to the sensor's current output at a bias voltage of + 4 V for lower (50  $\mu\text{M}$ ) and higher (1000  $\mu\text{M}$ ) glucose concentrations.

### 3.3.3 Proposed working mechanism of BTO NP's film based sensor

The sensing mechanism is directly based on change in conductivity of the BTO NP's film with respect to the change in glucose concentration from 0  $\mu\text{M}$  to 1 mM

respectively. Here the glucose molecule acts as an electron donor to the BTO NP's film decreasing the depletion layer width across the metal- semiconductor interface. Glucose molecules has lewis base site namely OH<sup>-</sup> group whereas BTO NP's film has Ba<sup>2+</sup> and Ti<sup>4+</sup> ionic species which are lewis acids. When glucose interacts with BTO NP's film, the lewis base (OH<sup>-</sup> groups) reacts with lewis acid sites (Ba<sup>2+</sup> and Ti<sup>4+</sup>) on BTO NP's and release electrons (e<sup>-</sup>) [23-24]. This leads to the chemisorption of glucose molecules on to BTO NP's whereby glucose gets oxidized and releases electrons. These released electrons will increase the charge carrier density of the film resulting in lowering the schottky barrier height at the drain side ( $\Phi'_d$ ) significantly increasing the output current of BTO film based glucose sensor. Here the metal(M) - semiconductor(S)- metal (M) interface has been formed by BTO film (n-type) and silver (Ag) electrodes schematically shown in Fig. 3.6 a-b.

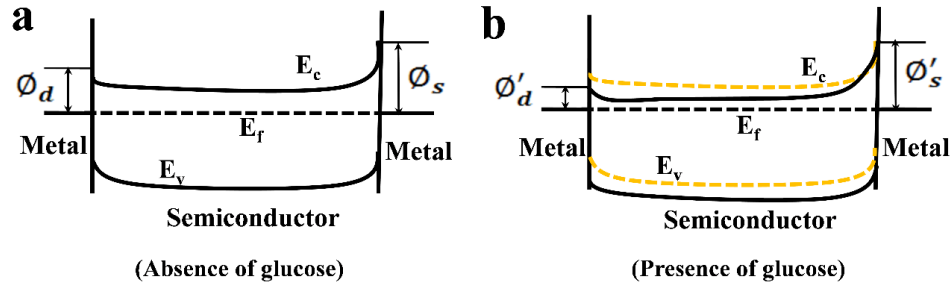


**Fig. 3.6.** Proposed working mechanism (using energy band diagram) of BTO NP's film based glucose sensor. **(a)** Energy band diagram in absence of glucose (presented as solid black lines in Fig. 3.6 a and dashed yellow lines in Fig. 3.6 b). **(b)** Energy band diagram in presence of glucose (presented as solid black lines in Fig. 3.6 b).

The proposed working principle can be illustrated using band structure of device (Fig. 3.6 a-b), which is almost analogous to ZnO energy band analysis due to its similar band gaps ( $\approx 3.2$  eV) [25]. The energy barrier at M-S interface is relatively low since the work function of silver (4.26 eV) do not vary significantly from the electron affinity of BTO as shown in Fig. 3.6 a. Fig. 3.6 b shows the band structure of the BTO film based device in the presence of glucose molecules. Glucose molecules releases  $e^-$  to BTO NP's film which will increase the charge carrier density of the film resulting in lowering the schottky barrier height at the drain side ( $\Phi'_d$ ) thus significantly increasing the output current of BTO film based glucose sensor as shown in Fig. 3.6 b. Thus with increase in glucose concentrations, the device output current increases.

### 3.3.4. I-T characteristics of the sensor

To estimate the sensitivity and low detection limit (LOD) of BTO film based glucose sensor we carried out current vs time analysis (I-T curve) under lower (0.1 $\mu$ M to 30  $\mu$ M) and higher glucose concentration ranges (50 $\mu$ M to 1mM) at an applied bias voltage of +0.5 V. For lower glucose concentration range (0.1 $\mu$ M to 30  $\mu$ M), linear current response with increasing glucose concentrations could be observed as shown in Fig. 3.6 a. The inset shows the calibration plot indicating the linearity between glucose concentration and current with a correlation coefficient of 0.9843 and the limit of detection (LOD) obtained is 7.941  $\mu$ M. The LOD was calculated from the calibration curve by  $3s/m$  method ( $s$  is the standard deviation,  $m$  is the slope of the calibration curve) [26]. The sensitivity of BTO film based glucose sensor is found to be 23.79 $\mu$ A/mM  $\text{cm}^2$ . Similar kind of response was observed for higher range of glucose concentration (50 $\mu$ M to 1mM) and the observed calibration plot with correlation coefficient 0.9913 is as shown in Fig. 3.6 b. Single calibration plot including two linear fittings for lower and higher glucose concentration ranges (0.1  $\mu$ M – 1000  $\mu$ M) is given in Fig. 3.6 c. It suggests that the proposed BTO film based glucose sensor has a good linear response at lower and higher range of glucose concentrations. Moreover, the initial response for proposed glucose sensor is around 30 seconds and maximized current (saturated current response) was observed in < 2 minutes for each concentration. The response time was not only depending on the inherent glucose sensing property of BTO NP's but also on the thickness of BTO film.

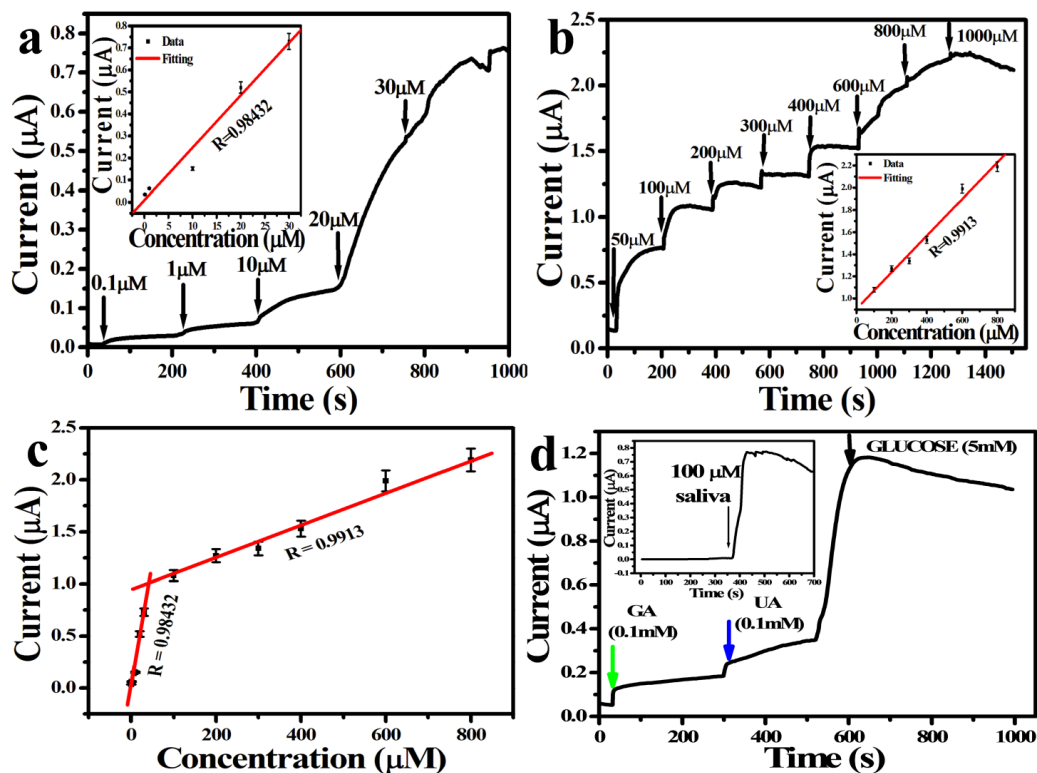


**Fig. 3.7.** Current-time response of BTO NP's film based glucose sensor at an applied bias voltage of +0.5 V. **(a)** For lower glucose concentration range (0 μM to 30 μM) having correlation coefficient of 0.9843. **(b)** For higher glucose concentration range (50 μM to 1000 μM) having correlation coefficient of 0.9913. **(c)** Single calibration plot including two linear fittings for lower and higher glucose concentration ranges (0.1 μM – 1000 μM). **(d)** I-T curve for interference study with 5 mM glucose and interferents such as 0.1 mM galactose and 0.1 mM uric acid. (Inset shows the current response of the sensor for human saliva spiked with 100 μM of glucose).

Main factor controlling the response time is the film thickness. The glucose sensor is made up of thick film of BTO nanoparticles. If film thickness is high, it results

in too long electronic transmission paths [16]. This might be the main reason for the delayed response time. Here, we assisted the drop casting method to fabricate BTO nanoparticles film. The thickness is around  $\approx 200 \mu\text{m}$  and very typical to control as compared to other existing techniques like physical vapor deposition (PVD), hydrothermal techniques etc. Even though the film thickness is high, the proposed sensor has sensitivity, LOD and responsivity comparable (or higher) to previous published reports [Table 1]. The response time of glucose sensor based on BTO NP's has the possibility to improve when fabricated with single micro wires around  $< 50 \mu\text{m}$  length or by directly growing BTO nanostructures on substrates. In near future these techniques will be implemented to overcome this issue.

### **3.3.5. Interference and real sample analysis**

In normal physiological sample, level of glucose is much higher than the level of interfering species. The glucose level is 3-8 mM and the interfering species level is not more than 0.1 mM. Though the level of interference species is low compared to glucose, the current response produced by them are comparable to that produced by glucose since interference species have higher electron transfer rate at an applied potential and hence, interference study is necessary to check the selectivity of the sensor [27-30]. Therefore, to check the selectivity of the sensor, 5 mM of glucose (the level of glucose in normal physiological sample) and 0.1 mM of interfering species namely galactose and uric acid (level of interferents in normal physiological sample) were taken for comparison [8], [31-32] Conclusion from this study is reliable as it is equivalent to the normal

physiological conditions. From I-T response curve as shown in Fig. 3.6 d, it could be observed that, galactose and uric acid had negligible current response when compared to glucose. Addition of glucose on to the device had approximately four fold increments in current response compared to the current response obtained with addition of galactose and uric acid. Additionally, we have also studied the I-V characteristics of the glucose sensor in the presence of ascorbic acid and comparative analysis of the current response of glucose to that of the ascorbic acid (~ fourfold difference) is given in Fig. 3.7 a-c.

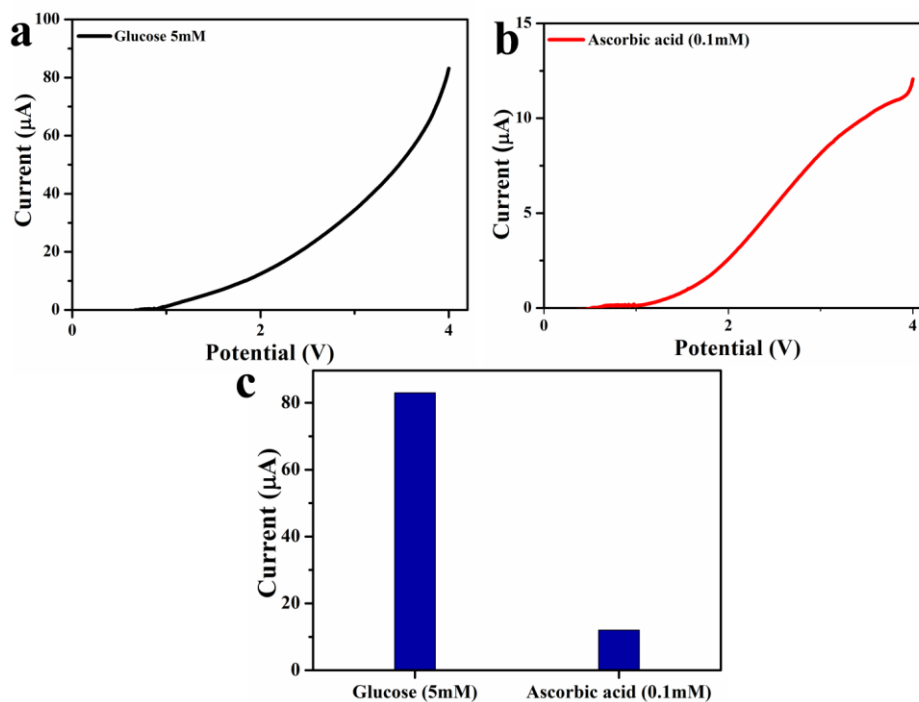


**Fig. 3.8.** Interference study (glucose vs ascorbic acid). I-V curves of BTO NP's film based glucose sensor at a potential window of 0 to +4V under (a) 5 mM glucose (b) 0.1 mM ascorbic acid. (c) Comparative analysis for current response of BTO NP's film based glucose sensor measured at +4V under 5 mM glucose and 0.1mM ascorbic acid.

Hence, the proposed sensor has good specificity to glucose even in the presence of potent interfering species. For real time glucose monitoring, human saliva sample was subjected to study. The inset of Fig. 3.6 d shows sensor current response to human saliva spiked with 100  $\mu\text{M}$  of glucose. This is compared with calibration plot for higher glucose concentrations (50 $\mu\text{M}$  to 1mM) (Fig. 3.6 b) and the obtained recovery percentage of glucose was found to be  $\sim 87.5\%$  respectively. The efficiency of the sensor can be further improved by reducing the matrix effect and improving the wettability of the film in reference to the saliva sample. With further optimization, there is a feasibility of real sample analysis of glucose using saliva making the sensor to be applicable for non-invasive glucose testing.

### **3.3.6. Working mechanism of PNG**

In our present work, we utilized a flexible PNG using composite film (BTO nanocubes/PVDF) whose mechanical energy can be converted to electrical energy [19]. The schematic representation for generating piezoelectric potential from PNG device when a mechanical force is acted up on is shown in Fig. 3.8 a. The observed peak to peak open circuit voltage (and short circuit current) for PNG device upon the mechanical force 11 N with a cyclic frequency of 3Hz is around  $\approx 3\text{ V}$  ( $\approx 750\text{ nA}$ ) and this may be due to the capacitance behaviour of composite film. This electrical output voltage increased to 5 V (900 nA), and 11 V (1.7  $\mu\text{A}$ ) by increasing the variable cyclic frequencies to 11 Hz and 21 Hz respectively at constant mechanical force (11 N) as shown in Fig. 3.8 b-c. This indicates the frequency dependent electrical response of

PNG device. The working mechanism mainly depends on the stress induced poling effect i.e. orientation of electric dipoles in PVDF/BTO nanocubes composite film. The generation of piezoelectric potential across the Al electrodes is due to perpendicular force acting on PNG device, which drives the flow of electrons through external circuitry. The development of charge carriers will depend on electrical poling, frequency dependent mechanical load, piezoelectric nanostructures in polymer and piezoelectric charge coefficient of film. We experimentally proved that the generated piezoelectric potential have the capability to drive five commercial green LEDs (Inset Fig. 3.8 d).

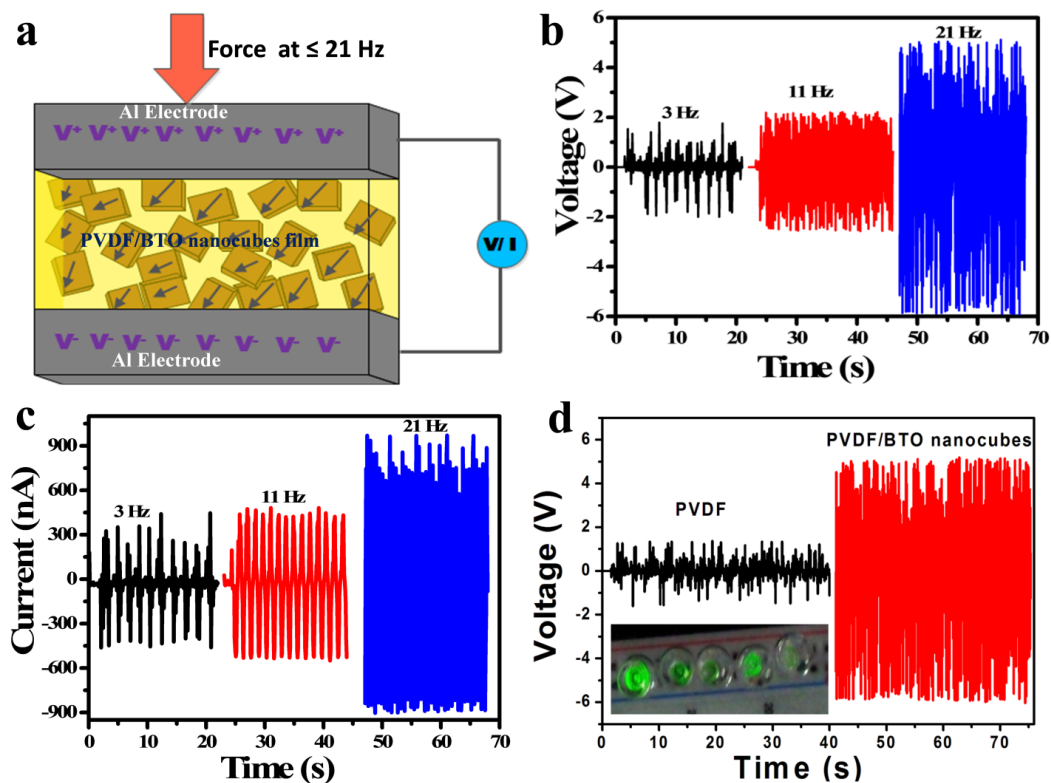


**Fig. 3.9.** Electrical response of PNG device. (a) Schematic diagram represents the measurement of PNG device output upon mechanical force of 11N. (b, c) Frequency

dependent open circuit voltage and short circuit current of composite PNG device upon the mechanical load (11N). **(d)** Comparative open circuit voltage of PVDF and PVDF/BTO nanocubes upon on mechanical load (11 N) at a frequency of 21 Hz.

To investigate the effect (role) of PVDF for energy harvesting, we fabricated PVDF (without BTO nanocubes) film based devices and characterized with constant force 11 N at a cyclic frequency of 21 Hz as shown in Fig. 3.8 d (Fig. 3.9 a). These devices have very less output as compared to the composite film PNG output. So the major contribution for harvesting energy is from the piezoelectric nature of BTO nanocubes. Here PVDF has two roles, one as a supporting polymer to fabricate desired film along with piezoelectric BTO nanocubes and other as a piezoelectric material (considerable piezoelectric property) that can possibly contribute to (or increase) energy conversion along with BTO nanocubes. The evaluation of the PNG device stability around 500 seconds with a mechanical load 11 N having cyclic frequency of 21 Hz shows no degradation in the open circuit voltage confirming PNG's good stability (Fig. 3.9 b).

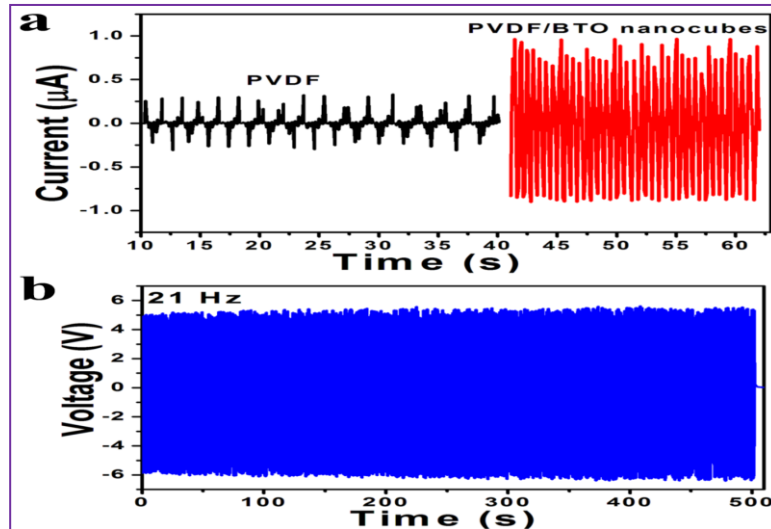


**Fig. 3.10.** (a) Comparison of short circuit current for PVDF and composite film (PVDF/BTO nanocubes) based PNG devices upon the mechanical force 11 N at a cyclic frequency 21 Hz. (b) Stability test for the composite PNG device during 500 seconds upon the mechanical force 11 N at a cyclic frequency 21 Hz.

### 3.3.7. Integration of PNG and glucose sensor

In our present work, the self-powered glucose sensor (battery less) was demonstrated by utilizing the energy harvested (peak to peak  $V_{OC} \approx 5$  V @ 11 N and 11 Hz) from PNG device to drive the BTO film based glucose sensor (M-S-M device configuration) by establishing a parallel connection between them as shown in Fig. 3.10 a. Here the voltage drop across the sensor was measured as a function of different glucose concentrations (0  $\mu$ M to 1 mM) as shown in Fig. 3.10 b.

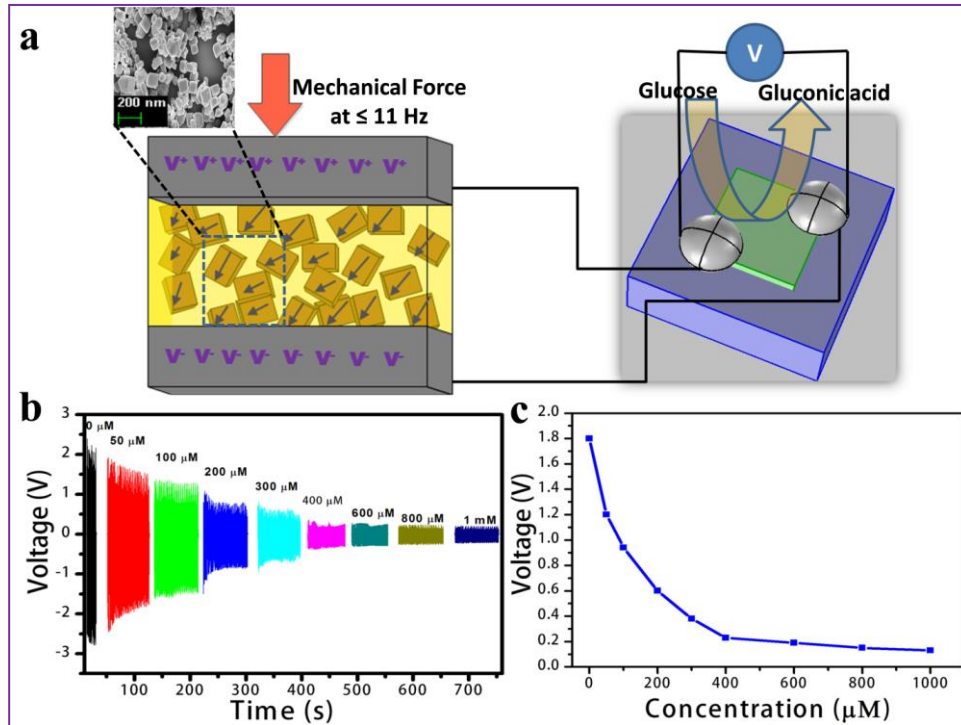


**Fig. 3.11.** (a) Schematic representation of self-powered glucose sensor by establishing parallel connection between the PNG device ( $\text{BaTiO}_3$  nanocubes / PVDF film) and BTO NP's film based glucose sensor. The inset shows the BTO nanocubes at 200 nm scale. (b) The open circuit potential drop across glucose sensor was measured as a function of different glucose concentrations ( $0 \mu\text{M}$  to  $1 \text{mM}$ ). (c) The non-linear behavior of self-powered glucose sensor under different glucose concentrations ( $0 \mu\text{M}$  to  $1 \text{mM}$ ).

In absence of glucose, the sensor's resistance is approximately equal to the PNG device resistance ( $\approx 1$  to  $50 \text{M}\Omega$ ). It can be confirmed by observing the PNG output and PNG/glucose sensor (self-powered) output (under  $0 \mu\text{M}$  glucose), which are equal upon the mechanical load  $11 \text{N}$  at  $11 \text{Hz}$  frequency as shown in Fig. 3.11. With increasing concentrations of glucose, the PNG/glucose sensor output shows decreasing trend at

same force (11 N at 11 Hz), which is quite less compared to pure PNG output indicating that the glucose sensor's resistance drastically decreases with increasing glucose concentrations. For qualitative analysis the glucose sensor's response was evaluated by considering positive peak output value (in terms of average voltage) with respect to glucose concentrations upon the constant mechanical force (11 N @ 11 Hz) as shown in Fig. 3.10 c. Interestingly we observed a slight non-linear behavior of glucose sensor (self-powered) when it was powered by the PNG device with constant force (Fig. 3.10 c).

**Table 3.1. Comparison of analytical parameters of proposed BTO NP's film based glucose sensor with well reported glucose biosensors (different detection techniques).**

Material employed	Detection technique	Sensitivity ( $\mu\text{A}/\text{mM cm}^2$ )	Detection limit	Linear range	Reference
BaTiO <sub>3</sub> film	I-V technique (non-enzymatic)	23.79	7.941 $\mu\text{M}$	0.1 $\mu\text{M}$ – 1 mM	<b>Present work</b> [4]
Spherical ZnO	Amperometric (non-enzymatic)	64.29	0.82 mM	1 to 10 mM	
ZnO nanotube	Amperometric (enzymatic)	21.7	1 $\mu\text{M}$	50 $\mu\text{M}$ to 12 mM	[33]
PtNCs/graphene	Amperometric (non-enzymatic)	1.21	30 $\mu\text{M}$	-	[34]
Pyramid-shaped porous ZnO	Amperometric (enzymatic)	-	10 $\mu\text{M}$	0.05 to 8.2 mM	[35]
Nanostructured TiO <sub>2</sub>	Amperometric (enzymatic)	0.3	-	150 $\mu\text{M}$ to 1.2 mM	[36]
PtNi-Graphene	Amperometric (enzymatic)	20.42	10 $\mu\text{M}$	upto 35mM	[8]
Lamellar-ridge-Au	Amperometric (non-enzymatic)	29	0.87 $\mu\text{M}$	2 $\mu\text{M}$ to 23mM	[32]
Pt- nanotubule arrays	Amperometric (enzymatic)	0.1	1 $\mu\text{M}$	2-14 mM	[7]
Boronic acid functionalized CNT	FET (non-enzymatic)	-	300nM	1 $\mu\text{M}$ -100 mM	[37]
Ni/VCNTs/G	Amperometric (non-enzymatic)	950.6	30 $\mu\text{M}$ .	0.05 to 1.0 mM	[31]

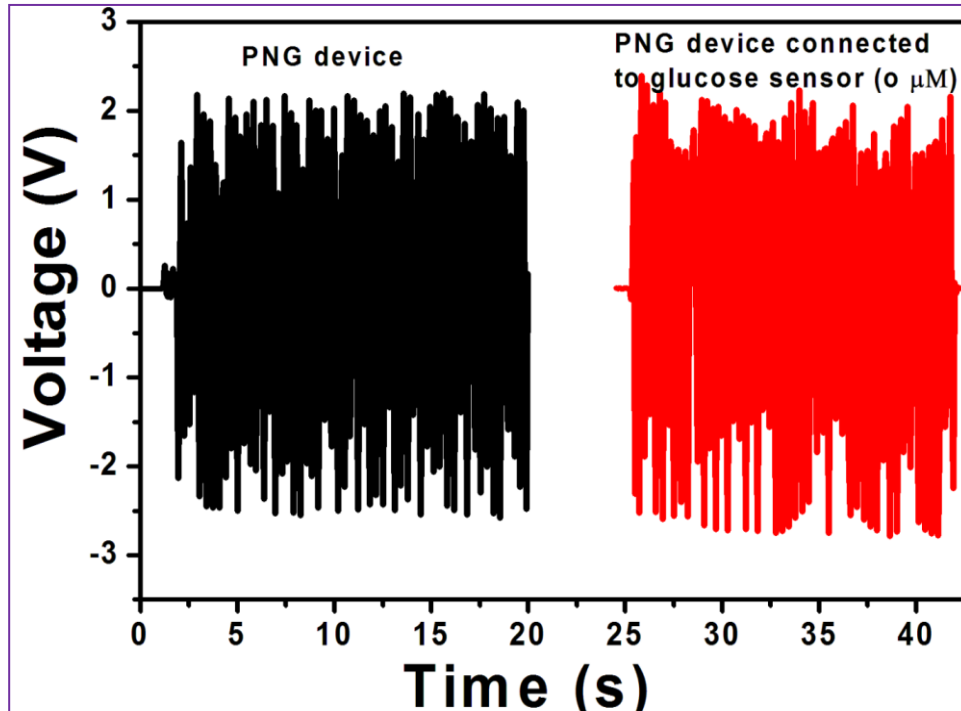


**Fig. 3.12.** Open circuit voltage ( $V_{oc}$ ) of PNG device and self-powered glucose sensor (under  $0 \mu\text{M}$  glucose concentration) upon the mechanical load  $11 \text{ N}$  at frequency  $11 \text{ Hz}$ .

But from the I-T characteristics of the sensor (Fig. 3.6 a-b), we observed a linear relationship (under DC bias voltage of  $+0.5\text{V}$ ) between the glucose concentration and the current response in both lower and higher ranges of glucose concentration. The non-linearity of self-powered glucose sensor is possibly due to the instantaneous voltage generated from PNG device upon the mechanical force with periodic intervals. Here, small time lag behavior is observed between the PNG device output (whenever mechanical force is acted on device) and continuous glucose sensor response. This may be the reason behind the nonlinearity of self-powered glucose sensor, even though sensor response is linear. All the above mentioned results indicate that the proposed

multifunctional polycrystalline BTO NP's has glucose sensing as well as energy harvesting capability to serve as a reliable self-powered bio-sensor.

### **3.4. Conclusions**

Facile fabrication of self-powered BTO NP's film based device (M-S-M device configuration) as glucose sensor has been reported for the first time. The proposed work is cost effective, eco-friendly and non-enzymatic. The performance of BTO film based glucose sensor depends on factors like concentration of BTO NP's, film thickness, fabrication temperature and resistance of film. The recovery percentage of glucose from human saliva is around 87.5 % and possible to improve by reducing the matrix effect. Comparing the physiological level of glucose ( $3\pm 8$  mM) to that of the interfering agents (0.1 mM), the sensitivity ( $23.79 \mu\text{A}/\text{mM}^1 \text{ cm}^2$ ), low detection limit ( $7.941 \mu\text{M}$ ) and linear concentration range ( $0.1\mu\text{M}$  to  $1000\mu\text{M}$ ) are obviously good enough for clinical applications without enzymes. Further investigations on the properties of barium titanate as theranostic agent and their practical applications as self-powered systems are in progress.

## References

- [1] R. Yu, C. Pan, J. Chen, G. Zhu, Z.L. Wang, Enhanced performance of a ZnO nanowire-based self-powered glucose sensor by piezotronic effect, *Adv. Funct. Mater.* 23 (2013) 5868–5874. doi:10.1002/adfm.201300593.
- [2] Y. Zhao, Y. Fu, P. Wang, L. Xing, X. Xue, Highly stable piezo-immunoglobulin-biosensing of a SiO<sub>2</sub>/ZnO nanogenerator as a self-powered/active biosensor arising from the field effect influenced piezoelectric screening effect., *Nanoscale.* 7 (2015) 1904–1911. doi:10.1039/c4nr06461e.
- [3] K. Il Park, M. Lee, Y. Liu, S. Moon, G.T. Hwang, G. Zhu, et al., Flexible nanocomposite generator made of BaTiO<sub>3</sub> nanoparticles and graphitic carbons, *Adv. Mater.* 24 (2012) 2999–3004. doi:10.1002/adma.201200105.
- [4] A. Tarlani, M. Fallah, B. Lotfi, A. Khazraei, S. Golsanamlou, J. Muzart, et al., New ZnO nanostructures as non-enzymatic glucose biosensors, *Biosens. Bioelectron.* 67 (2015) 601–607. doi:10.1016/j.bios.2014.09.063.
- [5] J. Wang, Electrochemical glucose biosensors, *Chem. Rev.* 108 (2008) 814–825. doi:10.1016/B978-012373738-0.50005-2.
- [6] M. Ahmad, C. Pan, Z. Luo, J. Zhu, A single ZnO nanofiber-based highly sensitive amperometric glucose biosensor, *J. Phys. Chem. C.* 114 (2010) 9308–9313.
- [7] J.H. Yuan, K. Wang, X.H. Xia, Highly Ordered Platinum-Nanotubule Arrays for Amperometric Glucose Sensing, *Adv. Funct. Mater.* 15 (2005) 803–809. doi:10.1002/adfm.200400321.

- [8] H. Gao, F. Xiao, C.B. Ching, H. Duan, One-step electrochemical synthesis of PtNi nanoparticle-graphene nanocomposites for nonenzymatic amperometric glucose detection, *ACS Appl. Mater. Interfaces*. 3 (2011) 3049–3057. doi:10.1021/am200563f.
- [9] S. Guo, D. Wen, Y. Zhai, S. Dong, E. Wang, Platinum nanoparticle ensemble-on-graphene hybrid nanosheet: One-pot, rapid synthesis, and used as new electrode material for electrochemical sensing, *ACS Nano*. 4 (2010) 3959–3968. doi:10.1021/nn100852h.
- [10] J. Čulić-Viskota, W.P. Dempsey, S.E. Fraser, P. Pantazis, Surface functionalization of barium titanate SHG nanoprobe for in vivo imaging in zebrafish, *Nat. Protoc.* 7 (2012) 1618–1633. doi:10.1038/nprot.2012.087.
- [11] E. FarrokhTakin, G. Ciofani, G.L. Puleo, G. de Vito, C. Filippeschi, B. Mazzolai, et al., Barium titanate core-gold shell nanoparticles for hyperthermia treatments., *Int. J. Nanomedicine*. 8 (2013) 2319–2331. doi:10.2147/IJN.S45654.
- [12] G. Ciofani, S. Danti, D. D'Alessandro, S. Moscato, M. Petrini, A. Menciassi, Barium Titanate Nanoparticles: Highly Cytocompatible Dispersions in Glycol-chitosan and Doxorubicin Complexes for Cancer Therapy, *Nanoscale Res. Lett.* 5 (2010) 1093–1101. doi:10.1007/s11671-010-9607-0.
- [13] Z.H. Lin, Y. Yang, J.M. Wu, Y. Liu, F. Zhang, Z.L. Wang, BaTiO<sub>3</sub> Nanotubes-Based Flexible and Transparent Nanogenerators, *J. Phys. Chem. Lett.* 3 (2012) 3599–3604. doi:10.1021/jz301805f.
- [14] H.D. Megaw, W.F. Forrester, R.M. Hinde, Crystal Structure of Barium Titanate,

- Nature. 155 (1945) 484–485.
- [15] A.F. Devonshire, Theory of barium titanate- part I, Philosophical Magazine 7 (1949) 1040-1063. doi:10.1080/14786444908561372.
- [16] C. Zhou, L. Xu, J. Song, R. Xing, S. Xu, D. Liu, et al., Ultrasensitive non-enzymatic glucose sensor based on three-dimensional network of ZnO-CuO hierarchical nanocomposites by electrospinning, Sci. Rep. 4 (2014) 7382-7391. doi:10.1038/srep07382.
- [17] P.-H. Yeh, Z. Li, Z.L. Wang, Schottky-Gated Probe-Free ZnO Nanowire Biosensor, Adv. Mater. 21 (2009) 4975–4978. doi:10.1002/adma.200902172.
- [18] Y. Zhao, P. Deng, Y. Nie, P. Wang, Y. Zhang, L. Xing, et al., Biomolecule-adsorption-dependent piezoelectric output of ZnO nanowire nanogenerator and its application as self-powered active biosensor, Biosens. Bioelectron. 57 (2014) 269–275. doi:10.1016/j.bios.2014.02.022.
- [19] N.R. Alluri, B. Saravanakumar, S.J. Kim, Flexible, hybrid piezoelectric film (BaTi<sub>(1-x)</sub>Zr<sub>x</sub>O<sub>3</sub>)/PVDF nanogenerator as a self-powered fluid velocity sensor, ACS Appl. Mater. Interfaces. 7 (2015) 9831–9840. doi:10.1021/acsami.5b01760.
- [20] J. Zhou, Y. Gu, P. Fei, W. Mai, Y. Gao, R. Yang, et al., Flexible piezotronic strain sensor, Nano Lett. 8 (2008) 3035–3040. doi:10.1021/nl802367t.
- [21] R. Yu, C. Pan, Z.L. Wang, High performance of ZnO nanowire protein sensors enhanced by the piezotronic effect, Energy Environ. Sci. 6 (2013) 494-499. doi:10.1039/c2ee23718k.
- [22] H. Hayashi, T. Nakamura, T. Ebina, In-situ Raman spectroscopy of BaTiO<sub>3</sub>

- particles for tetragonal–cubic transformation, *J. Phys. Chem. Solids.* 74 (2013) 957–962. doi:10.1016/j.jpcs.2013.02.010.
- [23] Q. Kuang, C. Lao, Z.L. Wang, Z. Xie, L. Zheng, High-sensitivity humidity sensor based on a single SnO<sub>2</sub> nanowire, (2007) 6070–6071.
- [24] V.A. Henrich, P.A. Cox, *The surface science of metal oxides*, Cambridge University Press: Cambridge, 1994; p 312.
- [25] F. Rao, M. Kim, a J. Freeman, S. Tang, M. Anthony, Structural and electronic properties of transition-metal / BaTiO<sub>3</sub>(001) interfaces, *Phys. Rev. B.* 55 (1997).
- [26] H.-P. Loock, P.D. Wentzell, Detection limits of chemical sensors: Applications and misapplications, *Sensors Actuators B Chem.* 173 (2012) 157–163. doi:10.1016/j.snb.2012.06.071.
- [27] C. Wang, L. Yin, L. Zhang, R. Gao, Ti / TiO<sub>2</sub> Nanotube Array / Ni Composite Electrodes for Nonenzymatic Amperometric Glucose Sensing, *J. Phys. Chem.* 114 (2010) 4408–4413. doi:10.1021/jp912232p.
- [28] M. Guo, X. Yin, C. Zhou, Y. Xia, W. Huang, Z. Li, Electrochimica Acta Ultrasensitive nonenzymatic sensing of glucose on Ni (OH)<sub>2</sub> -coated nanoporous gold film with two pairs of electron mediators, *Electrochim. Acta.* 142 (2014) 351–358. doi:10.1016/j.electacta.2014.07.135.
- [29] Y. Wang, J. Chen, C. Zhou, L. Zhou, Y. Kong, H. Long, et al., A novel self-cleaning, non-enzymatic glucose sensor working under a very low applied potential based on a Pt nanoparticle-decorated TiO<sub>2</sub> nanotube array electrode,

- Electrochim. Acta. 115 (2014) 269–276. doi:10.1016/j.electacta.2013.09.173.
- [30] H.D. Jang, S.K. Kim, H. Chang, K.-M. Roh, J.-W. Choi, J. Huang, A glucose biosensor based on TiO<sub>2</sub>-Graphene composite., Biosens. Bioelectron. 38 (2012) 184–8. doi:10.1016/j.bios.2012.05.033.
- [31] W.-S. Kim, G.-J. Lee, J.-H. Ryu, K. Park, H.-K. Park, A flexible, nonenzymatic glucose biosensor based on Ni-coordinated, vertically aligned carbon nanotube arrays, RSC Adv. 4 (2014) 48310–48316. doi:10.1039/C4RA07615J.
- [32] X. Guo, H. Deng, H. Zhou, T. Fan, Z. Gao, Detection of glucose with a lamellar-ridge architected gold modified electrode, Sensors Actuators B Chem. 206 (2015) 721–727. doi:10.1016/j.snb.2014.09.019.
- [33] T. Kong, Y. Chen, Y. Ye, K. Zhang, Z. Wang, X. Wang, An amperometric glucose biosensor based on the immobilization of glucose oxidase on the ZnO nanotubes, Sensors Actuators B Chem. 138 (2009) 344–350. doi:10.1016/j.snb.2009.01.002.
- [34] G. Chang, H. Shu, Q. Huang, M. Oyama, K. Ji, X. Liu, et al., Synthesis of highly dispersed Pt nanoclusters anchored graphene composites and their application for non-enzymatic glucose sensing, Electrochim. Acta. 157 (2015) 149–157. doi:10.1016/j.electacta.2015.01.085.
- [35] Z. Dai, G. Shao, J. Hong, J. Bao, J. Shen, Immobilization and direct electrochemistry of glucose oxidase on a tetragonal pyramid-shaped porous ZnO nanostructure for a glucose biosensor, Biosens. Bioelectron. 24 (2009) 1286–

1291. doi:10.1016/j.bios.2008.07.047.

- [36] S.J. Bao, C.M. Li, J.F. Zang, X.Q. Cui, Y. Qiao, J. Guo, New nanostructured TiO<sub>2</sub> for direct electrochemistry and glucose sensor applications, *Adv. Funct. Mater.* 18 (2008) 591–599. doi:10.1002/adfm.200700728.
- [37] M.B. Lerner, N. Kybert, R. Mendoza, R. Villechenon, M. a. B. López, a. T.C. Johnson, Scalable, Non-Invasive Glucose Sensor Based on Boronic Acid Functionalized Carbon Nanotube Transistors, *Appl. Phys. Lett.* 1 (2013) 1–8. doi:10.1063/1.4804438.

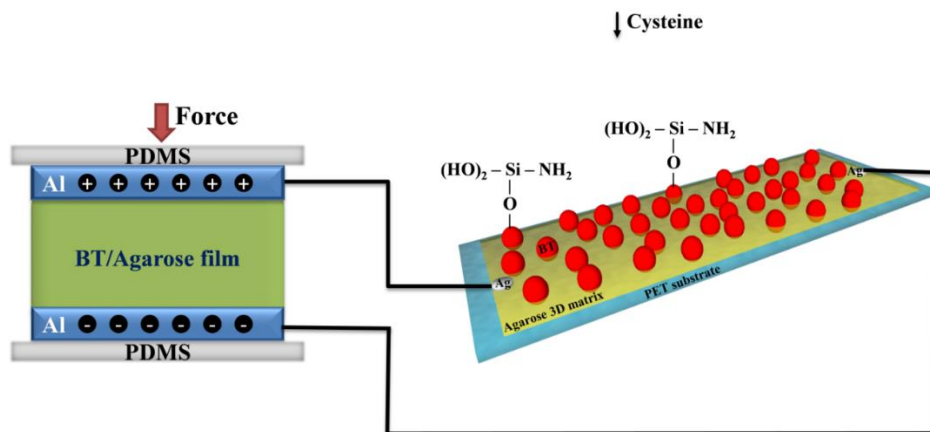
## CHAPTER IV

# Direct Detection of Cysteine Using Functionalized BaTiO<sub>3</sub> Nanoparticles Film Based Self-Powered Biosensor

### Highlights

- ✚ First report on facile and direct detection of cysteine through *I-V* technique.
- ✚ Functionalized BaTiO<sub>3</sub> NPs for self-powered cysteine biosensing system.
- ✚ Biocompatible BaTiO<sub>3</sub> NPs and agarose biopolymer paves way for green chemistry.
- ✚ Proposed sensor has good selectivity and detection limits down to 10  $\mu\text{M}$  (3 s/m).
- ✚ The findings may further lead to novel piezoelectric-biosensing devices.

### Graphical overview



#### 4.1. Introduction

Cysteine, an essential amino acid containing a thiol group, has vital roles in homeostasis and as a precursor; it has also been used as a biomarker [1]. Deviations in cysteine concentration from physiological levels (30–200  $\mu\text{M}$ ) has been linked to chronic diseases, such as rheumatoid arthritis, Parkinson's disease, Alzheimer's disease, and even adverse pregnancy outcomes [2-5]. Thus, a facile, direct method for cysteine detection could have considerable significance, given the currently available approaches, such as those based on high-performance liquid chromatography [6], colourimetric and fluorescence spectroscopy [2], capillary electrophoresis, and electrochemical voltammetry [7]. The existing methods have certain drawbacks such as complex sample preparation before measurement, time-consuming processes, and the need for sophisticated instrumentation. With this in mind, there is a continuing need for the development of a simple and rapid sensor capable of identifying cysteine in routine analysis.

One possible approach is a stimulus-responsive nanodevice; these devices have gained much attention among researchers due to their vital applications in theranostics, biomolecule detection [8], and drug delivery [9], avoiding off-target effects and false-positive results. A promising route to a stimulus-responsive system involves nanocomposites, comprising nanoparticles and polymers. Nanocomposites have been used in diverse applications in bio-sensing, electronics, drug delivery, nano-medicine, and catalysis [10] due to their enhanced functionality. Typically, the polymer plays the role of a matrix (substrate) and functionalized nanoparticles (NPs) are involved in

sensing the target molecule. In this study, an agarose (Ag) biopolymer was used as the substrate and amine-functionalised BaTiO<sub>3</sub> NPs (BT-NH<sub>2</sub> NPs) were used for the selective detection of cysteine for the first time. Agarose, a polysaccharide consisting of alternating residues of  $\alpha$ -1,3-linked D-galactose and R-1,4-linked 3,6-anhydro-R-L-galactopyranose, forms left-handed helices as a linear polymer. These helices aggregate into long fibres, which, in turn, associate in three dimensions to form a three-dimensional (3D) gel network [11]. Agarose has considerable chemical, thermal, and physical stability and is less likely to interact with biomolecules, making it a preferred matrix for use with protein and nucleic acids. Agarose films have higher stiffness than poly(vinylidene fluoride) films due to inter- and intra-hydrogen bonding of its functional groups. Also, the unique chemical functionality of agarose has prompted its use as an alternate electrode material and multifunctional green battery material [12].

The BaTiO<sub>3</sub> (BT) nanoparticles used here are a well-known metal oxide with an ABO<sub>3</sub> perovskite structure, having (n-type) semiconducting [13] and inherent piezoelectric properties [14]. Its unique features, such as biocompatibility, second-harmonic generation (SHG) [15], low dielectric constant, and high piezoelectric coefficient, make it a potential candidate for applications in biosensing [13], theranostics [16], bioimaging [17], and piezoelectric-based energy harvesting [18]. Furthermore, such ceramic perovskite-structured metal oxides have applications in electrical and electronic devices. As yet, the fact that this has still not been exploited extensively for biological applications renders great interest for self-powered biosensing and theranostic applications. Self-powered systems with novel features, such as battery-less operation,

portability, point-of-care diagnosis, and implantable applications [19], can be developed using piezoelectric nanogenerators (PNG), a relatively old energy-harvesting technology in which mechanical energy is converted into electrical energy. Self-powered nanosensors combine the nanogenerator with a sensor, through internal or external integration. Thus, the energy harvested from the nanogenerator is used to drive the sensor. Based on the novel approaches mentioned above, in the present work, a self-powered cysteine sensor was demonstrated by externally integrating a cysteine sensor with a PNG. Ag/BT-NH<sub>2</sub> film-based cysteine sensor with metal–semiconductor–metal (MSM) configuration was connected in parallel to a BT/Ag film-based piezoelectric nanogenerator (BT/Ag PNG). The cysteine sensor's analytical outputs were analysed using a current–voltage (*I–V*) technique. In a self-powered cysteine sensor, the voltage across the sensor decreases with an increase in the cysteine concentration; this potential drop is measured as the sensing signal, in accordance with *I–V* studies. To our knowledge, this is the first report of a self-powered cysteine sensor based on a direct detection technique and BT NPs. The as-fabricated sensor demonstrated comparable or enhanced performance, compared with conventional sensors. The novelty in our work stems from the direct, self-powered detection method using functionalized BT NPs, harnessing both its semiconducting and piezoelectric properties. The proposed sensor can be developed as a possible prototype for implantable and point-of-care diagnostic devices in the near future.

## **4.2. Experimental section**

### **4.2.1. Synthesis of BT NPs**

Pristine, tetragonal-phase BT NPs were synthesised via a conventional solid-state reaction method. The high-purity precursors BaCO<sub>3</sub> (99.95%, High Purity Chemicals) and TiO<sub>2</sub> (98%, Daejung Chemicals) were taken according to the atomic ratio of BaTiO<sub>3</sub> and mixed well using a pestle and mortar in acetone for 30 min until a homogeneous powder was obtained. It was then placed inside a alumina combustion boat and heated to 1200°C for 2 h in an open-tube furnace at a heating rate of 2.5°C/min [13]. The final product was taken out of the furnace after the reaction was complete and cooled naturally. The as-synthesised NPs' phase and surface morphology were confirmed by Raman spectroscopy, X-ray diffraction (XRD), and field-emission scanning electron microscopy (FE-SEM) analyses.

#### **4.2.2. NH<sub>2</sub> functionalization of BT NPs**

The BT NPs obtained were functionalized with NH<sub>2</sub>. A two-step process was used whereby the BT NPs were first functionalized with OH groups and then with NH<sub>2</sub> groups via (3-aminopropyl) triethoxysilane (APTES) treatment [16-17]. First, 120 mg of BT NPs were treated with 1M nitric acid for 2 h and then washed until neutral pH was attained. They were further treated with H<sub>2</sub>O<sub>2</sub> overnight and centrifuged (5000 rpm, 5 min). To the hydroxylated BT (BT-OH) NP product, 140 μL of APTES, 250 μL ammonium solution, and 36 mL of anhydrous ethanol were added and treated at 70°C for 8 h. After cooling, the sample was washed three times with ethanol to remove unwanted reactants. The resulting BT-NH<sub>2</sub> nanoparticles were dried and stored in a

vacuum environment.  $\text{NH}_2$  functionalization of the BT surface reduced aggregation of the NPs, resulting in a more dispersed solution [20].

#### 4.2.3. Fabrication of the cysteine sensor

A schematic diagram of the Ag/BT- $\text{NH}_2$  film-based cysteine sensor is provided in Fig. 4.1. The fabrication protocol is facile and straightforward, requiring no sophisticated equipment or process. The film was fabricated through a simple solution-casting technique. Specifically 0.2% (w/v) of BT- $\text{NH}_2$  NPs were dispersed in 1% predissolved agarose (Ag was dissolved in twice-distilled water in a microwave oven for 1 min) and allowed to gel *in situ* after casting the composite solution in Petri dishes. The film was then dried at 45°C for 24 h and later sliced according to the device dimensions (0.5 × 1 cm). Polyethylene terephthalate was used as the substrate on to which the film was attached. Electrical contacts were established using silver paste, and external connections were made using copper wires. An epoxy layer was used to cover the electrodes to prevent possible contact between the electrodes and buffer solution.

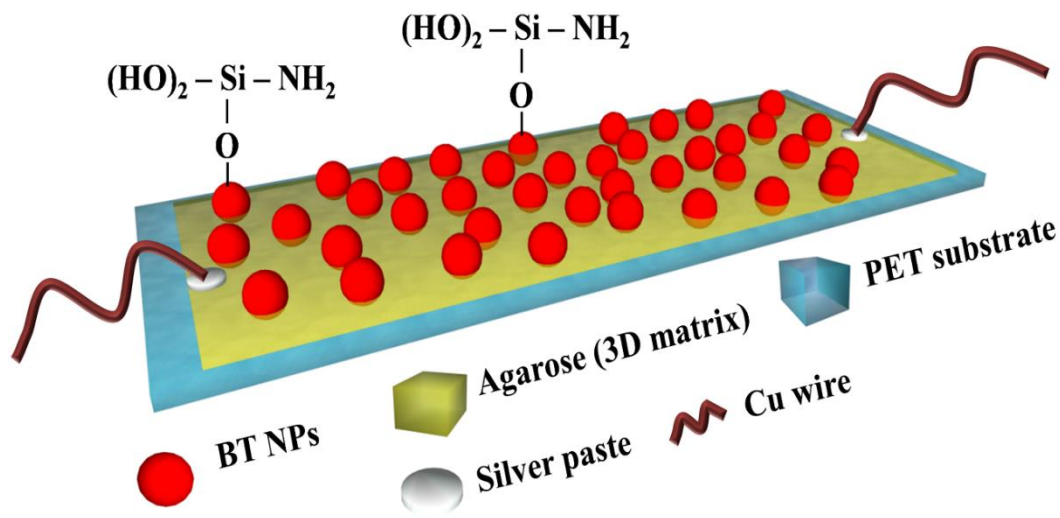


**Figure 4.1.** Schematic illustration of the as-fabricated cysteine sensor.

#### 4.2.4. Fabrication of the BT/Ag PNG

Fabrication of the BT/Ag PNG involved three simple steps: composite film formation, establishment of electrodes and external connections, and finally device packaging, as shown in Fig. 4.2. The BT/Ag film was formed by a simple solution-casting technique as described for the fabrication of the sensor. Specifically 0.1, 0.2, and 0.4 % (w/v) BT NPs in 1% Ag were used for composite film fabrication and 1% Ag for pure Ag film fabrication. To the as-fabricated composite film (3 × 3 cm), Al foil-based electrodes were attached on the top and bottom; electrical contacts were made using silver paste. External connections were established using copper wires. The device was finally packed with a polydimethylsiloxane stamp to protect it from external factors, such as humidity and temperature.

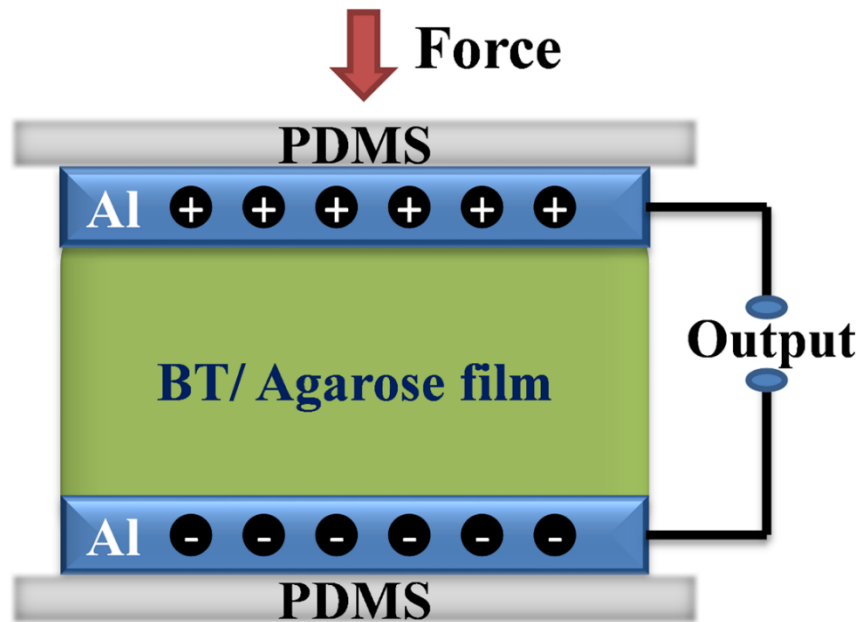


**Figure 4.2.** Schematic illustration of the as-fabricated BaTiO<sub>3</sub>/agarose (BT/Ag) nanogenerator.

#### 4.2.5. Instrumentation

An X-ray diffractometer (XRD, Rigaku), operating at 40 kV/10 mA using Cu K $\alpha$  radiation ( $2\theta$  range, 20–80°) at room temperature, was used to confirm the crystalline phase formation in the BT NPs and composite films. Raman spectra for all samples were recorded from 100 to 3000 cm<sup>-1</sup> with an excitation source of 514 nm, using a high-throughput, single-stage spectrometer (Lab RAM HR Evaluation, Japan). The surface morphology of all samples was characterised using FE-SEM (JEOL, JSM-6700F). A Prizmatiz multi-wavelength light-emitting diode (LED) light source was used as the ultraviolet (UV) source (365 nm). *I*-*V* measurements were made using a Frequency Variable CV-IV System (B 1500A). The open circuit voltage ( $V_{oc}$ ) and short circuit

current ( $I_{sc}$ ) of the PNG were recorded with a nanovoltmeter (Keithley 2182A) and a picoammeter (Keithley 6485), respectively. The PNG output was measured by triggering with a mechanical load of 2 N.

### 4.3. Results and Discussion

#### 4.3.1. Structural characterisation

The successful  $\text{NH}_2$  functionalization of BT NPs using APTES (a silane coupling agent) was confirmed through Fourier-transform infrared (FTIR) analysis. The corresponding FTIR spectra of BT NPs before and after surface modification are shown in Fig. 4.3A. The BT NP's characteristic Ti-O stretch can be observed at  $550\text{ cm}^{-1}$ . Prior to amine functionalization, BT NPs were hydroxylated, which was confirmed by  $-\text{OH}$  stretching and vibrational modes at  $3450\text{ cm}^{-1}$  and  $1650\text{ cm}^{-1}$ . The peak around  $1430\text{ cm}^{-1}$ , indicating the adsorbed carbonate group, was eliminated after surface hydroxylation. The Si- $\text{CH}_3$  stretch at around  $800\text{ cm}^{-1}$  and the double overlapping peak between  $1000$  and  $1200\text{ cm}^{-1}$  corresponding to the Si-O-Si bond, indicates appropriate silane coating of the BT NPs [17]. Primary amine bending at  $1550\text{ cm}^{-1}$  and the alkane group stretching vibrational mode at  $2960\text{ cm}^{-1}$  further confirmed the successful surface modification of BT NPs using APTES [21].

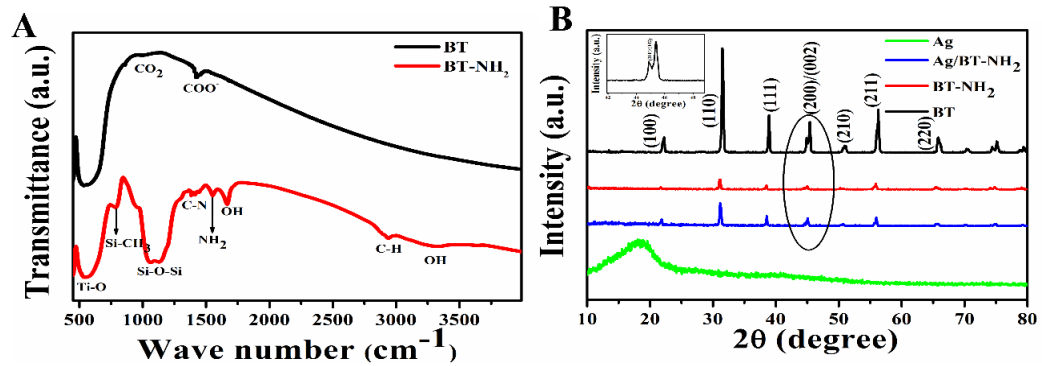


**Figure 4.3.** (A) Fourier-transform infrared spectra of BT nanoparticles (NPs) before and after NH<sub>2</sub> functionalization and (B) X-ray diffraction spectra for pristine BT NPs, BT-NH<sub>2</sub> NPs, Ag/BT-NH<sub>2</sub> film, and pristine Ag.

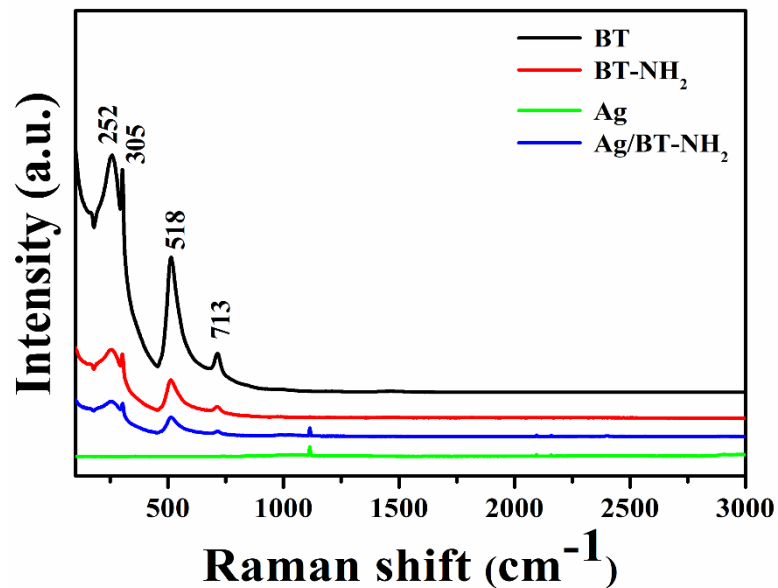


**Figure 4.4.** Raman spectra for pristine BT NPs, BT-NH<sub>2</sub> NPs, pristine Ag film and Ag/BT-NH<sub>2</sub> film.

The phases of individual components and the composites were determined using Raman and XRD characterisation. Pristine BT NPs and BT-NH<sub>2</sub> NPs have tetragonal

phases. No change in phase was observed, even after composite film formation (Ag-BT-NH<sub>2</sub>), as shown in the XRD spectrum (Fig. 4.3B). The diffraction peak splitting at 45° (200/002), observed with BT, BT-NH<sub>2</sub>, and Ag/BT-NH<sub>2</sub> film demonstrated the tetragonal nature of BT NPs, consistent with the reference ICDD 98-001-3771 pattern [18]. In the case of the agarose film, the peak at ~19° illustrates a high degree of crystallinity [22]. Moreover, the characteristic peaks at 305 cm<sup>-1</sup> and 518 cm<sup>-1</sup> in the Raman spectrum (Fig. 4.4) confirmed the tetragonality of BT NPs, indicating the presence of Ti<sup>4+</sup> ions in the parent lattice; the peaks were assigned to A1 and B1 modes, respectively [23].

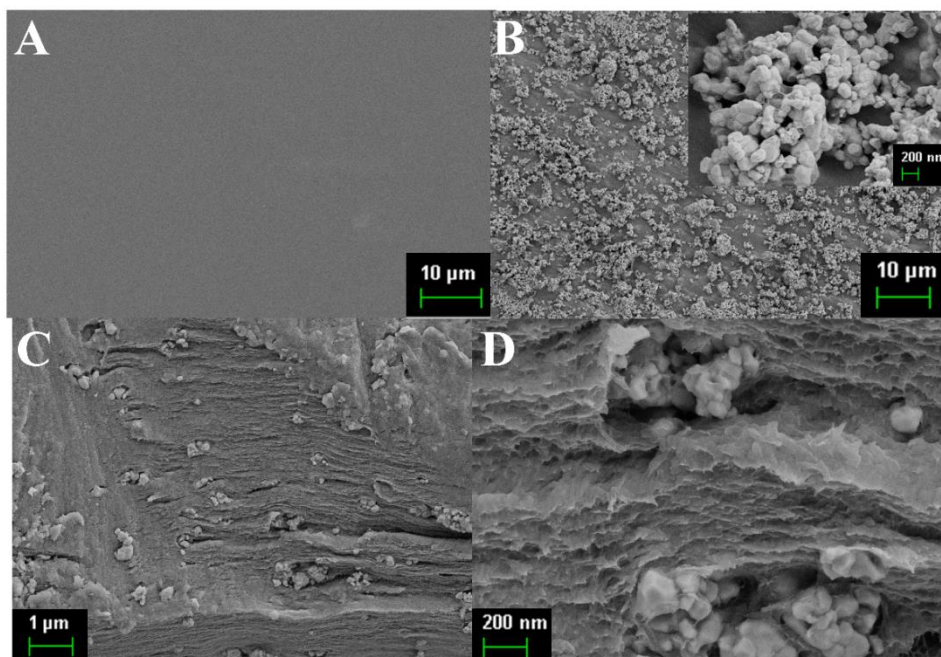


**Figure 4.5.** Scanning electron microscopy images of (A) pristine Ag film, (B) Ag/BT-NH<sub>2</sub> film (inset shows BT-NH<sub>2</sub> NPs of size  $\leq 200$  nm), Ag/BT-NH<sub>2</sub> film at (C) 1 μm scale (D) 200 nm scale.

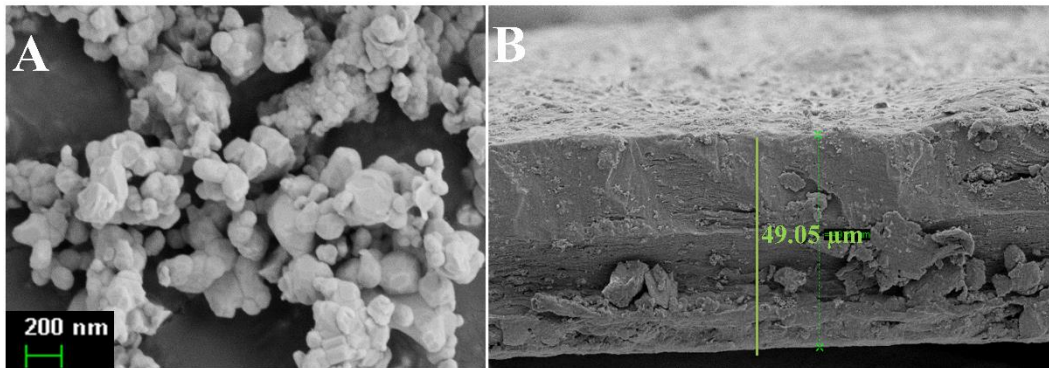


**Figure 4.6.** FE-SEM images of (A) BT NPs at 200 nm scale, (B) a cross-sectional view of Ag/BT-NH<sub>2</sub> film with a film thickness of ~50 μm.

The surface morphology of individual components and the composites were analysed through FE-SEM characterisation. The low-magnification SEM image in Fig. 4.5A shows that pure agarose film has a smooth surface in the top view. Because gelation of agarose occurred in the presence of BT-NH<sub>2</sub> NPs, the NPs are in intimate contact with the polymer matrix, being embedded within the densely packed microstructure of the agarose matrix, as confirmed by SEM images (Fig. 4.5B: the inset shows BT-NH<sub>2</sub> NPs of  $\leq 200$  nm, and Fig. 4.5 C-D). As-synthesised BT NPs have random shapes with size  $\leq 200$  nm (Fig. 4.6 A). The cross-sectional view of the Ag/BT-NH<sub>2</sub> film showed a uniform film thickness of ~50 μm (Fig. 4.6 B). Possible interactions between NPs and the agarose polymer could be mediated through hydrogen bonding or electrostatic interactions, resulting in intimate contact between them [24]. Thus, the agarose matrix served as a supporting medium (binder) for the BT-NH<sub>2</sub> NPs and connected them to the current collector (electrodes) [12].

### 4.3.2. Device characterisation and investigation of its sensing feasibility

To confirm the sensing feasibility of the Ag/BT NPs film, the surface charge properties of the film were examined with respect to pH (range: 3–7) using *I–V* technique [8].

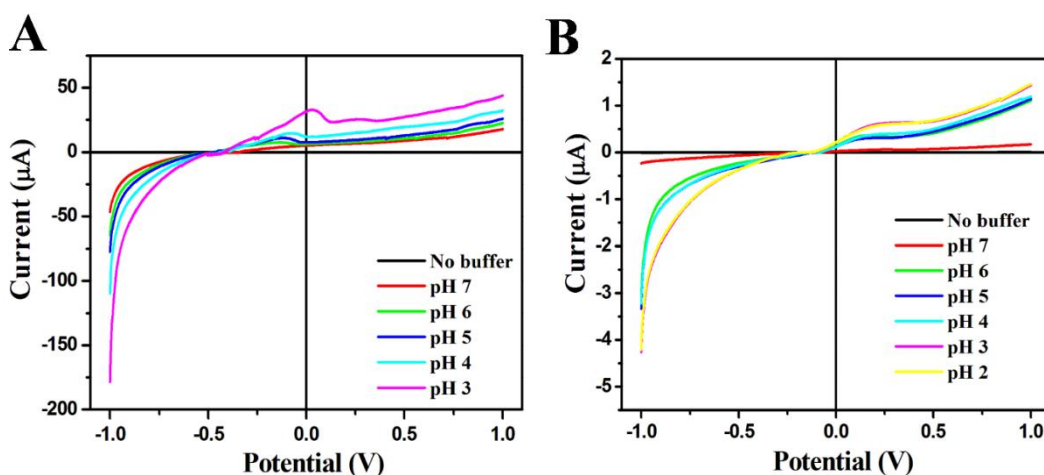


**Figure 4.7.** I-V curves of (A) Ag/BT film based device and (B) Ag film based device under different pH values (pH 7 to 3) at a bias voltage of  $\pm 1$  V.

Figure 4.7A shows that for the Ag/BT NP film-based device, the change in pH from 7 to 3 resulted in an increase in current at  $-1$  V from  $-50$   $\mu$ A to  $-175$   $\mu$ A, respectively. In contrast, for the Ag film alone (Figure 4.7B), the increase in current was negligible ( $-0.5$   $\mu$ A to  $-4.5$   $\mu$ A) at  $-1$  V. This confirmed that the agarose served as a matrix for the suspended BT NPs and that it does not make a significant contribution to sensing.

We also investigated the effect of BT-NH<sub>2</sub> NP concentration and UV light exposure in cysteine detection. To confirm whether UV light could catalyse the reaction,

the Ag/BT-NH<sub>2</sub> film-based sensor was irradiated with a UV source (365 nm) after the addition of cysteine at different concentrations (Figure 4.8A). As a control, the experiment was carried out under the same conditions with no UV irradiation (Figure 4.8B).

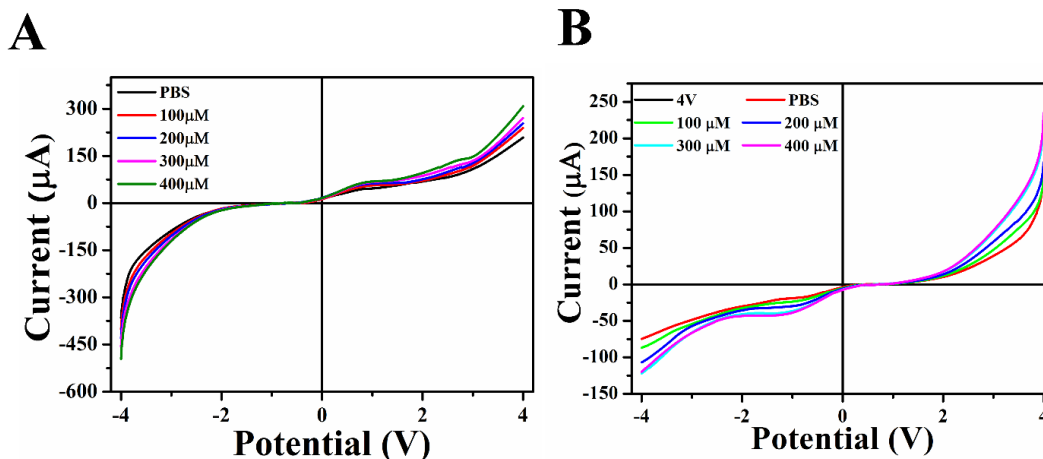


**Figure 4.8.** I-V curves of Ag/BT-NH<sub>2</sub> film based cysteine sensor under different cysteine concentrations (100 µM to 400 µM) in (A) presence and (B) absence of UV at ± 4V.

UV irradiation catalysed the reaction and enhanced the output, showing more than a two-fold increase (relative current at -4 V;  $I-I_0/I_0$ ) versus the control (Figure 4.9A). Thus, the 365-nm UV source was used in subsequent experiments.

The effect of BT-NH<sub>2</sub> NP concentration in cysteine detection was studied by comparing two concentrations of BT-NH<sub>2</sub> NPs (0.1 and 0.2% w/v). The output current increased (relative current at -4 V) with BT-NH<sub>2</sub> NP concentration, as shown in the 3D

graph in Figure 4.9B. From this, 0.2% w/v of BT-NH<sub>2</sub> NPs was taken to be the optimum concentration, as the output current obtained was sufficient for cysteine detection.

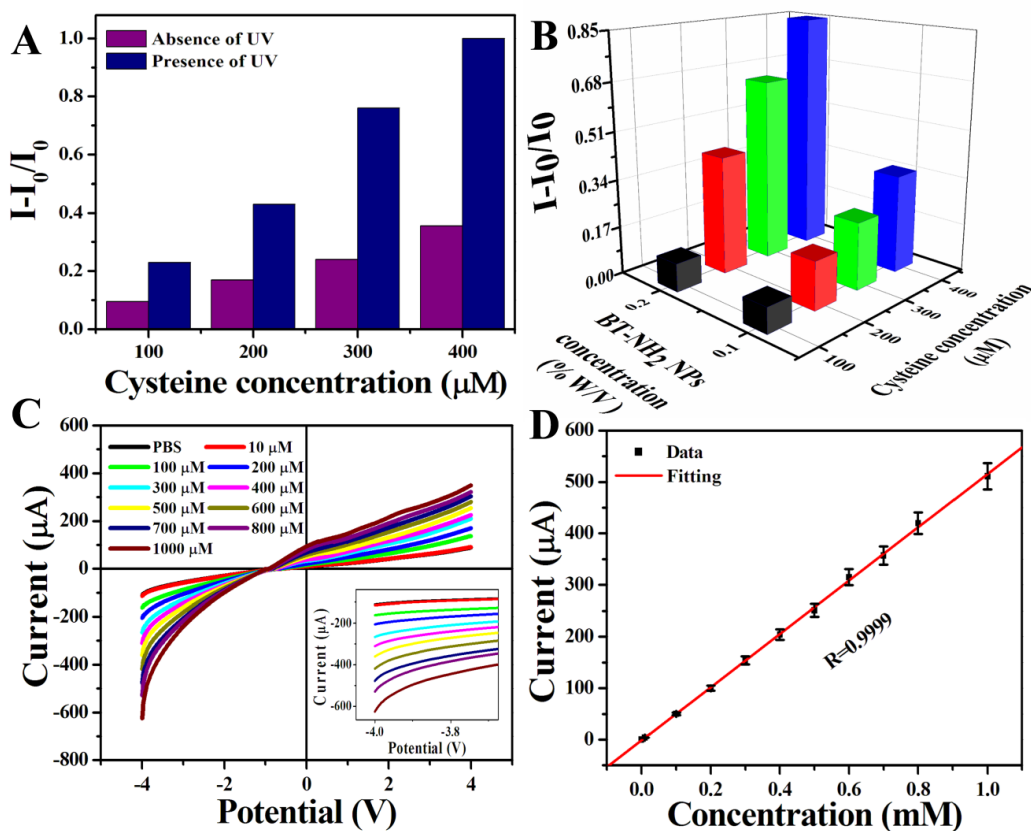


**Figure 4.9.** Cysteine detection using a current–voltage ( $I$ – $V$ ) technique. (A) Two-dimensional (2D) graph depicting the performance of a cysteine sensor in the absence and presence of ultraviolet (UV) light (365 nm). (B) Three-dimensional (3D) graphical representation of the cysteine sensor’s relative change in current ( $I-I_0/I_0$ ) with respect to BT-NH<sub>2</sub> NP and cysteine concentrations. (C)  $I$ – $V$  curves of Ag/BT-NH<sub>2</sub> film-based cysteine sensor (0.2% w/v) in response to various cysteine concentrations (10–1000

$\mu\text{M}$ ). (D) Normalized current value ( $|I-I_0|$ ) of the sensor at  $-4\text{ V}$  for different cysteine concentrations ( $10\text{--}1000\ \mu\text{M}$ ; calibration plot obtained from  $I\text{--}V$  curves).

#### 4.3.3. Cysteine detection by an $I\text{--}V$ technique

The cysteine response of the  $\text{Ag}/\text{BT-NH}_2$  film-based sensor was determined using an  $I\text{--}V$  technique.  $I\text{--}V$  curves were measured over a potential range of  $-4$  to  $+4\text{ V}$  in phosphate buffer solution ( $0.1\text{ M}$  PBS;  $\text{pH } 7$ ) containing various cysteine concentrations ( $10\ \mu\text{M}$  to  $1\text{ mM}$ ), as shown in Figure 4.9C. The inset of the figure shows an enlarged portion at  $-4\text{ V}$ . The device current output was normalised (saturated) with PBS before taking measurements with different concentrations of cysteine. After the  $\text{Ag}/\text{BT-NH}_2$  film-based sensor was exposed to UV light ( $365\text{ nm}$ ) for  $15\text{ min}$  in the presence of  $10\ \mu\text{M}$  cysteine, there was an increase in the current output at  $-4\text{ V}$ . Furthermore, with an increase in cysteine concentrations ( $10\ \mu\text{M}$  to  $1\text{ mM}$ ), the current at  $-4\text{ V}$  increased. This increase in current showed a linear relationship with cysteine concentrations (correlation coefficient:  $0.9999$ ), as in the calibration curve (Figure 4.9D). The limit of detection (LOD) was  $\sim 10\ \mu\text{M}$ ; LOD was calculated from the calibration curve by the “ $3s/m$ ” criteria, where  $s$  is the standard deviation and  $m$  is the slope of the calibration curve. With physiological levels of cysteine of the order of  $30\text{--}200\ \mu\text{M}$  [1], the as-fabricated sensor with a sensitivity of  $\sim 506\ \mu\text{A}/\text{mM}$  should be sufficient for practical, routine analysis. As a control, the experiment was also performed using only PBS to ensure that the current signal obtained was due to cysteine and was not from ions present in the PBS (electrolyte), as shown in Figure 4.10 A-B. From

Figure 4.10 C, it can be seen that with an increase in the PBS concentration, there was no significant increase in current output at  $-4$  V, compared with the current change ratio in the presence of cysteine (100 to 400  $\mu$ M). The Ag/BT-NH<sub>2</sub> film has a positive surface charge in the absence of cysteine under the given experimental conditions. A rapid increase in current occurred at  $-4$  V upon addition of cysteine, as expected from the pI of cysteine (5.07), because it would be negatively charged at the given pH of our experimental conditions, leading to the binding of negatively charged species to the film and the depletion of positively charged species [8]. With an increase in cysteine concentration, the negative charge on the film surface increased, resulting in a significant increase in current at  $-4$  V.

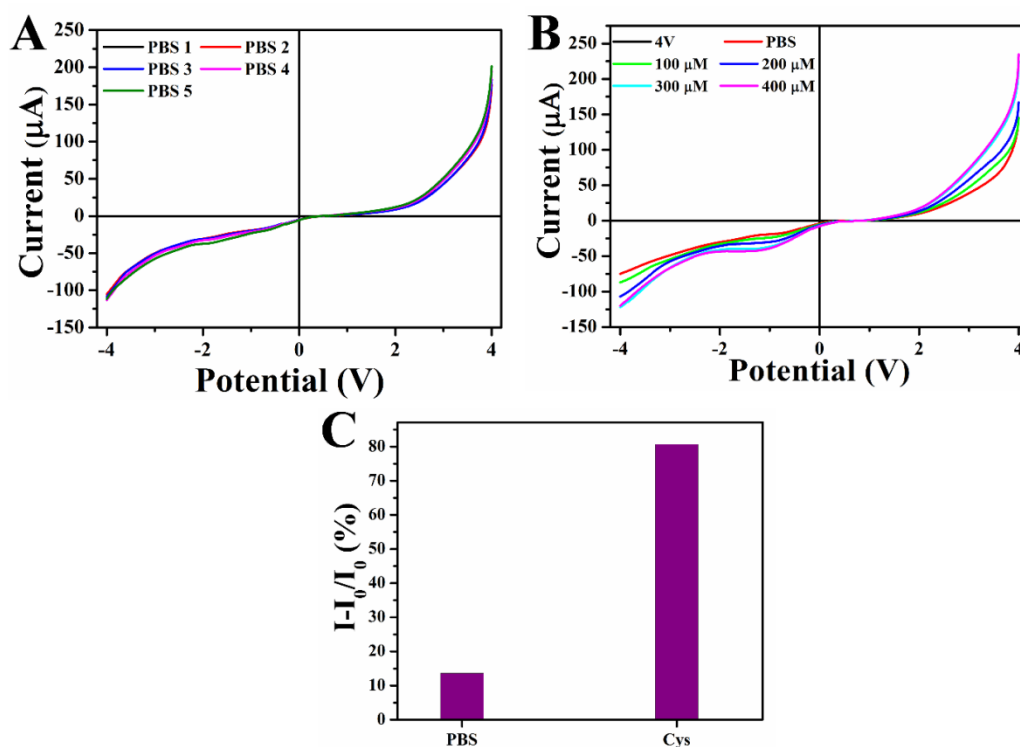


**Figure 4.10.** I-V curves of Ag/BT-NH<sub>2</sub> film based cysteine sensor in presence of

different concentrations of (A) PBS buffer and (B) cysteine (100  $\mu\text{m}$  to 400  $\mu\text{m}$ ) (C) Comparison between their relative change in current (%) at -4V.

#### 4.3.4. Proposed working mechanism of the Ag/BT-NH<sub>2</sub> film-based cysteine sensor

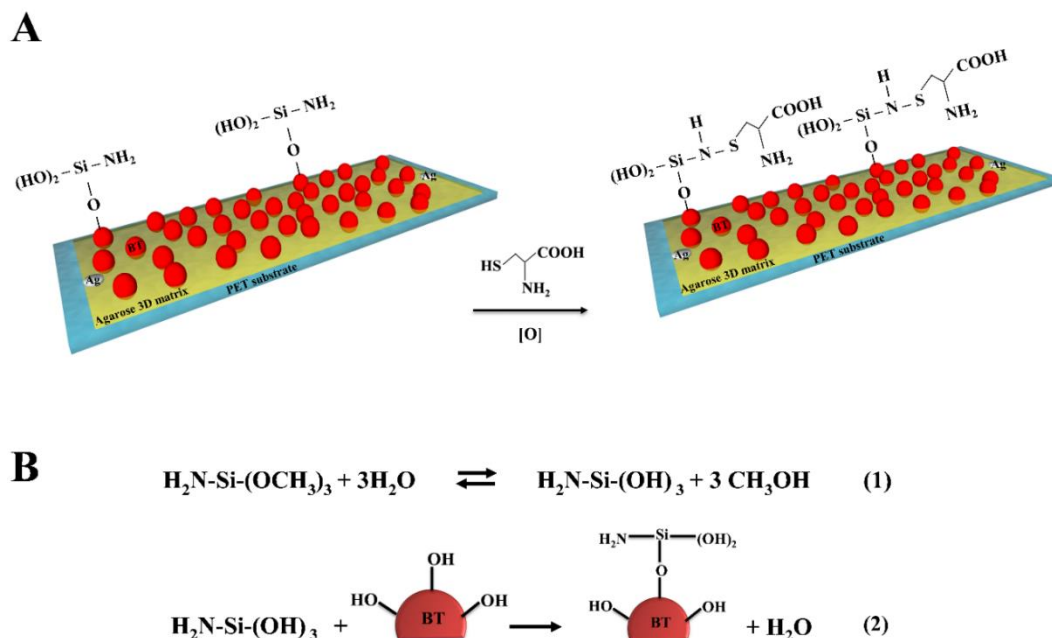
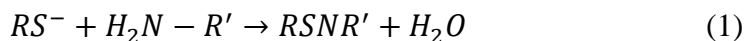


**Figure 4.11.** Schematic representation. (A) Proposed mechanism of cysteine detection (B) Reaction scheme for amine functionalization of BT NPs using (3-aminopropyl) triethoxysilane (APTES, a silane coupling agent).

An increase in negatively charged species (cysteine) on the film will increase the charge carrier density (electrons) and thus eventually decrease the resistance across the film, leading to an increased output current [13]. This typical MSM device behaviour was observed in the  $I$ - $V$  data [13], [19]. In absence of buffer or cysteine, Ohmic

behaviour was observed ; with the introduction of different concentrations of cysteine, the  $I-V$  curves became non-linear. The increase in charge carrier density (electrons) in the film lowers the Schottky barrier height on the drain side (M-S interface), resulting in a significant increase in the output current of the Ag/BT-NH<sub>2</sub> film-based sensor.

A possible response mechanism can be explained as follows. R-SH (thiol) in the presence of BT-NH<sub>2</sub> (positive residue) loses a H<sup>+</sup> ion and becomes a thiolate [25]. The thiolate side chain (R-S<sup>-</sup>) in cysteine is a strong nucleophile [1] and acts as a Lewis base, ready to react with the NH<sub>2</sub> group on BT NPs (electrophiles). This results in a nucleophilic attack of R-S<sup>-</sup> on the NH<sub>2</sub> group, leading to S-N bond formation (sulfenamides; (Figure 4.11 A); equation (1)) [26]. Thus, cysteine binds to the film, increasing its surface negative charge. A detailed reaction scheme for the functionalization of BT NPs with amine groups is provided in (Figure 4.11 B). The proposed sensor's analytical throughput (LOD and linear concentration range) is better than or comparable to existing cysteine sensors (Table 1). These reported sensors are based on colourimetric, amperometric, and fluorescence-based techniques, whereas the sensor developed is self-powered and based on a direct detection technique. Thus, our novel sensor design provides efficient cysteine detection with minimal sample processing and time consumption; as such, being a prototype for implantable and point-of-care diagnostic devices.



#### 4.3.5. Real-time analysis and interference studies

The sensor was further assessed with complex matrices like urine samples for real-time detection. Non-invasive detection using urine samples has great advantages, such as patient compliance and ease of sample handling. An abnormal level of cysteine in urine is a result of a disorder or disease [8]. The physiological level of cysteine in urine mirrors changes in plasma, where the level varies from 30 to 200  $\mu\text{M}$  [28-29]. Thus, for real sample analyses, the concentration range studied was 10–500  $\mu\text{M}$ , which covers the physiological range of cysteine. The urine samples collected were diluted by a factor of 10 with 0.1 M PBS (pH 7) and immediately used for analysis. The diluted samples were spiked with known concentrations of cysteine (10-500  $\mu\text{M}$ ).  $I$ - $V$  curves of the Ag/BT-NH<sub>2</sub> film-based cysteine sensor in response to different concentrations of cysteine-spiked urine samples are shown in Figure 4.12 A (inset shows the enlarged portion at  $-4$  V). The  $I$ - $V$  characteristics obtained were consistent with the cysteine concentrations (10  $\mu\text{M}$  to 1 mM) shown in Figure 4.9 C. From the calibration plot obtained (Figure 4.12 B), there was a linear relationship between the current obtained at  $-4$  V and the cysteine concentration (correlation coefficient: 0.9999) and LOD obtained was  $\sim 10$   $\mu\text{M}$  (3s/m criteria) which is in agreement with Figure 4.9 D. Thus the sensor is applicable for screening samples to check whether the cysteine level lies within the normal physiological range or not.

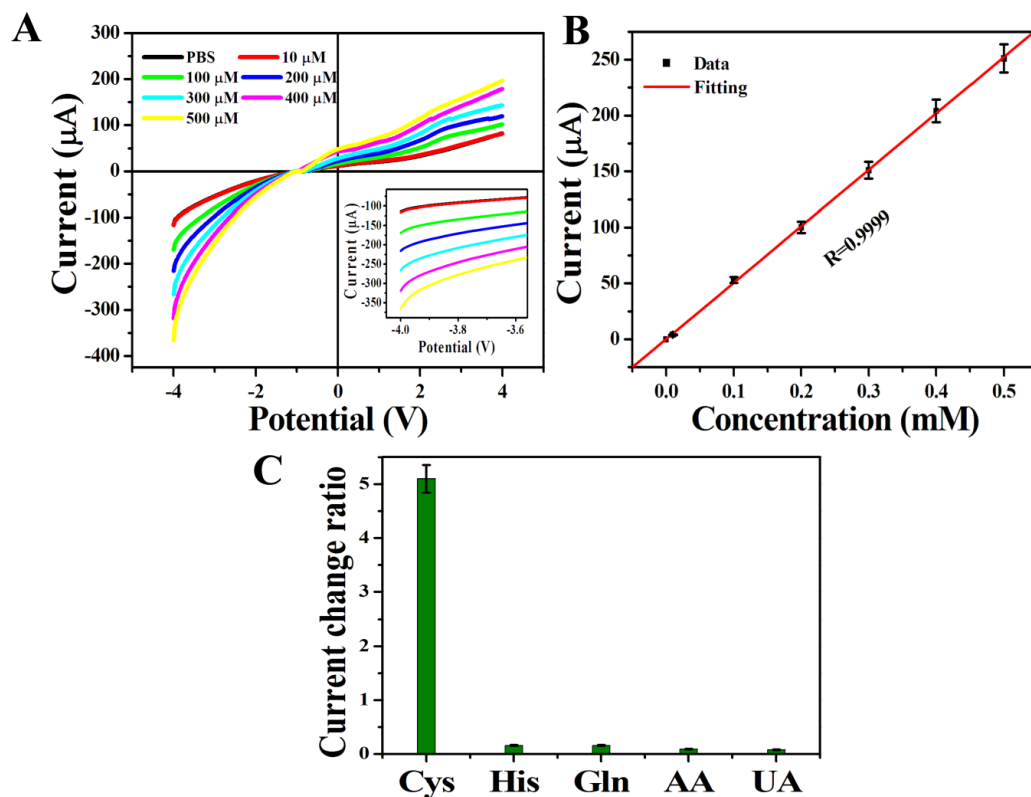


**Figure 4.12.** Real sample analysis and interference studies. (A)  $I$ - $V$  response of the Ag/BT-NH<sub>2</sub> film-based cysteine sensor in the presence of a urine sample spiked with different cysteine concentrations (10–500  $\mu\text{M}$ ). (B) Normalized current value ( $|I-I_0|$ ) of the sensor at  $-4$  V in the presence of different concentrations of cysteine-spiked urine sample (10–500  $\mu\text{M}$ ; calibration plot obtained from  $I$ - $V$  curves). (C) Current change ratio of cysteine sensor measured at  $-4$  V in 0.1 M PBS (pH 7) with the addition of 1 mM Cys, His, Gln, AA, and UA.

The sensor has good selectivity towards cysteine compared to various interfering species, such as histidine (His), glutamine (Gln), ascorbic acid (AA), and uric acid (UA). The current change ratios measured at  $-4$  V in  $0.1$  M PBS (pH 7) with the addition of  $1$  mM Cys, His, Gln, AA, and UA are shown in Figure 4.12 C. From the negligible current change ratios for interfering species compared with that of cysteine, the sensor's selectivity towards cysteine is clear.

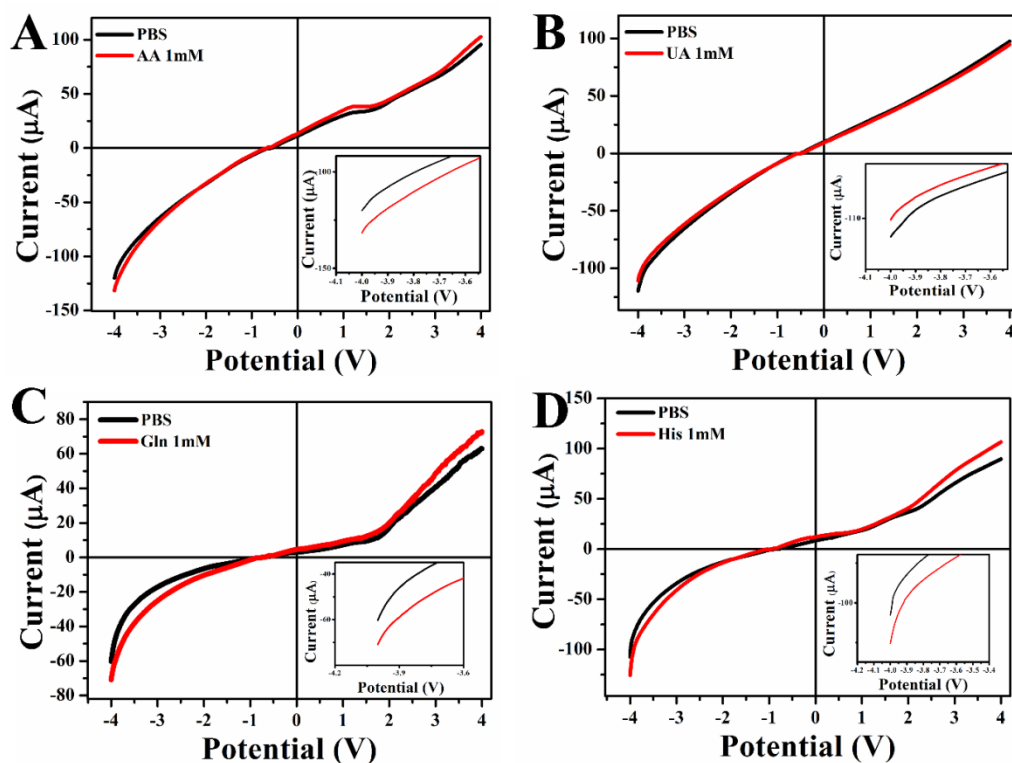


**Figure 4.13.** Interference study. I-V curves of Ag/BT-NH<sub>2</sub> film based cysteine sensor at  $\pm 4$  V in presence of 1 mM concentration of interferents namely (A) AA, (B) UA, (C) Gln and (D) His (inset shows the enlarged view of the I-V curve at -4 V).

The  $I$ - $V$  curves of a Ag/BT-NH<sub>2</sub> film-based sensor in response to 1 mM concentrations of potentially interfering species in the presence of PBS (electrolyte) are shown in Figure 4.12 A–D (the inset shows an enlarged portion at  $-4$  V). There were negligible changes in current at  $-4$  V, even at 1 mM concentrations of the interfering species.

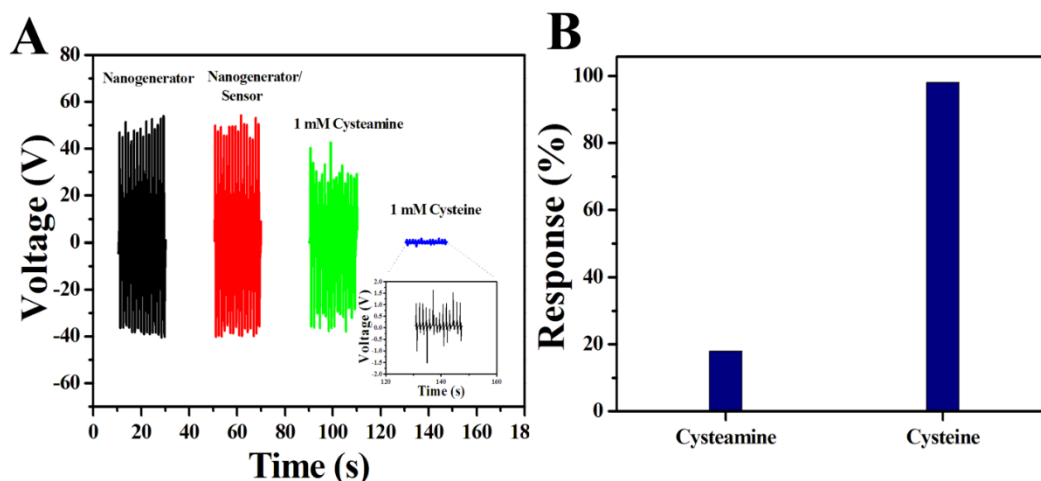


**Figure 4.14.** Interference study for self-powered cysteine sensor. (A) The open circuit potential drop across the sensor in the presence of 1 mM cysteamine and 1 mM cysteine (@2N load; inset shows the enlarged view of the open circuit potential drop for 1 mM cysteine). (B) The response of the self-powered cysteine sensor to 1 mM concentration of cysteamine and cysteine respectively.

Additionally, interference study for self-powered cysteine sensor was also performed using cysteamine; an aminothiols and a therapeutic drug used for treating cysteine related disorders (Figure 4.14 A–B). The open circuit potential drop across the sensor (peak-to-peak value) for 1 mM cysteamine is 65 V and to that of 1 mM cysteine

is 1.5 V. Thus, the response of the sensor to cysteamine and cysteine is 18% and 98% respectively (~ 5.5 fold difference) as shown in Figure 4.14 B; once again confirms the sensor's selectivity. The experiments were repeated four times (denoted by error bars) and measurements were made over a time period of two months (stored at room temperature) which proves the sensors performance, reproducibility and stability.

#### 4.3.6. BT/Ag PNG

The novel approach to cysteine detection demonstrated prompted development of a self-powered sensor system. Agarose, a biopolymer, has been recently exploited in energy harvesting and storage devices, due to its unique chemical features (ether and hydroxyl groups) and properties, such as higher stiffness (due to inter- and intra-hydrogen bonding of its functional groups), as an electrode binder, multifunctional green battery material, and building element for battery separators [12]. A composite made of agarose and BT can be exploited to create a piezoelectric nanogenerator for energy harvesting, which can then be used as a power source for driving the Ag/BT-NH<sub>2</sub> film-based sensor. The biopolymer agarose serves as a matrix for the BT NPs, assisting in film formation. BT/Ag PNGs of four different weight ratios (0, 0.1, 0.2, and 0.4% w/v), with 3 × 3 cm dimensions, were fabricated as described in the Experimental section. The  $V_{oc}$  and  $I_{sc}$  of these PNGs are shown in Figure 4.15 A-B and Figure 4.16 A. The 0.4% w/v BT/Ag PNG showed the best performance among the various weight ratios, with an average peak-to-peak  $V_{oc}$  of 80 V (Figure 4.16 B) and an average peak-to-peak  $I_{sc}$  of 285 nA (Figure 4.16 C) at a mechanical load of 2 N, the maximum values among the four

weight ratios. With an increase in BT concentration, the nanogenerator's output voltage and current increased (Figure 4.16 A). The composite film with a higher % w/v of BT NPs showed higher performance compared with the pure Ag film and lower % w/v BT NPs. The piezoelectric potential generated from this device (0.4% w/v) can light up six commercial green LEDs (Figure 4.16 D), confirming its ability to power sensors and other low-power electronic gadgets. The as-fabricated PNG showed good stability, giving a stable output voltage of 80 V with no degradation, even for a period of 1000 s under a mechanical force of 2 N (Figure 4.16 E). Thus, this PNG was used as the power source to drive the as-fabricated cysteine sensor.

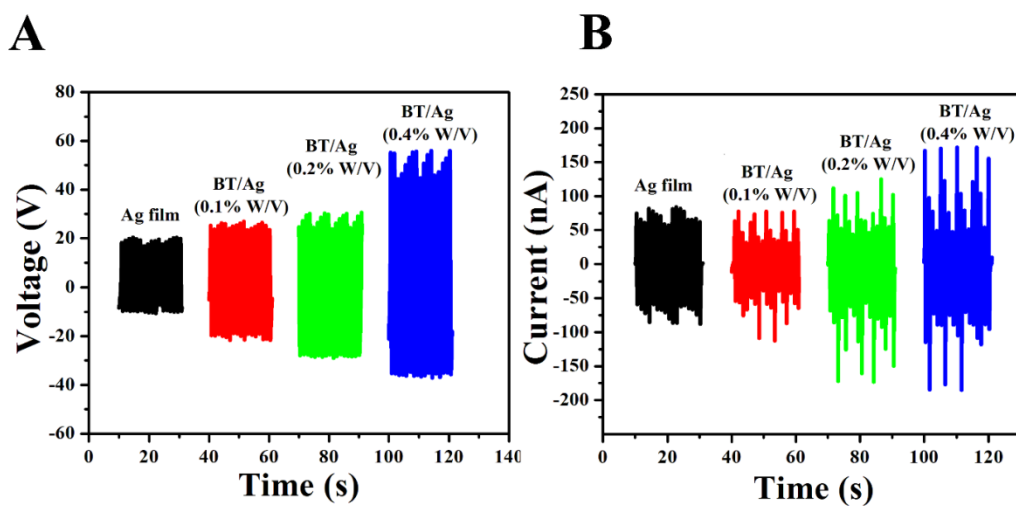


**Figure 4.15.** (A) Open circuit voltage ( $V_{oc}$ ) and (B) short circuit current ( $I_{sc}$ ) of 0, 0.1, 0.2 and 0.4 % (W/V) of BT/Ag NG at a mechanical load of 2N.

#### 4.3.7. Working mechanism of PNG

The flexible PNG's mechanical energy is converted into electrical energy. When a compressive force is applied, orientation of dielectric poles in the BT/Ag composite

film occurs, generating a piezoelectric potential. The perpendicular force acting on the composite film generates a piezopotential on both sides of the film, which, in turn, induces inductive charges on the top and bottom electrodes. The charge carriers create a potential difference, which drives electrons through the external circuitry [30].

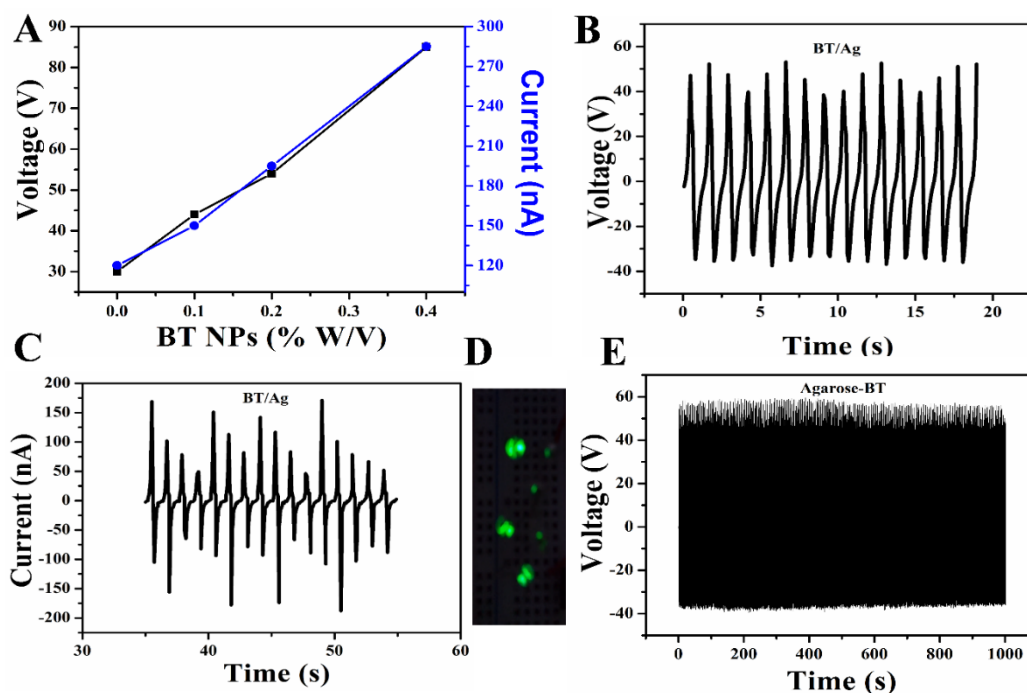


**Figure 4.16.** Self-powered cysteine sensor. (A) Output voltage and current of BT/Ag nanogenerator as a function of different concentrations of BT NPs (% w/v) at a mechanical load of 2 N. (B) Open circuit voltage ( $V_{oc}$ ) and (C) short-circuit current ( $I_{sc}$ ) of BT/Ag nanogenerator (0.4% w/v) at 2 N. (D) Demonstration of commercial green light-emitting diodes (LEDs) lit using the piezoelectric potential generated. (E) Stable output voltage of the nanogenerator (under a load of 2 N) for a period of 1000 s with no degradation.

**Table 4.1.** Comparison between cysteine sensors based on different detection techniques

Material employed	Detection technique	Limit of detection	Linear range concentration	Reference
Fluorescent AgAuNCs@11-MUA	Fluorometric	111 Nm	0.25-7 $\mu$ M	[31]
GCE/MWCNTs/PEI/Au NPs electrode modified with DTNB	Amperometric	2.7 $\mu$ M	9.0-250 $\mu$ M	[32]
Coumarin derivative	Fluorometric	L <sup>-1</sup>	L <sup>-1</sup>	[33]
Silver nanoparticles	Colourimetric	100 nM	0-0.9 mM	[34]
MIL-88A-derived Fe <sub>3</sub> O <sub>4</sub> -carbon Hierarchical nanocomposites	Amperometric	2 $\mu$ M	0.007-14.18 mM	[35]
Tetraphenylethene-coumarin hybrid fluorophore	Fluorometric	5 $\mu$ M	5-500 $\mu$ M	[36]
NH <sub>2</sub> -functionalised BT NPs suspended in agarose matrix	I-V technique	10 $\mu$ M	10 $\mu$ M-1 mM	<b>This work</b>
Tris(bipyridine)Ru(II) complex	Fluorometric	1.41 $\mu$ M	15 to 180 $\mu$ M	[37]

In the case of a nanogenerator made of pure agarose film, the generation of electrical output is mainly from the functional groups (hydroxyl and ether) present in the agarose, causing inductive charges on the top and bottom Al electrodes. The difference in potential between the two electrodes drives the charge carriers through the external connections, leading to the generation of an electrical output. A PNG made from BT/Ag composite film showed better performance and thus was used for driving the sensor.

#### 4.3.8. Integration of the cysteine sensor and BT/Ag PNG

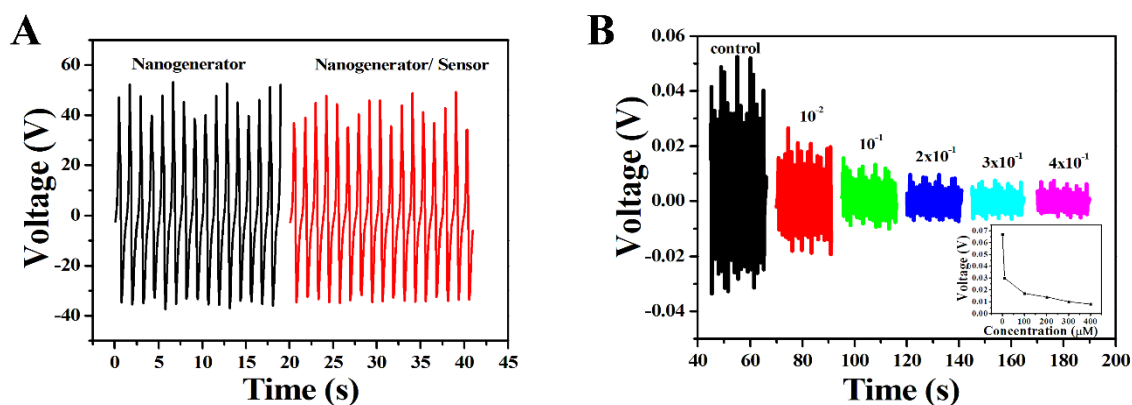


**Figure 4.17.** (A) Output voltage of the nanogenerator (NG) and self-powered cysteine sensor (NG/cysteine sensor) under a load of 2 N. (B) The open-circuit potential drop across the sensor as a function of different cysteine concentrations ( $10^{-2}$  mM to  $4 \times 10^{-1}$  mM) at 2 N (inset shows the calibration plot where the potential drop across the sensor has a monotonic functional relationship with the cysteine concentration).

The electrical output generated from the BT/Ag PNG was used to drive the Ag/BT-NH<sub>2</sub> film-based cysteine sensor. To demonstrate the self-powered device, the

cysteine sensor was connected in parallel to the BT/Ag PNG. The PNG output and PNG/cysteine sensor (self-powered device) output (peak-to-peak  $V_{oc}$ :  $\sim 80$  V @ 2 N, in the absence of buffer) was approximately the same, confirming that the sensor's resistance was equal to the PNG's resistance (1–50 M $\Omega$ ; Figure 4.17 A). With the introduction of a buffer, the voltage across the sensor decreased and approached saturation. Further addition of cysteine to the buffer caused the voltage across the sensor to decrease further. With an increase in cysteine concentrations from 10 to 400  $\mu$ M, the voltage across the sensor decreased from 30 to 8 mV, respectively under a 2-N load (Figure 4.17 B), consistent with the  $I$ – $V$  characteristics of the sensor in the presence of different cysteine concentrations (Figure 4.9 C). Typical MSM device behaviour was observed. With increased cysteine concentrations, the resistance of the device (sensor) decreased due to an increase in charge carrier density (electrons) and thus the voltage across the sensor decreased. This potential drop across the sensor showed a monotonic relationship with cysteine concentrations (inset, Figure 4.17 B). The non-linearity of the self-powered cysteine sensor was attributed to the PNG's instantaneous voltage, as there is a small time lag between the PNG's output and continuous cysteine sensor response. However, the cysteine sensor itself has a linear response (Figure 4.9 D).

#### 4.4. Conclusions

We report for the first time the facile, direct detection of cysteine using functionalized BT NPs. Amine-functionalised BT NPs suspended in an agarose matrix were used for cysteine detection based on the change in surface charge properties of the

composite film. The novel composite was also investigated for harvesting energy, leading to the development of a self-powered device. The agarose biopolymer and biocompatible BT NPs were used for sensing as well as for energy harvesting resulting in green chemistry. The as-fabricated sensor showed good selectivity, reproducibility, low cost, and detection limits down to  $\sim 10 \mu\text{M}$ . The study may further lead to the realization of functionalized BT NPs in theranostic applications and novel piezoelectric-biosensing devices.

## References

- 1 H. S. Jung, J. H. Han, T. Pradhan, S. Kim, S. W. Lee, J. L. Sessler, T. W. Kim, C. Kang and J. S. Kim, *Biomaterials*, 2012, **33**, 945–953.
- 2 H. S. Jung, T. Pradhan, J. H. Han, K. J. Heo, J. H. Lee, C. Kang and J. S. Kim, *Biomaterials*, 2012, **33**, 8495–8502.
- 3 C. Yang, X. Wang, L. Shen, W. Deng, H. Liu, S. Ge, M. Yan and X. Song, *Biosens. Bioelectron.*, 2016, **80**, 17–23.
- 4 Q. Gong, R. Zhang, J. Yang, Z. Huang, N. Li, N. Zhao and B. Z. Tang, *J. Mater. Chem. C*, 2015, **3**, 8397–8402.
- 5 M. Zhang, M. Yu, F. Li, M. Zhu, M. Li, Y. Gao, L. Li, Z. Liu, J. Zhang, D. Zhang, T. Yi and C. Huang, *J. Am. Chem. Soc.*, 2007, **129**, 10322–10323.
- 6 O. Nekrassova, N. S. Lawrence and R. G. Compton, *Talanta*, 2003, **60**, 1085–1095.
- 7 S. J. Park, H. S. Song, O. S. Kwon, J. H. Chung, S. H. Lee, J. H. An, S. R. Ahn, J.

- E. Lee, H. Yoon, T. H. Park and J. Jang, *Sci. Rep.*, 2014, **4**, 4342.
- 8 Z. Sun, C. Han, M. Song, L. Wen, D. Tian, H. Li and L. Jiang, *Adv. Mater.*, 2014, **26**, 455–460.
- 9 F. Xia, H. Ge, Y. Hou, T. Sun, L. Chen, G. Zhang and L. Jiang, *Adv. Mater.*, 2007, **19**, 2520–2524.
- 10 P. Thoniyot, M. J. Tan, A. A. Karim, D. J. Young and X. J. Loh, *Adv. Sci.*, 2015, **2**.
- 11 K. S. Horger, D. J. Estes, R. Capone and M. Mayer, 2009, 2973–2982.
- 12 G. Hwang, J.-M. Kim, D. Hong, C.-K. Kim, N.-S. Choi, S.-Y. Lee and S. Park, *Green Chem.*, 2016, 14–19.
- 13 S. Selvarajan, N. R. Alluri, A. Chandrasekhar and S.-J. Kim, *Sensors Actuators B Chem.*, 2016, **234**, 395–403.
- 14 K. Il Park, M. Lee, Y. Liu, S. Moon, G. T. Hwang, G. Zhu, J. E. Kim, S. O. Kim, D. K. Kim, Z. L. Wang and K. J. Lee, *Adv. Mater.*, 2012, **24**, 2999–3004.
- 15 C.-L. Hsieh, R. Grange, Y. Pu and D. Psaltis, *Biomaterials*, 2010, **31**, 2272–2277.
- 16 E. FarrokhTakin, G. Ciofani, G. L. Puleo, G. de Vito, C. Filippeschi, B. Mazzolai, V. Piazza and V. Mattoli, *Int. J. Nanomedicine*, 2013, **8**, 2319–31.
- 17 J. Čulić-Viskota, W. P. Dempsey, S. E. Fraser and P. Pantazis, *Nat. Protoc.*, 2012, **7**, 1618–1633.
- 18 N. R. Alluri, B. Saravanakumar and S. J. Kim, *ACS Appl. Mater. Interfaces*, 2015, **7**, 9831–9840.
- 19 R. Yu, C. Pan, J. Chen, G. Zhu and Z. L. Wang, *Adv. Funct. Mater.*, 2013, **23**, 5868–5874.

- 20 J. Culic-viskota, 2012, **2012**.
- 21 J. Coates, R. A. M. Ed and J. Coates, *Encycl. Anal. Chem.*, 2000, 10815–10837.
- 22 Y. Freile-Pelegr, T. Madera-Santana, D. Robledo, L. Veleza, P. Quintana and J. A. Azamar, *Polym. Degrad. Stab.*, 2007, **92**, 244–252.
- 23 H. Hayashi, T. Nakamura and T. Ebina, *J. Phys. Chem. Solids*, 2013, **74**, 957–962.
- 24 Z. Wang, R. Zhang, Y. Ma, L. Zheng, A. Peng, H. Fu and J. Yao, *J. Mater. Chem.*, 2010, **20**, 1107.
- 25 M. L. C. and K. S. Carroll, *Oxidative Stress Redox Regul.*, 2012.
- 26 F. Johnson, H. Levanon, J. R. Norris and F. Johnson, *Nature*, 1970, **227**, 419–419.
- 27 B. Saravanakumar, S. Soyoon and S. Kim, *ACS Appl. Mater. Interfaces*, 2014, **6**, 13716–13723.
- 28 Refsum, H., Ueland, P.M., Kvinnsland, S., 1986. *Cancer Res* 46, 5385–5391.
- 29 Kaniowska, E., Chwatko, G., Głowacki, R., Kubalczyk, P., Bald, E., 1998. *J. Chromatogr. A* 798, 27–35.
- 30 J. Zhang, X. Xu, Y. Yuan, C. Yang and X. Yang, *ACS Appl. Mater. Interfaces*, 2011, **3**, 2928–2931.
- 31 J. Zhang, J. Wang, J. Liu, L. Ning, X. Zhu, B. Yu, X. Liu, X. Yao and H. Zhang, *Anal. Chem.*, 2015, **87**, 4856–4863.
- 32 J. Lee, P. A. Ulmann, M. S. Han, C. A. Mirkin, J. Lee, P. A. Ulmann, M. S. Han and C. A. Mirkin, 2008.
- 33 M. Santhiago, P. R. Lima, W. de J. R. Santos and L. T. Kubota, *Sensors Actuators, B Chem.*, 2010, **146**, 213–220.

- 34 C. Han, K. Xu, Q. Liu, X. Liu and J. Li, *Sensors Actuators, B Chem.*, 2014, **202**, 574–582.
- 35 L. Wang, Y. Zhang, X. Li, Y. Xie, J. He, J. Yu and Y. Song, *Sci. Rep.*, 2015, **5**, 14341.
- 36 Z. Yang, N. Zhao, Y. Sun, F. Miao, Y. Liu, X. Liu, Y. Zhang, W. Ai, G. Song, X. Shen, X. Yu, J. Sun and W.-Y. Wong, *Chem. Commun.*, 2012, **48**, 3442.
- 37 X. Lou, Z. Zhao, Y. Hong, C. Dong, X. Min, Y. Zhuang, X. Xu, Y. Jia, F. Xia and B. Z. Tang, *Nanoscale*, 2014, **6**, 14691–14696.

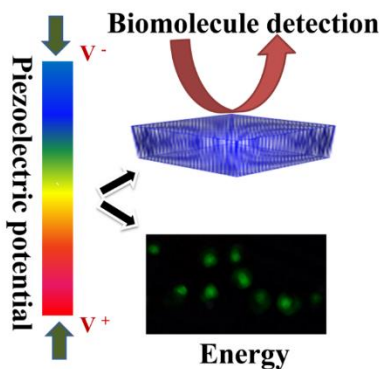
## CHAPTER V

# Unconventional Active Biosensor made of Piezoelectric BaTiO<sub>3</sub> Nanoparticles for Biomolecule Detection

### Highlights

- ✚ First report on BaTiO<sub>3</sub> NPs film based nanogenerator as one-stop active glucose sensor.
- ✚ Multifunctional and biocompatible BaTiO<sub>3</sub> NPs with piezoelectric and semiconducting properties.
- ✚ Device with dual functions, as both an energy source and a biosensing signal.
- ✚ Proposed sensor has good selectivity and detection limits down to 10  $\mu$ M.
- ✚ Prototype for smart/intelligent implantable nanosystems for theranostic applications.

### Graphical overview



## 5.1. Introduction

Multi-functional, self-powered, piezoelectric-based active sensors have potential in the development of medical devices for health-monitoring purpose. The realization of such a smart nanosystem is quite challenging, but highly desirable for next-generation diagnostic and theranostic applications. Such unconventional diagnostic tools can be realized from conventional principles existing in everyday applications, such as piezoelectricity. Piezoelectric nanogenerators (PNG) are among the older, more established energy harvesters converting mechanical energy into electrical energy [1]. Much research has been focused on harvesting mechanical energy in living environments, and scavenging biomechanical energy, and their conversion to electrical power for powering low-power electronic gadgets and sensors [2-4]. Few reports on PNGs as implantable devices for health monitoring are available [5],[6]. With limitations in the operational lifetime of the conventional batteries used for powering implantable devices, continuous monitoring over long periods is almost impossible. Surgeries are needed to replace batteries, leading to complications and morbidity. Implantation of both an energy harvester and a monitoring system could be a solution but it would occupy more space inside the recipient animal or patient, involving complex surgical procedures. Thus, developing a stand-alone, fully integrated, one-stop device (an active biosensor) is a desirable solution.

The BaTiO<sub>3</sub> nanoparticle (BT NP) is a well-known piezoelectric, ferroelectric material, similar to lead zirconate titanate (PZT), the piezoelectric harvesting properties of which have been described and investigated by many researchers [7-10]. Although

research on enhancing the piezo properties of the BT NP by composite technologies and bio-based template-assisted self-assembling technology[11] have been reported, it remains unexploited with respect to biosensing and theranostic applications. Unlike PZT, BT NPs are biocompatible, making them suitable candidates for drug delivery, *in vivo* imaging [12], cancer therapy [13], and self-powered nanosystems[14]. This background prompted us to investigate BT NPs in the field of biosensing for developing self-powered sensors, as reported by our group previously [15],[16]. Instead of harvesting energy separately and integrating it externally with a sensor, a one-stop device having dual functions may be possible. Moreover, vital biomedical information could be determined from the piezoelectric output of a nanogenerator by tailoring its piezoelectric properties for monitoring or sensing biologically important molecules. This suggests a new era of piezo-based biosensing where piezoelectric, piezotronic, and semiconducting properties of BT NPs could play a major role [17],[16],[18]. Thus, tailoring these properties by means of biomolecules can result in a novel biosensing mechanism [17], [19],[20].

Generally, poling leads to orientation of electrical dipoles in BT NPs in the direction of the external electrical field. During mechanical deformation of a nanogenerator, a piezoelectric potential is induced between the top and bottom electrodes due to the stress of the dipoles. This built-in potential causes the flow of free electrons, thus neutralizing the piezoelectric potential [21]. Thus, tailoring the charge-carrier density can result in the piezopotential containing vital information. Adsorption of biomolecules on a piezoelectric material causes changes in the free electrons, so

screening of the piezopotential could have a significant effect on the final output of the NG [20],[22]. The free-carrier density in the conduction band of piezoelectric material tends to flow and screen the positive ionic piezoelectric charges at one end, while leaving the negative ionic piezoelectric charges alone. This principle is called the screening effect which alters the piezoelectric output of the PNG. This output signal then serves both as a biosensor and a source of energy. In this study, the piezoelectric output response of an unpackaged BT film-based NG to glucose was investigated, exploring the screening effect of free carriers on piezo potential due to the presence of glucose molecules. The NG can actively detect glucose molecules as a self-powered sensor without requiring external power (active sensor). This study could provide a prototype for the development of next-generation smart/self-powered nanosystems.

## **5.2. Experimental section**

### **5.2.1. Synthesis of BT NPs**

A conventional solid-state reaction method was used for synthesizing pristine, tetragonal-phase BT NPs. The precursors – BaCO<sub>3</sub> (99.95%, High Purity Chemicals) and TiO<sub>2</sub> (98%, Daejung Chemicals) – were mixed well in acetone using a pestle and mortar for 30 min until a homogeneous powder was obtained (precursors were taken according to the atomic ratio of BaTiO<sub>3</sub>). The homogeneous mixture was then placed inside a combustion boat (alumina) and heated, at a heating rate of 2.5°C/min, to 1,200°C for 2 h in an open-tube furnace. The BT NPs thus formed were taken out of the furnace and cooled naturally [16]. The phase and surface morphology of the as-

synthesized NPs were confirmed by Raman spectroscopy, Fourier-transform infrared (FTIR) spectroscopy, X-ray diffraction (XRD), and Field- emission scanning electron microscopy (FE-SEM) analyses.

### **5.2.2. Fabrication of Al/BT/ITO NG**

Figure 5.1 shows a schematic of the Al/BT/ITO NG, the fabrication of which involved three simple steps: BT film formation, establishment of electrodes and external connections, and fixation within a Kapton frame. The transparent ITO-coated PET (Polyethylene Terephthalate) film served as both the substrate for BT film and a conducting electrode (bottom). A BT film of thickness  $\sim 50 \mu\text{m}$  was formed on the ITO substrate by a simple solution-casting technique. Specifically 5, 10, and 20 % (w/v) BT NPs in 5% (w/v) PVA (poly vinyl alcohol) matrix were dispersed homogeneously for BT film formation. After casting this homogenous mixture on the ITO substrate, it was heat-treated at  $150^\circ\text{C}$  for 1 h in an oven to achieve a uniform polycrystalline film and to eliminate the PVA matrix [15]. A piece of aluminum (Al) foil (thickness,  $\sim 15 \mu\text{m}$ ) positioned on the top of the BT film served as the counter-electrode (top). Copper (Cu) wires were attached to the top and bottom electrodes with a silver (Ag) paste and were used to measure the piezoelectric output voltage and current. Finally, the device was fixed tightly between two Kapton films on both sides of the device as supporting frames to establish firm contact between the electrode and BT film. The active area of the device was  $2 \times 2 \text{ cm}$ , with slight extension of the BT film on one side for placing the glucose molecules for detection. The NG device was poled by applying an electric field

of 5 kV for ~15 h to enhance its piezoelectric properties. This facile, novel device structure leads to a new piezoelectric-based biosensing approach for detecting biologically important molecules.

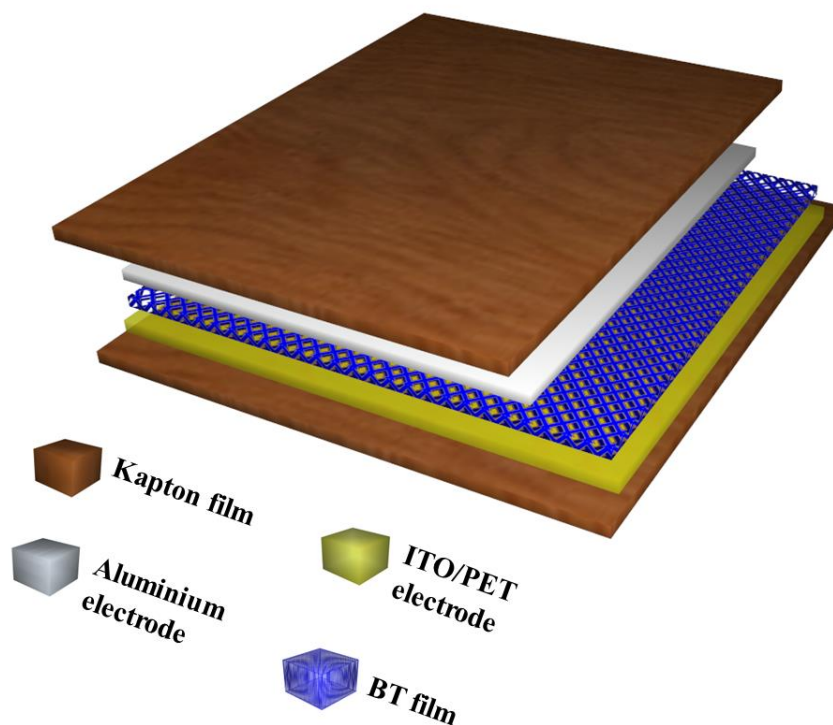


**Figure 5.1.** Schematic diagram of the BaTiO<sub>3</sub> (BT) film-based piezoelectric nanogenerator (PNG) used in this research.

### 5.2.3. Instrumentation

The surface morphology of all samples was characterized using FE-SEM (JSM-6700F; JEOL). An X-ray diffractometer (Rigaku), operating at 40 kV/10 mA and using Cu K $\alpha$  radiation ( $2\theta$  range, 20-80°) at room temperature, was used to confirm crystalline phase formation in the BT NPs. Raman spectra were recorded with an excitation source of 514

nm using a high-throughput, single-stage spectrometer (Lab RAM; HR Evaluation, Japan). The open circuit voltage ( $V_{oc}$ ) and short circuit current ( $I_{sc}$ ) of the NG were recorded with a nanovoltmeter (2182A; Keithley) and a picoammeter (6485; Keithley), respectively. The NG output was measured by triggering with a mechanical load ( $F = 0.2$  N) using a linear motor (E1100).

### 5.3. Results and Discussion

#### 5.3.1. Structural characterization

The structural morphology, size, and phase of the as-synthesized BT NPs were confirmed through characterization techniques. The XRD and Raman shift results were used to confirm the phase of the BT NPs. The characteristic peaks of BT NPs at  $252\text{ cm}^{-1}$ ,  $305\text{ cm}^{-1}$ , and  $518\text{ cm}^{-1}$  in the Raman spectrum (Figure 5.2 a) confirmed the tetragonal phase of BT NPs, indicating the presence of  $\text{Ti}^{4+}$  ions in the parent lattice; the peaks at  $305\text{ cm}^{-1}$  and  $518\text{ cm}^{-1}$  were assigned to the A1 and B1 modes, respectively [23]. Moreover, the XRD diffraction pattern (Figure 5.2 b) was consistent with the reference ICDD 98-001-3771 pattern and the peak splitting observed at  $45^\circ$  (200/002; inset; Figure 5.2 b) confirmed the tetragonal nature of the pristine BT NPs [14]. Thus, the Raman shift and XRD pattern indicated that the BT NPs had good crystallinity, with an excellent ferroelectric tetragonal phase. The surface morphologies of the BT film and pristine BT NPs were analyzed using FE-SEM. The low-magnification SEM image (Figure 5.2 c) showed a uniform distribution of BT NPs in the BT film surface from the top view at a  $2\text{-}\mu\text{m}$  scale. The inset shows FE-SEM micrographs of BT NPs having

random shapes with sizes  $\leq 200$  nm. The cross-sectional view of the BT film showed a uniform film thickness of  $\sim 50$   $\mu\text{m}$  (Figure 5.2 d). Additionally, the FTIR spectrum showed a Ti-O stretch signal at  $\sim 550$   $\text{cm}^{-1}$ , again confirming the characteristics of the BT NPs (Figure 5.3) [24].

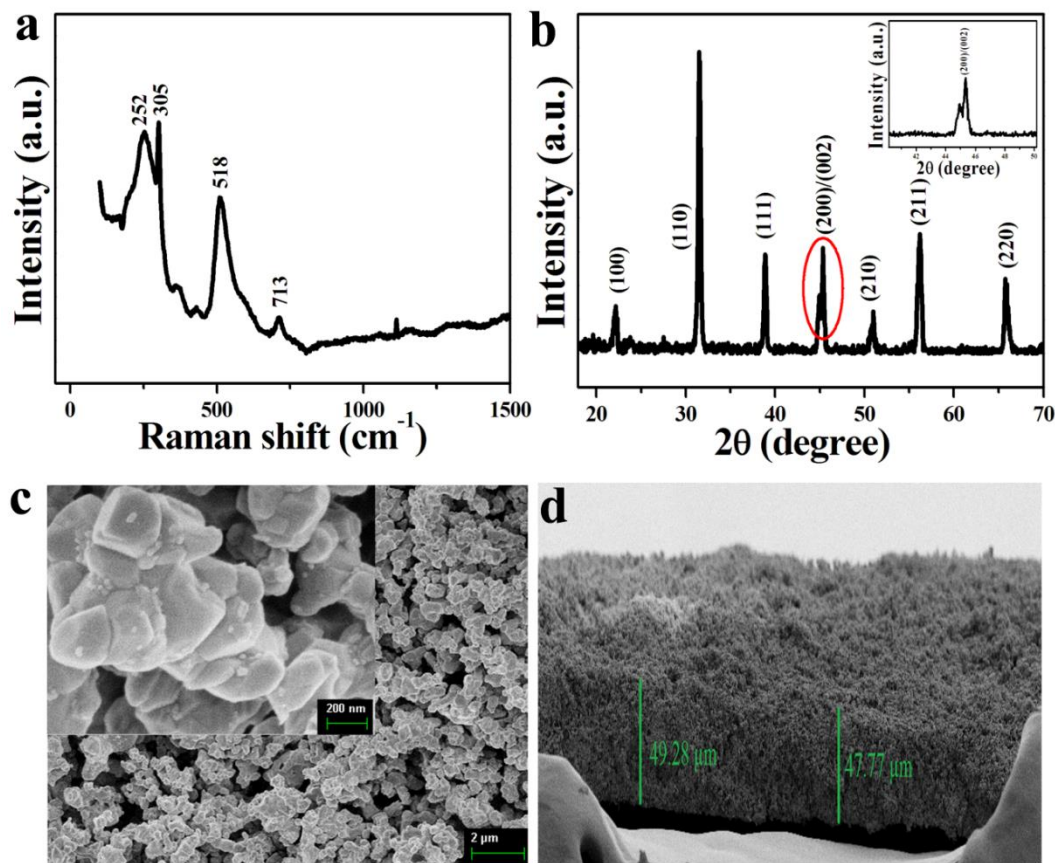


**Figure 5.2.** Structural characterization. (a) Raman spectrum and (b) X-ray diffraction (XRD) pattern of the as-synthesized BaTiO<sub>3</sub> nanoparticles (BT NPs). Field-emission scanning electron microscopy (FE-SEM) micrographs of (c) BT NPs film at 2  $\mu\text{m}$  scale (inset shows BT NPs  $\leq 200$  nm) (d) a cross-sectional view of BT NPs film with film thickness of  $\sim 50$   $\mu\text{m}$ .

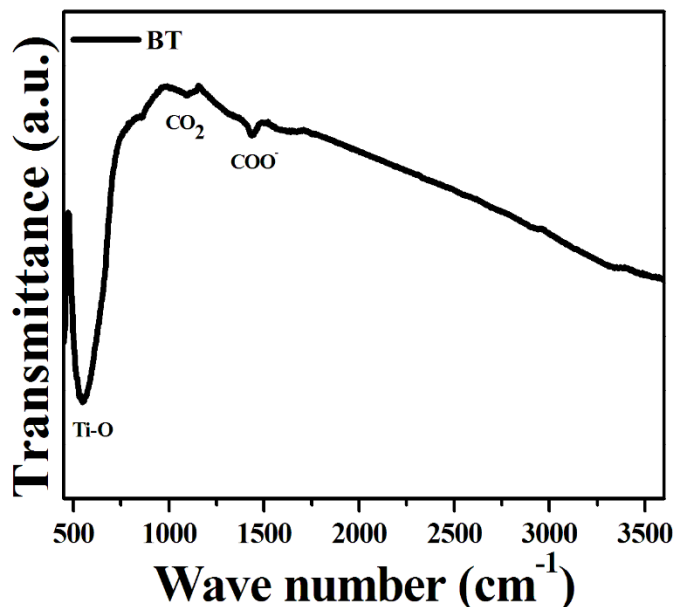


**Figure 5.3.** Fourier-transform infrared (FTIR) spectrum of as-synthesized BT nanoparticles.

### 5.3.2. NG device optimization and characterization

Al/BT/ITO NGs of three different weight ratios of BT NPs (5, 10, and 20% w/v), with a  $2 \times 2$  cm active area, were fabricated as described in the Experimental section. The  $V_{oc}$  and  $I_{sc}$  of these NGs are given in Figure 5.4 and Figure 5.5 a. With an increase in BT concentration, the output voltage and current of the nanogenerator increased in a linear fashion (Figure 5.5 a). NG with a higher % w/v of BT NPs (20% w/v) showed higher performance compared with lower % w/v BT NPs, giving a peak-to-peak  $V_{oc}$  of  $\sim 30$  V (Figure 5.5 b) and a peak-to-peak  $I_{sc}$  of  $\sim 340$  nA (Figure 5.5 c).

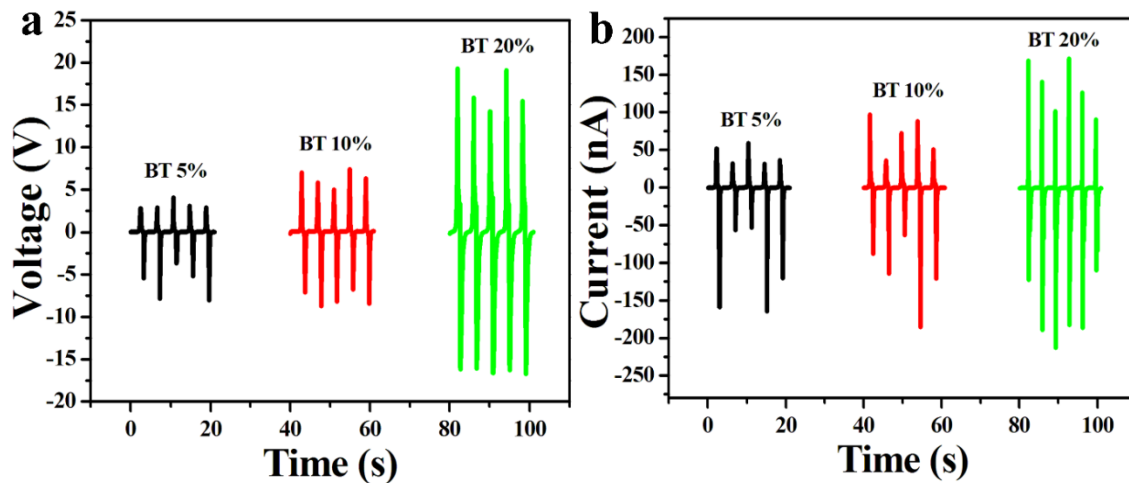


**Figure 5.4.** (a) Open circuit voltage ( $V_{oc}$ ) and (b) short-circuit current ( $I_{sc}$ ) of BT film-based NGs fabricated with 5, 10, and 20% w/v BT NPs at a mechanical load of  $F = 0.2$  N.

The electrical outputs of the nanogenerator were measured using a programmed linear motor by applying a periodic compressive load ( $F = 0.2$  N). When this force was applied perpendicularly to the Al/BT/ITO nanogenerator that included a BT film of thickness  $\sim 50$   $\mu\text{m}$ , the output voltage reached  $\sim 30$  V (Figure 5.5b inset shows an enlarged image of a single peak-to-peak voltage graph), and the output current was  $\sim 340$  nA (peak-to-peak). The piezoelectric potential generated from this device (20% w/v) could light up nine commercial green LEDs (Light-emitting diode) (Figure 5.5 b; inset), confirming its ability as a potential energy source for driving low-power electronic gadgets and sensors, as well as being an active biosensing device. Moreover, this NG gave a stable output voltage of  $\sim 30$  V with no degradation, even for a period of 600 s under a

mechanical force of 0.2 N (Figure 5.5 d), confirming device stability (inset shows enlarged image).

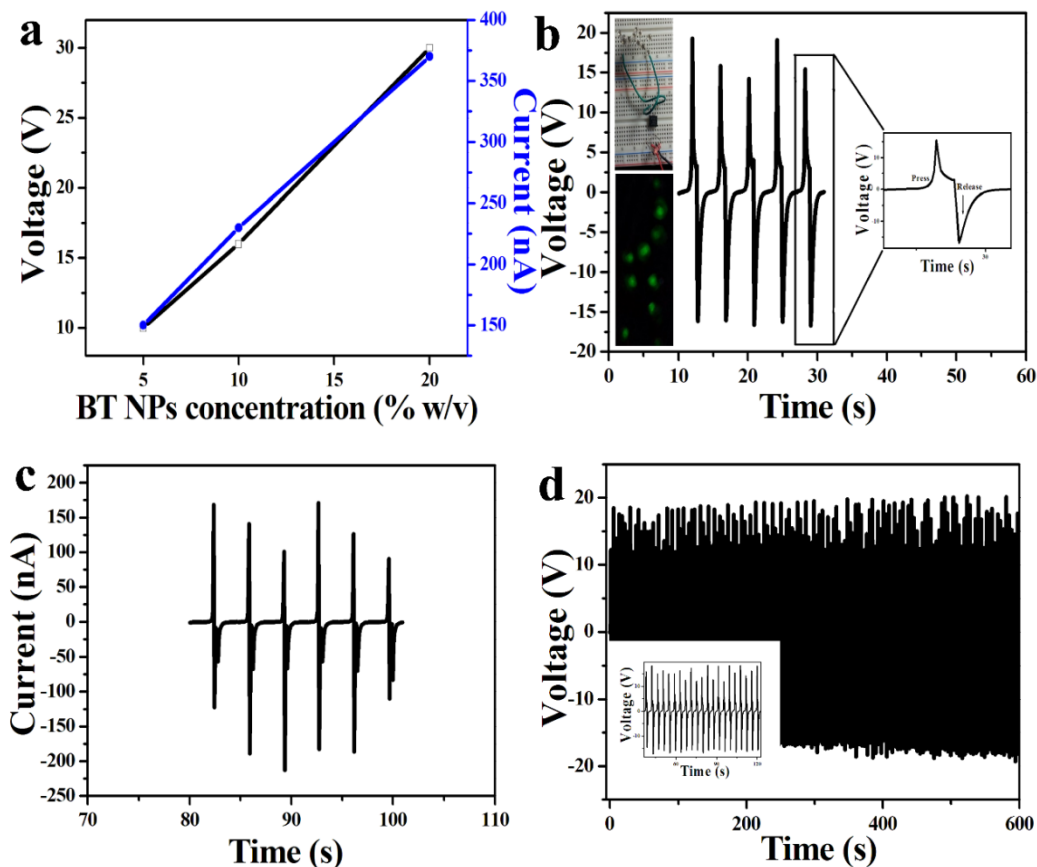


**Figure 5.5.** Electrical characterization of NG. (a) Output voltage and current of BT film-based nanogenerator (NG) as a function of different concentrations of BT NPs (% w/v) under a mechanical load ( $F = 0.2$  N). (b) Open circuit voltage ( $V_{oc}$ ) (inset: enlarged image of a single peak-to-peak voltage graph; commercial green light-emitting diodes (LEDs) lit using the piezoelectric potential generated and (c) short-circuit current ( $I_{sc}$ ) of BT-film based NG (20% w/v). (d) Stable output voltage of NG (20% w/v; under a load of  $F = 0.2$  N) for a period of 600 s with no degradation.

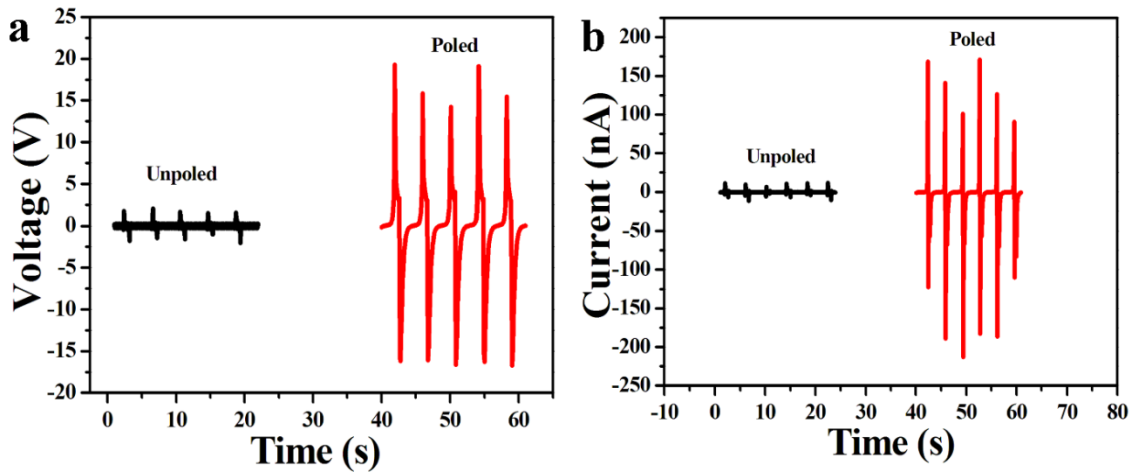


**Figure 5.6.** (a) The  $V_{oc}$  and (b)  $I_{sc}$  of BT film-based NGs (20% w/v BT NPs) before and after poling at an electric field of 5 kV for 15 h (at a mechanical load of  $F = 0.2$  N).

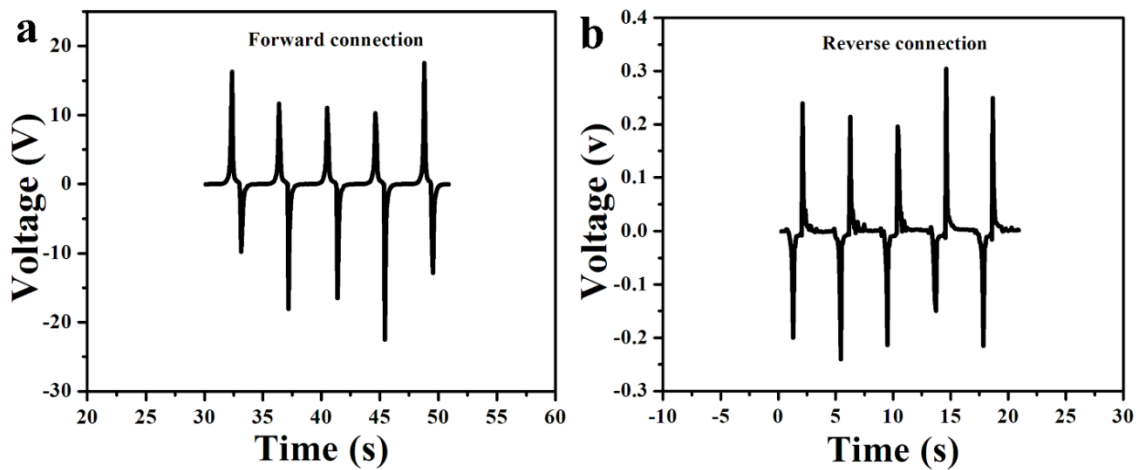


**Figure 5.7.** Polarity switching test. The  $V_{oc}$  of BT film-based NG (20% w/v BT NPs) during (a) forward connection and (b) reverse connection (at a mechanical load of  $F = 0.2$  N).

The NG device poling condition was optimized to an electric field of 5 kV for about 15 h. The piezoelectric output of the NG (20% w/v) before and after poling

(Figure 5.6 ) confirmed the orientation of dielectric poles in the BT NPs, due to the applied electric field, thus leading to an enhanced piezoelectric potential.

Polarity switching tests were performed to confirm that the output electrical signals came from the NG and were not due to contact electrification between the measurement set-up and device. An opposite output signal when the device was connected in reverse confirmed that the signal was from the device (Figure 5.7.).

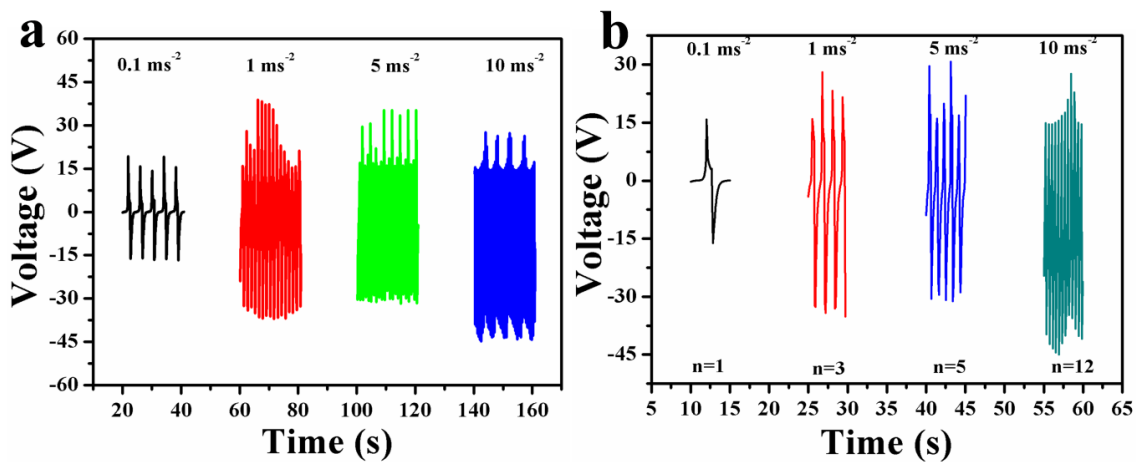


**Figure 5.8.** The Open circuit voltage ( $V_{oc}$ ) of the PNG (a) subjected to different accelerations  $0.1 \text{ ms}^{-2}$ ,  $1 \text{ ms}^{-2}$ ,  $5 \text{ ms}^{-2}$  and  $10 \text{ ms}^{-2}$  (time dependence of the compressive and decompressive load action on PNG). (b) representing number of cycles ( $n$ ; sinusoidal peaks) for a time period of 5 seconds when subjected to different accelerations.

Moreover, time dependent compressive and decompressive force on the PNG was studied by subjecting the device to four different accelerations namely  $0.1 \text{ ms}^{-2}$  ( $F=0.2\text{N}$ ),  $1 \text{ ms}^{-2}$  ( $F=2\text{N}$ ),  $5 \text{ ms}^{-2}$  ( $F=10\text{N}$ ) and  $10 \text{ ms}^{-2}$  ( $F=20\text{N}$ ) for which the device

gave respective output voltage as shown in Figure 5.8 a. With increase in acceleration, there is corresponding increase in peak amplitude and frequency. From Figure 5.8 b, we can observe that the number of cycles ( $n$ ; sinusoidal waves) for a time period of 5 seconds increases with increase in acceleration. This depicts the time dependence of the compressive and decompressive load action on PNG. Among all these accelerations, device at  $0.1 \text{ ms}^{-2}$  ( $F=0.2\text{N}$ ) showed best performance with respect to peak pattern behavior and uniformity for a constant period of time, suitable for our purpose of study to be used as a self-powered sensor with dual functions as sensor and energy harvester. Hence, this acceleration was chosen as the optimum one and further used for all measurements throughout the study.

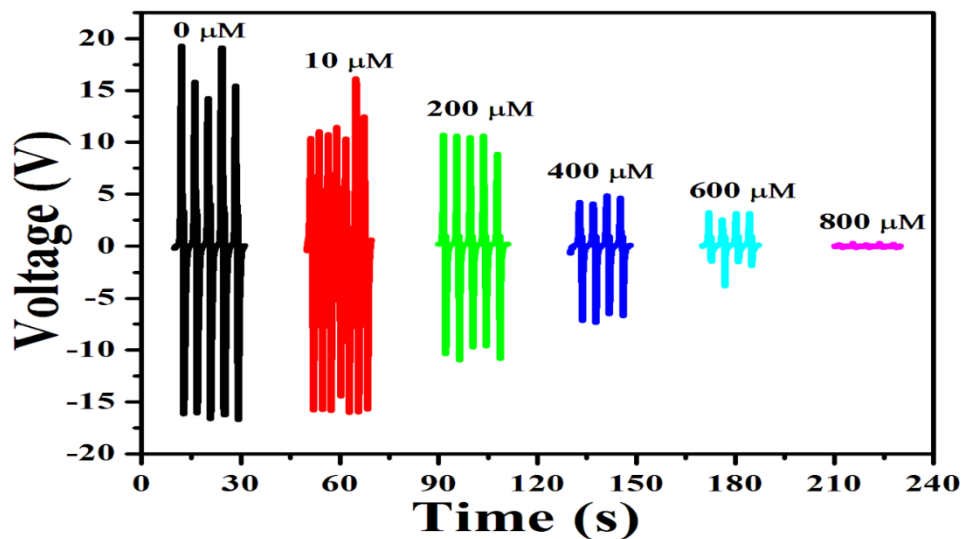


**Figure 5.9.** Active (self-powered) glucose sensor. The piezoelectric output of the NG (20% w/v) in the presence of different glucose concentrations (0 to 800  $\mu\text{M}$ ) at  $F = 0.2 \text{ N}$  (the piezoelectric output voltage of the device was linearly dependent on the concentration of glucose).

### 5.3.3. Self-powered/ active glucose sensor

The output voltage (piezoelectric potential) generated from the as-fabricated Al/BT/ITO NG can act not only as an energy source but can also be used as a biosensing signal. Thus, the NG has two functions: first, as an energy source (in that it can produce piezoelectric output power), and second as a biosensor (because the output of the NG is also a measure of chemisorbed glucose molecules). The piezoelectric potential generated by the device in the presence of different concentrations of glucose was used as a biosensing signal for glucose detection. The linear concentration range of glucose studied was 0 to 800  $\mu\text{M}$ . In the absence of glucose, the piezoelectric output voltage under the compressive force was  $\sim 30$  V. With the addition of 10  $\mu\text{M}$  glucose, the piezoelectric output voltage of the NG decreased and continued to decrease with further addition of glucose molecules. The piezoelectric output voltage of the device was linearly dependent on the glucose concentration. Glucose solution was added to the slight extension of the BT film on one side of the device from which it will spread throughout the device through capillary action. The amount of glucose solution used is 50  $\mu\text{l}$  which will not cause problems like stagnation or short circuits. Moreover, after adding the glucose solution, the device was allowed to dry at 37°C for 15 minutes just to ensure that there will be no short circuit due to contact between solution and electrode. This time period of 15 minutes is sufficient for our experimental conditions as the device is not completely immersed in glucose solution in which case it has to be dried for an hour or more. After this, measurements were taken by subjecting the device to compressive and decompressive force using linear motor. When the concentrations of

glucose were 10  $\mu\text{M}$ , 200  $\mu\text{M}$ , 400  $\mu\text{M}$ , 600  $\mu\text{M}$ , and 800  $\mu\text{M}$ , the piezoelectric output voltages were 29 V, 22 V, 13.5 V, 6 V, and 0.4 V, respectively (Figure 5.9.).

The calibration curve obtained from Figure 5.9 fitted the equation  $Y = A + B \times X$ , where  $A = 29.41003$ ,  $B = -0.03762$ , and  $R^2 = 0.9961$  as shown in Figure 5.10 a. The experimentally detected limit of detection (LOD) was 10  $\mu\text{M}$ . The response of the self-powered active biosensor based on the voltage variation in function of glucose concentration can be given as

$$r = \frac{|V_0 - V_i|}{V_0} \times 100\% \quad (1)$$

where  $V_0$  and  $V_i$  are the piezoelectric output without and with glucose, respectively.

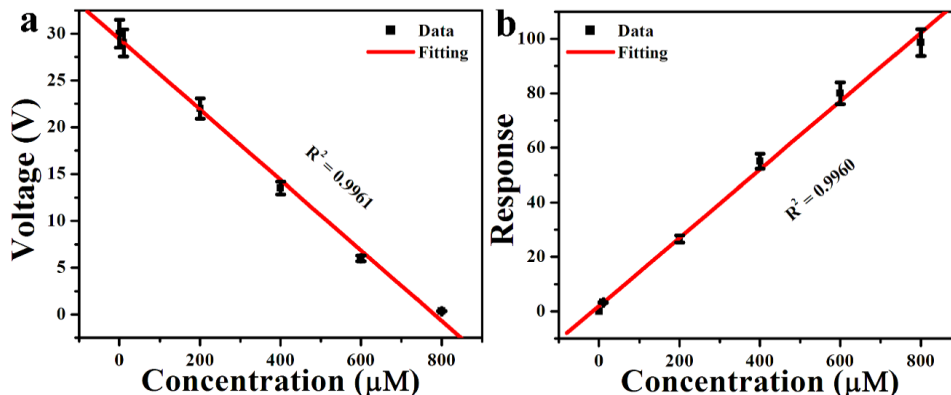


**Figure 5.10.** (a) Relationship between the piezoelectric output of NG and the concentration of glucose. (b) Dependence of the response  $r$  on the concentration of glucose.

The responses of the device for 10  $\mu\text{M}$ , 200  $\mu\text{M}$ , 400  $\mu\text{M}$ , 600  $\mu\text{M}$ , and 800  $\mu\text{M}$  glucose concentrations under a mechanical load of  $F = 0.2 \text{ N}$  were 3.3%, 26.6%, 55%,

80%, and 98.6%, respectively. The sensitivity can be calculated from the slope of the response curve (Figure 5.10 b) which gives the response of the device for per  $\mu\text{M}$  glucose concentration change. Thus, the calculated sensitivity of 0.125 (i.e.  $\sim 125 \text{ mV}/\mu\text{M}$  glucose concentration) is in agreement with the peak resolution of the active sensor which is 117 mV (8 bit ADC) as shown in Figure 5.11. Thus, with a vertical range of 30 V, voltage differences as much as 125 mV can be ideally resolved using this active sensor.

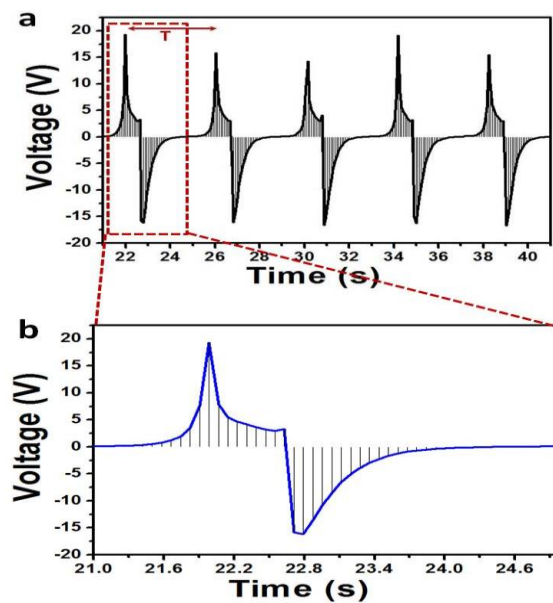


**Figure 5.11.** Resolution of peak amplitude. (a) The Open circuit voltage ( $V_{oc}$ ) of the PNG (5 peak cycles) divided into discrete levels by Discrete Fourier transform (DFT) (b) enlarged image of one peak cycle.

Resolution is the smallest input voltage change a digitizer can capture. It can be expressed in bits (LSB), in proportions, or in percent of full scale. It can also be explained through an n-bit analog-to-digital converter (ADC) where resolution is a

function of how many parts the maximum signal can be divided into. The formula to calculate resolution is  $2^n$ , where  $n$  denotes the bits. Figure 5.11. shows single sine wave peak divided into multiple discrete step amplitudes (by assuming 5 bit ADC) such as 32 peaks.

Thus,

$$2^5 = 32$$

Therefore, the best resolution is 1 part of 32 (32 discrete levels)

i.e.  $1/32 = 0.03125$

$\approx 3.125\%$  of the full scale.

In present case, the resolution of active glucose sensor calculated from the response curve (Figure 5.10 b) is  $125\text{mV}/\mu\text{M}$  glucose concentration. Thus an 8 bit ADC with 256 discrete levels (step amplitudes) will give such a resolution. According to the resolution formula,

$$2^8 = 256$$

Therefore, the best resolution is 1 part of 256

i.e.  $1/256 = 0.00390625$

$\approx 0.390625\%$  of the full scale.

The peak-to-peak amplitude of voltage signal is 30 V and the corresponding best resolution is  $(0.390625 * 30 \text{ V})/100 = 117 \text{ mV}$  (approximately equal to 125 mV). Thus, with a vertical range of 30 V, voltage differences as much as 125 mV can be ideally resolved using this active sensor (8 bit ADC).

**Table 5.1.** Comparison among glucose sensors based on different detection techniques

<b>Material employed</b>	<b>Detection technique</b>	<b>Limit of detection</b>	<b>Linear range concentration</b>	<b>Reference</b>
CuO nanowire	Amperometric (non-enzymatic)	49 nM	0.4 $\mu$ M to 2 mM	[31]
PtNi-Graphene	Amperometric (enzymatic)	10 $\mu$ M	up to 35 mM	[32]
Nanostructured TiO <sub>2</sub>	Amperometric (enzymatic)	100 nM	150 $\mu$ M - 1.2 mM	[33]
BaTiO <sub>3</sub> NPs film	<i>I-V</i> technique	7.94 $\mu$ M	0 - 1 mM	[15]
Pyramid-shaped porous ZnO	Amperometric (enzymatic)	10 $\mu$ M	0.05-8.2 mM	[34]
Ni	Flow-injection analysis (non- enzymatic)	0.04 mM	0.1-2.5 mM	[35]
3D porous ZnO– CuO hierarchical nanocomposites	Amperometric (non-enzymatic)	0.21 $\mu$ M.	up to 1.6 mM	[36]
Porous Cu <sub>2</sub> O microcubes	Amperometric (non-enzymatic)	1.5 $\mu$ M	0-1.5mM	[37]
BaTiO <sub>3</sub> NP film	Piezoelectric biosensing	10 $\mu$ M	0 to 800 $\mu$ M	<b>This work</b>

NP, nanoparticle

#### 5.3.4. Proposed working mechanism of Al/BT/ITO NG as active glucose biosensor

With no force, there is no generation of a piezoelectric potential (Figure 5.12 a). Mechanical energy is converted into electrical energy when a compressive force is applied perpendicularly to the BT film-based NG due to the orientation of dielectric poles in the BT NPs, generating a piezoelectric potential. The piezoelectric potential generated on both sides of the film, in turn, induces inductive charges on the top and bottom electrodes, as a result of electrostatic force. This potential difference between the electrodes results in transient flow of electrons through the external circuit in response to the periodic mechanical deformation (Figure 5.12 b). Moreover, the piezoelectric output of the NG depends on the piezoelectric coefficient ( $d_{33}$ ), [16] given by

$$V_{OC} = \left(\frac{d_{33}}{K\epsilon_0}\right)\sigma Yt \quad (2)$$

$$I_{SC} = g_{33}K\epsilon_0YA\epsilon \quad (3)$$

Where,  $V_{oc}$  is open circuit voltage,  $d_{33}$  is piezoelectric coefficient of the material,  $\sigma$  is the strain (perpendicular direction),  $Y$  is Young's modulus,  $T$  is the thickness of the device,  $K$  is the relative permittivity,  $\epsilon_0$  is the permittivity of free space,  $I_{sc}$  is short-circuit current,  $g_{33}$  is the piezoelectric voltage constant  $\left(\frac{d_{33}}{K\epsilon_0}\right)$ ,  $A$  is the cross-sectional area of the device and  $\epsilon$  is the applied strain.

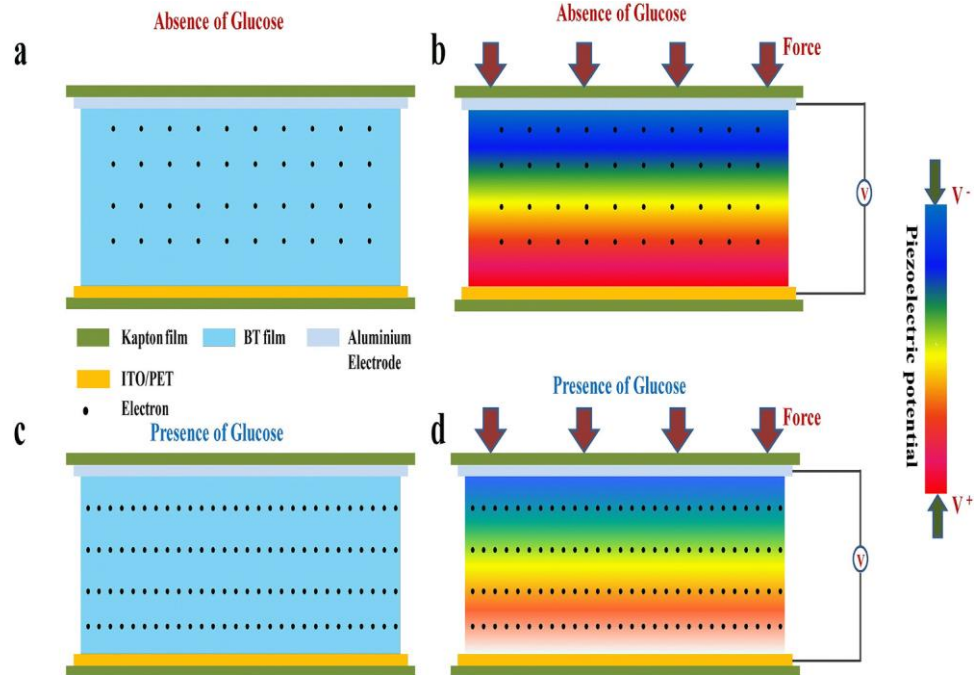


**Figure 5.12.** Schematic representation of the proposed mechanism of BT film-based NG during active biosensing of glucose.

A change in the free-carrier density in the BT film will influence the piezoelectric output of the NG due to its screening effect on the piezoelectric polarization charges at the interface. The electron density of the BT film will be affected by the adsorption of biomolecules, which in turn can establish a local electric field and greatly change the screening of the piezoelectric field [19]. Chemisorption of glucose molecules on the BT film will increase its electron density and thus provide a gate potential (Figure 5.12c). This increase in free-carrier density in the conduction band of BT will screen the positive ionic piezoelectric charges at one end, leaving the negative ionic piezoelectric charges alone, thereby reducing the piezoelectric output (Figure 5.12 d) [20],[22],[25]. Thus, with different concentrations of glucose molecules, the

piezoelectric output of the nanogenerator will be reduced due to the increased electron density, acting as a biosensing signal.

The change in charge-carrier density can be assessed directly by the change in resistance of the BT film through  $I$ - $V$  (current-voltage) studies, as reported previously[15]. Glucose molecules release  $e^-$  to the BT NP film, which will increase the charge carrier density of the film, resulting in lowering of the Schottky barrier height on the drain side ( $\Phi'_d$ ); thus, the interface between the BT NP film and the metal electrode (MS) significantly increases the output current of the BT film-based glucose sensor with a metal-semiconductor-metal (MSM) device structure, as explained previously. Glucose molecules have a Lewis base site, the OH group, whereas the BT NP film has  $Ba^{2+}$  and  $Ti^{4+}$  ionic species, which are Lewis acids. The Lewis base (OH groups) reacts with Lewis acids ( $Ba^{2+}$  and  $Ti^{4+}$ ) and releases electrons ( $e^-$ ), leading to the chemisorption of glucose molecules on to BT NPs, where the glucose is oxidized and releases electrons[26],[15]. The glucose molecules (Lewis base) on the surface of BT film (Lewis acid) provide a gate potential, and the field effect eventually influences the charge carrier density (electrons) in the BT film (Figure 5.12 c), which varies the screening effect of free-carriers on the piezoelectric output (Figure 5.12 d). The response of the active NG to glucose molecules is consistent with the  $I$ - $V$  characteristics of the Ag-BT-Ag device (MSM) in our previous report [15]. There is a typical MSM structure in our NG device (Al-BT-ITO) [4],[27],[28],[29]. The free-carrier density in BT film increases with an increase in glucose concentration and thus the piezoelectric output of the NG containing the glucose-sensing information decreases.

### 5.3.5. Interference studies

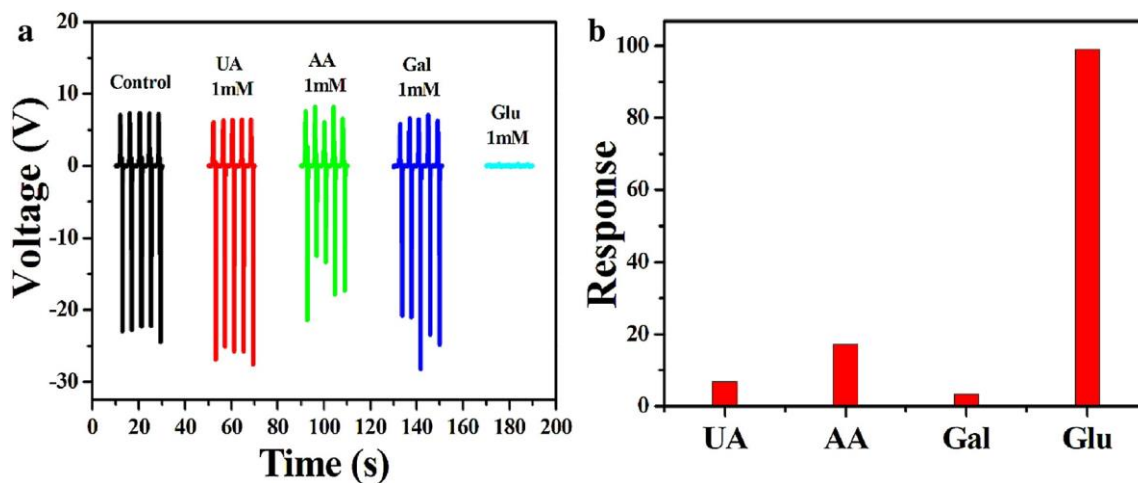


**Figure 5.13.** Interference study. (a) The piezoelectric output of the NG in the presence of 1 mM glucose and interferents such as 1 mM uric acid (UA), 1 mM ascorbic acid (AA) and 1 mM galactose (Gal). (b) Response of NG based on the voltage variation in the presence of glucose and interferents.

The specificity of the sensor was confirmed through an interference study using 1 mM uric acid (UA), ascorbic acid (AA), and galactose (Gal), respectively, as interferents. The normal physiological level of glucose (3–8 mM) is much higher than the level of interfering species (0.1 mM) [30]. The piezoelectric output voltage of the NG in the presence of glucose (1 mM) and interfering species (1 mM) is shown in Figure 5.13 a. The piezoelectric output voltage of the NG in the absence of any biomolecule was ~30 V (peak-to-peak); in the presence of UA, AA, Gal, and Glu it was ~32 V, ~24 V, ~31 V, and ~0.28 V, respectively. There was no significant change in the piezoelectric output of

the nanogenerator for interferents but for glucose there was a significant change (potential drop). Thus, even at higher concentration of interferents (1mM), the response of the device to interferents was negligible when compared with that to glucose. The device (active sensor) showed a 99% response to glucose, but responses of only 6.8% to UA, 17.2% to AA, and 3.4% to Gal (Figure 5.13 b). The proposed sensor thus showed high selectivity towards glucose even in the presence of potent interferents and its analytical throughput (LOD and linear concentration range) is comparable to existing conventional glucose sensors (Table 5.1).

#### **5.4. Conclusions**

In summary, a BT film-based NG was developed for energy harvesting and active biosensing. This is the first report of a BT film-based PNG for actively sensing glucose biomolecules. The simple, novel device structure leads to new dimensions in diagnosis, namely piezoelectric-based biosensing. The piezoelectric output signal from the device contains the biosensing signal, thus having a dual purpose as a generator and biosensor. The active glucose sensor has an LOD of 10  $\mu$ M and is highly selective towards glucose. The screening effect of charge carriers (due to the adsorption of biomolecules) on the piezoelectric output of the nanogenerator was exploited in this novel sensing approach. This study may pave the way for future studies on developing self-powered nanosystems for implantable and multifunctional point-of-care diagnostic devices.

## References

- [1] Park, K.; Son, J. H.; Hwang, G.; Jeong, C. K.; Ryu, J.; Koo, M.; Choi, I.; Lee, S. H.; Byun, M.; Wang, Z. L.; et al. Highly Efficient Flexible Piezoelectric PZT Thin Film Nanogenerator on Plastic Substrates. *Adv Mater.* 26 (2014) 2514-2520.
- [2] Kwon, S.; Kim, W. K.; Park, J.; Yang, Y.; Yoo, B.; Han, C. J.; Kim, Y. S. Fabric Active Transducer Stimulated by Water Motion for Self- Powered Wearable Device. *ACS Appl Mater Interfaces.* 8 (2016) 24579-24584.
- [3] Zhang, K.; Wang, Z. L.; Yang, Y. Conductive Fabric Based Stretchable Hybridized Nanogenerator for Scavenging Biomechanical Energy Conductive Fabric Based Stretchable Hybridized Nanogenerator for Scavenging Biomechanical Energy. *ACS Nano*, 10 (2016) 4728–4734.
- [4] Yu, R.; Pan, C.; Chen, J.; Zhu, G.; Wang, Z. L. Enhanced Performance of a ZnO Nanowire-Based Self-Powered Glucose Sensor by Piezotronic Effect. *Adv. Funct. Mater.* 23 (2013) 5868–5874.
- [5] Alam, M.; Mandal, D. Native Cellulose Microfiber Based Hybrid Piezoelectric Generator for Mechanical Energy Harvesting Utility. *ACS Appl. Mater. Interfaces*, 8 (2016) 1555–1558.
- [6] Hwang, G.; Park, H.; Lee, J.; Oh, S.; Park, K.; Byun, M.; Park, H.; Ahn, G.; Jeong, C. K.; No, K.; et al. Self-Powered Cardiac Pacemaker Enabled by Flexible Single Crystalline PMN-PT Piezoelectric Energy Harvester. *Adv Mater.* 26 (2014) 4880-4887.
- [7] Park, K. Il; Lee, M.; Liu, Y.; Moon, S.; Hwang, G. T.; Zhu, G.; Kim, J. E.; Kim,

- S. O.; Kim, D. K.; Wang, Z. L.; et al. Flexible Nanocomposite Generator Made of BaTiO<sub>3</sub> Nanoparticles and Graphitic Carbons. *Adv. Mater.* 24 (2012) 2999–3004.
- [8] Park, K.-I.; Xu, S.; Liu, Y.; Hwang, G.-T.; Kang, S.-J. L.; Wang, Z. L.; Lee, K. J. Piezoelectric BaTiO<sub>3</sub> Thin Film Nanogenerator on Plastic Substrates. *Nano Lett.* 10 (2010) 4939–4943.
- [9] Yan, J.; Jeong, Y. G. High Performance Flexible Piezoelectric Nanogenerators Based on BaTiO<sub>3</sub> Nanofibers in Different Alignment Modes. *ACS Appl. Mater. Interfaces*, 8 (2016) 15700–15709.
- [10] Guoquan Suo; Yanhao Yu; Zhiyi Zhang; Shifa Wang; Ping Zhao; Jianye Li; Xudong Wang. Piezoelectric and Triboelectric Dual Effects in Mechanical Energy Harvesting Using BaTiO<sub>3</sub> / Polydimethylsiloxane Composite Film. *ACS Appl. Mater. Interfaces*, 8 (2016) 34335–34341.
- [11] Shin, D.-M.; Han, H. J.; Kim, W.-G.; Kim, E.; Kim, C.; Hong, S. W.; Kim, H. K.; Oh, J.-W.; Hwang, Y.-H. Bioinspired Piezoelectric Nanogenerators Based on Vertically Aligned Phage Nanopillars. *Energy Environ. Sci.* 8 (2015) 3198–3203.
- [12] Hsieh, C.-L.; Grange, R.; Pu, Y.; Psaltis, D. Bioconjugation of Barium Titanate Nanocrystals with Immunoglobulin G Antibody for Second Harmonic Radiation Imaging Probes. *Biomaterials* 31 (2010) 2272–2277.
- [13] FarrokhTakin, E.; Ciofani, G.; Puleo, G. L.; de Vito, G.; Filippeschi, C.; Mazzolai, B.; Piazza, V.; Mattoli, V. Barium Titanate Core–Gold Shell Nanoparticles for Hyperthermia Treatments. *Int. J. Nanomedicine* 8 (2013) 2319–2331.

- [14] Alluri, N. R.; Saravanakumar, B.; Kim, S. J. Flexible, Hybrid Piezoelectric Film (BaTi<sub>(1-x)</sub>Zr<sub>x</sub>O<sub>3</sub>)/PVDF Nanogenerator as a Self-Powered Fluid Velocity Sensor. *ACS Appl. Mater. Interfaces* 7 (2015) 9831–9840.
- [15] Selvarajan, S.; Rao, N.; Chandrasekhar, A.; Kim, S. Sensors and Actuators B : Chemical BaTiO<sub>3</sub> Nanoparticles as Biomaterial Film for Self-Powered Glucose Sensor Application. *Sensors Actuators B. Chem.* 234 (2016) 395–403.
- [16] Selvarajan, S.; Rao, N.; Chandrasekhar, A. Biosensors and Bioelectronics Direct Detection of Cysteine Using Functionalized BaTiO<sub>3</sub> Nanoparticles Film Based Self-Powered Biosensor. *Biosens. Bioelectron.* 91 (2017) 203–210.
- [17] Ruomeng Yu; Caofeng Panab; Zhong Lin Wang. High performance of ZnO nanowire protein sensors enhanced by the piezotronic effect. *Energy Environ. Sci.*, 6 (2013) 494-499
- [18] Yu, R.; Niu, S.; Pan, C.; Wang, Z. L. Piezotronic Effect Enhanced Performance of Schottky-Contacted Optical, Gas, Chemical and Biological Nanosensors. *Nano Energy* (2015) 1–28.
- [19] Yeh, B. P.; Li, Z.; Wang, Z. L. Schottky-Gated Probe-Free ZnO Nanowire Biosensor. *Adv. Mater.* (2009) 4975–4978.
- [20] Zhao, Y.; Deng, P.; Nie, Y.; Wang, P.; Zhang, Y.; Xing, L. Biosensors and Bioelectronics Biomolecule-Adsorption-Dependent Piezoelectric Output of ZnO Nanowire Nanogenerator and Its Application as Self-Powered Active Biosensor. *Biosens. Bioelectron.* 57 (2014) 269–275.
- [21] Saravanakumar, B.; Soyoon, S.; Kim, S. Self-Powered pH Sensor Based on a

- Flexible Organic – Inorganic Hybrid Composite Nanogenerator. *ACS Appl. Mater. Interfaces*. 6 (2014) 13716–13723.
- [22] Zhao, Y.; Fu, Y.; Wang, P.; Xing, L.; Xue, X. Highly Stable Piezo-Immunoglobulin-Biosensing of a SiO<sub>2</sub>/ZnO Nanogenerator as a Self-Powered/active Biosensor Arising from the Field Effect Influenced Piezoelectric Screening Effect. *Nanoscale*. 7 (2015) 1904–1911.
- [23] Hayashi, H.; Nakamura, T.; Ebina, T. In-Situ Raman Spectroscopy of BaTiO<sub>3</sub> Particles for Tetragonal–cubic Transformation. *J. Phys. Chem. Solids*. 74 (2013) 957–962.
- [24] Xue, X.; Nie, Y.; He, B.; Xing, L.; Zhang, Y. Surface Free-Carrier Screening Effect on the Output of a ZnO Nanowire Nanogenerator and Its Potential as a Self-Powered Active Gas Sensor. *Nanotechnology*. 24 (2013) 225501
- [25] Kuang, Q.; Lao, C.; Wang, Z. L.; Xie, Z.; Zheng, L. High-Sensitivity Humidity Sensor Based on a Single SnO<sub>2</sub> Nanowire. *J. Am. Chem. Soc.* 129 (2007) 6070–6071.
- [26] Zhou, J.; Gu, Y.; Fei, P.; Mai, W.; Gao, Y.; Yang, R.; Bao, G.; Wang, Z. L. Flexible Piezotronic Strain Sensor. *Nano Lett.* 8 (2008) 3035–3040.
- [27] Zhou, J. Indium Tin Oxide (ITO) Deposition, Patterning and Schottky Contact Fabrication. *Applied Physics Letters*. 88 (2006)
- [28] Hong, W.; Song, J.; Hong, H.; Ban, K. Highly Reflective and Low Resistance Indium Tin Oxide / Ag Ohmic Contacts to P-Type GaN for Flip-Chip Light. *Electrochemical and Solid-State Letters*, 8 (2005) 320–323.

- [29] Wang, C.; Yin, L.; Zhang, L.; Gao, R. Ti / TiO<sub>2</sub> Nanotube Array / Ni Composite Electrodes for Nonenzymatic Amperometric Glucose Sensing. *J. Phys. Chem.* 114 (2010) 4408–4413.
- [30] Ćulić-Viskota, J.; Dempsey, W. P.; Fraser, S. E.; Pantazis, P. Surface Functionalization of Barium Titanate SHG Nanoprobes for in Vivo Imaging in Zebrafish. *Nat. Protoc.* 7 (2012) 1618–1633.
- [31] Zhuang, Z.; Su, X.; Yuan, H.; Sun, Q.; Choi, M. M. F. An Improved Sensitivity Non-Enzymatic Glucose Sensor Based on a CuO Nanowire Modified Cu Electrode. *Analyst.* 133 (2008) 126–132.
- [32] Gao, H.; Xiao, F.; Ching, C. B.; Duan, H. One-Step Electrochemical Synthesis of PtNi Nanoparticle-Graphene Nanocomposites for Nonenzymatic Amperometric Glucose Detection. *ACS Appl. Mater. Interfaces.* 3 (2011) 3049–3057.
- [33] Bao, S. J.; Li, C. M.; Zang, J. F.; Cui, X. Q.; Qiao, Y.; Guo, J. New Nanostructured TiO<sub>2</sub> for Direct Electrochemistry and Glucose Sensor Applications. *Adv. Funct. Mater.* 18 (2008) 591–599.
- [34] Dai, Z.; Shao, G.; Hong, J.; Bao, J.; Shen, J. Immobilization and Direct Electrochemistry of Glucose Oxidase on a Tetragonal Pyramid-Shaped Porous ZnO Nanostructure for a Glucose Biosensor. *Biosens. Bioelectron.* 24 (2009) 1286–1291.
- [35] Zhao, C.; Shao, C.; Li, M.; Jiao, K. Flow-Injection Analysis of Glucose without Enzyme Based on Electrocatalytic Oxidation of Glucose at a Nickel Electrode. 71 (2007) 1769–1773.

- [36] Zhou, C.; Xu, L.; Song, J.; Xing, R.; Xu, S.; Liu, D.; Song, H. Ultrasensitive Non-Enzymatic Glucose Sensor Based on Three-Dimensional Network of ZnO-CuO Hierarchical Nanocomposites by Electrospinning. *Sci. Rep.* 4 (2014) 7382.
- [37] Zhang, L.; Li, H.; Ni, Y.; Li, J.; Liao, K.; Zhao, G. Electrochemistry Communications Porous Cuprous Oxide Microcubes for Non-Enzymatic Amperometric Hydrogen Peroxide and Glucose Sensing. *Electrochem. commun.* 11 (2009) 812–815.

## CHAPTER VI

### **Biocompatible Electronic Platform for Monitoring Protein-Drug Interactions and Proof-of-concept Theranostics**

#### **Highlights**

- ✚ Biocompatible electronic platform based on casein micelle to investigate its pH-responsive behavior through current-voltage ( $I$ - $V$ ) technique.
- ✚ *In vitro* demonstration of the interaction between casein micelle and cysteamine drug (protein-drug) interactions based on a solid-state device.
- ✚ Successful bioconjugation between casein micelle, cysteamine drug and amine functionalized barium titanate NPs confirmed through spectroscopic studies.
- ✚ Proof of concept theranostic platform to investigate the interaction between cysteine and cysteamine drug encapsulated in CAS carrier on a solid-state device.
- ✚ Investigated piezoelectric response of the bioconjugates with prospects in self-powered applications.

## 6.1. Introduction

Solid-state devices provide a beneficial platform for sensing potential biological molecules<sup>[1]</sup>. Nanomaterials, especially multifunctional nanoparticles used in constructing these devices provide a versatile platform for multiple applications<sup>[2]</sup>. When combined with biological components like proteins and polymers will open up new possibilities in constructing smart devices for biosensing and theranostics<sup>[3],[4]</sup>. Combining solid-state devices with biological components proves to have promising scope in nanomedicine, smart biosensing systems where the fundamental life sciences and advanced engineering applications are possible to converge<sup>[4],[5]</sup>. Such an interdisciplinary field of biological systems interface and solid-state electronic devices will be the future research trend in nanobiotechnology for advanced diagnostic as well as therapeutic applications<sup>[3],[6]</sup>. Stimuli-responsive and multifunctional materials serve to be promising systems for developing next-generation biomedical devices<sup>[7],[8],[9]</sup>. One such example is semiconducting nanomaterials used for biological applications such as sensing<sup>[10]</sup> and drug delivery. The prospect of nanomaterials in life sciences has a remarkable application, and such a nano-bio interface has its challenges and prevails to be at the proof-of-concept stage <sup>[11]</sup>

Casein, a major milk protein has been extensively studied for elucidating its structure<sup>[12],[13]</sup>, and for applications in drug delivery<sup>[14]</sup>, opaque coatings<sup>[15]</sup>, MRI contrast agents<sup>[16]</sup>, biosensing and as soft materials<sup>[17]</sup>. Casein micelles (CAS) have the potential to be vectors or carriers that can conjugate with the drug as well as nanoparticles,

rendering advantages in diagnostic and therapeutic applications<sup>[3,18]</sup>. Moreover, CAS has the potential to be a stimuli-responsive material<sup>[19]</sup>. Combining it with multifunctional nanomaterial like Barium titanate nanoparticles (BT NPs) will lead to potential application in diagnostics<sup>[20]</sup> as well as therapeutics since BT NP is a well known semiconducting (n-type)<sup>[21]</sup>, piezoelectric material<sup>[22]</sup>, biocompatible and exhibits Second Harmonic Generation (SHG)<sup>[23]</sup>, non-linear optical properties useful in imaging. Hence interaction between CAS and BT NPs together with a model drug will be a useful and interesting study in this field. Usually, a spectroscopic method is the most widely adopted one for finding the interactions between the nanoparticle, proteins, and drugs for conjugate confirmation<sup>[18]</sup>; a solid-state biocompatible electronic platform could be a substitute for such related studies. Realization of such multifunctional platform for transducing chemical or biological binding events into electrical signals suggests the potential for a highly sophisticated interface between nanoelectronics and biological information processing systems in the future<sup>[1]</sup>.

The present work is representative of such a novel concept where CAS based electronic platform (a solid-state device) serves as the tool for studying the interaction between the protein CAS and model drug cysteamine (CYST). The solid state configuration of metal-protein-metal electrical junctions, resembling the natural electron transfer (ET) process (biomimetic approach) has been adopted in this proposed work<sup>[24]</sup>. CAS also conjugates with amine functionalized Barium titanate nanoparticles (BT NPs) which renders possible use in imaging and stimuli-responsive applications. Agarose, a biopolymer which forms three-dimensional (3D) network serves as the suitable matrix

(substrate) for working with protein<sup>[25]</sup>. Its film-forming ability, stability, and inertness towards biomolecules, above all its property as an alternate electrode make it best suitable for our present study<sup>[26]</sup>. The binding events between the protein and drug/analyte are observed through significant change in current output. Finally, proof of concept theranostic application has been proposed in this work and demonstrated using cysteine (CYS) as the analyte. The conjugate CAS-CYST were responsive to CYS, as observed through a change in current value on a biocompatible electronic platform. Thus such an *in-vitro* platform can serve as a preliminary tool for investigating the possible interactions and opens application in theranostics before performing invasive real-time experiments. The proposed work opens up possibilities for utilizing such an *in-vitro* platform for investigating possible applications in theranostics as well as for constructing smart devices.

## **6.2. Experimental section**

### **6.2.1. BT NPs synthesis**

Tetragonal phase, BT NPs with random shape were synthesized by a conventional solid-state reaction method and the precursors used was 99.95% pure BaCO<sub>3</sub> (High Purity Chemicals) and 98% pureTiO<sub>2</sub> (Daejung Chemicals). An appropriate quantity of precursors according to the atomic ratio of BaTiO<sub>3</sub> was ground well in a pestle and mortar for 30 min using acetone. This homogeneous mixture was placed in an open-tube furnace and heated to 1,200°C at the rate of 2.5°C/min, for two hours<sup>[21]</sup>. Once the process completed, the BT NPs were taken out and cooled.

### **6.2.2. Functionalization of BT NPs with NH<sub>2</sub> group**

Functionalization of Barium titanate nanoparticles with amine group was carried out by a two-step process as reported in our previous work. Firstly, it is decorated with OH groups and then later functionalized with NH<sub>2</sub> groups using (3-aminopropyl) triethoxysilane (APTES) as the source. Barium titanate nanoparticles (120 mg) were treated with 1M nitric acid for two hours and then washed until it attains neutral pH. Further, these NPs were treated overnight with H<sub>2</sub>O<sub>2</sub> which results in hydroxylation of BT NPs (BT-OH), and this product is treated with 140 μL of APTES, 250 μL ammonium solution, and 36 mL of anhydrous ethanol and heated at 70°C for 8 h<sup>[20],[52]</sup>. The sample was washed three times with ethanol to remove unwanted reactants and later dried and stored in a vacuum environment.

### **6.2.3. Casein micelle preparation**

The Critical Micellar Concentration of Casein is 1 mg/ml. The stock solution (5 mg/ml) was prepared in such a way that even the lowest working dilution will have a concentration of casein above 1mg/ml. CAS was prepared by adding the appropriate quantity of casein powder to 0.01M PBS and stirring it for 1 hour. It was then refrigerated at least for 2 hours before use<sup>[18]</sup>. The upper layer contained casein micelles.

### **6.2.4. Preparation of Cysteamine (CYST) drug solution**

A stock solution of drug was prepared by dissolving 250 mg of CYST in 1ml of 0.1M PBS buffer.

### **6.2.5. Preparation of conjugates**

The bioconjugates were prepared by adding the appropriate amount of individual components (stock solution) and stirring for 1 hour at room temperature. The ratio of CAS: CYST: BT is 1:5:0.2 which is by literature. The as-prepared bioconjugates were stored in the refrigerator. The schematic representation of the bioconjugate is given in Figure 6.1.

#### **6.2.6. Fabrication of CAS film based devices**

CAS and its conjugates based devices for pH stimuli, protein-drug interactions, and proof-of-concept theranostic studies through *I-V* studies were fabricated using agarose as the matrix. 0.5% of agarose solution was used as the matrix for fabricating devices. The appropriate quantity of agarose mixed in 0.01M PBS (phosphate buffer solution), was microwaved for 1 min to obtain a clear solution. 1:1 ratio of agarose: conjugates solution (or CAS solution) was taken, mixed well and drop cast onto a clean glass slide and allowed for drying at 37°C overnight. The as-fabricated device area is 1.5×1.5 cm.

#### **6.2.7. Fabrication of PNGs (Piezoelectric Nanogenerators)**

CAS and CAS-BT film-based piezoelectric nanogenerators were fabricated in a facile fashion involving three simple steps: CAS/CAS-BT film formation, the establishment of electrodes and external connections, and fixation within a Kapton frame. The film formation process was similar to the one mentioned in experimental section 2.6. The ITO-coated PET film served as a conducting electrode (bottom) as well as a substrate for the film whereas the Aluminum (Al) foil (thickness, ~15 μm) positioned on the top of the film served as the counter-electrode (top). External connections were established using Copper (Cu) wires by attaching to the top and bottom electrodes with a silver (Ag)

paste and were used to measure the piezoelectric output voltage and current. The final step is to fix the device tightly between two Kapton films as supporting frames to establish firm contact between the electrode and the active area (film). The active area of the as-fabricated device was  $1.5 \times 1.5$  cm. The PNG devices were poled by applying an electric field of 1 kV for ~1 h to enhance its piezoelectric properties.

#### **6.2.8. Instrumentation**

FE-SEM (JSM-6700F; JEOL) was used for surface morphological studies. The crystallinity and phase of the pristine, as well as amine functionalized BT NPs were analyzed through X-ray diffractometer (Rigaku), operated at room temperature (40 kV/10 mA; Cu K $\alpha$  radiation). For Raman analysis, an excitation source of 514 nm and a single-stage spectrometer (Lab RAM; HR Evaluation, Japan) were used. The electrical outputs of PNGs were recorded using Keithley nanovoltmeter (2182A) and picoammeter (6485). The PNGs output was measured by triggering with a mechanical load ( $F = 0.2$  N). The successful conjugation was confirmed using Fourier-transform infrared spectroscopy (FTIR, Nicolet 6700, Thermo Scientific).

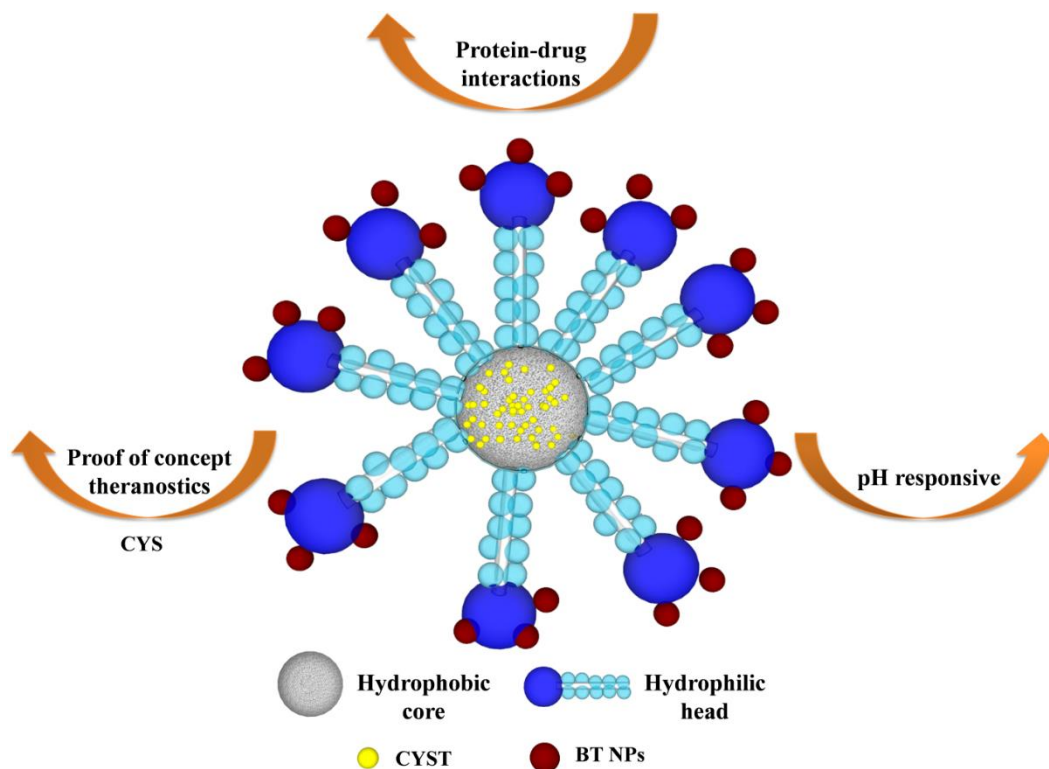


**Figure 6.1.** Schematic representation of CAS-CYST-BT conjugate and overview of the proposed work.

### 6.3. Results and discussion

#### 6.3.1. Structural characterization and spectroscopic confirmation of bioconjugate formation

Among the different spectroscopic methods that can efficiently characterize protein structures, Raman spectroscopy has the potential to identify even ensemble of structures compared to single conformation. The globular structure of CAS is evident from the amide I band around  $1667\text{ cm}^{-1}$  (Figure 6.2a). The predominant protein

secondary structures of CAS are  $\beta$ -sheets as evident from the  $1667\text{ cm}^{-1}$  peak corresponding to C=O stretching vibrations<sup>[27]</sup>. Further, the  $1240\text{ cm}^{-1}$  peak represents amide III band as well as contributions from  $\beta$ -sheets. The peaks around  $1210\text{ cm}^{-1}$  and  $1615\text{ cm}^{-1}$  corresponds to tyrosine band whereas  $1326\text{ cm}^{-1}$  and  $1452\text{ cm}^{-1}$  corresponds to  $\text{CH}_2$  and  $\text{CH}_3$  deformations respectively<sup>[28]</sup>. The  $2575\text{ cm}^{-1}$  peak represents the  $-\text{SH}$  group in CYST, the  $\text{CH}_2$  stretching vibrations could be observed in the region between  $2850\text{--}2950\text{ cm}^{-1}$  and the Trans conformation of CYST is evident from the  $763\text{ cm}^{-1}$  peak<sup>[29-31]</sup>. The characteristic peaks of BT NPs at  $305\text{ cm}^{-1}$  and  $518\text{ cm}^{-1}$  confirm the tetragonal phase of the nanoparticle (Figure 6.2a)<sup>[32]</sup>. Moreover, the tetragonal phase of pristine as well as  $\text{NH}_2$  functionalized BT NPs are evident from the peak splitting at  $45^\circ$  ( $200/002$ ) as shown in XRD spectra (Figure 6.3; ICDD 98-001-3771 pattern). In the final conjugate (CAS-CYST-BT), the presence of individual component peaks, as well as that of conjugation, confirms the successful conjugation between them all. The amide I and amide III bands (peaks) are conserved even in the conjugates, and thus the CAS protein conformation remains unaltered. The characteristic C-S bond of CYST has been shifted to lower wavenumber appearing at  $643\text{ cm}^{-1}$ . This shift is due to the withdrawal of electron density from the C-S bond due to the bonding between sulfur and CAS<sup>[29]</sup>. Thus the Raman studies confirm the successful conjugation between all the components.

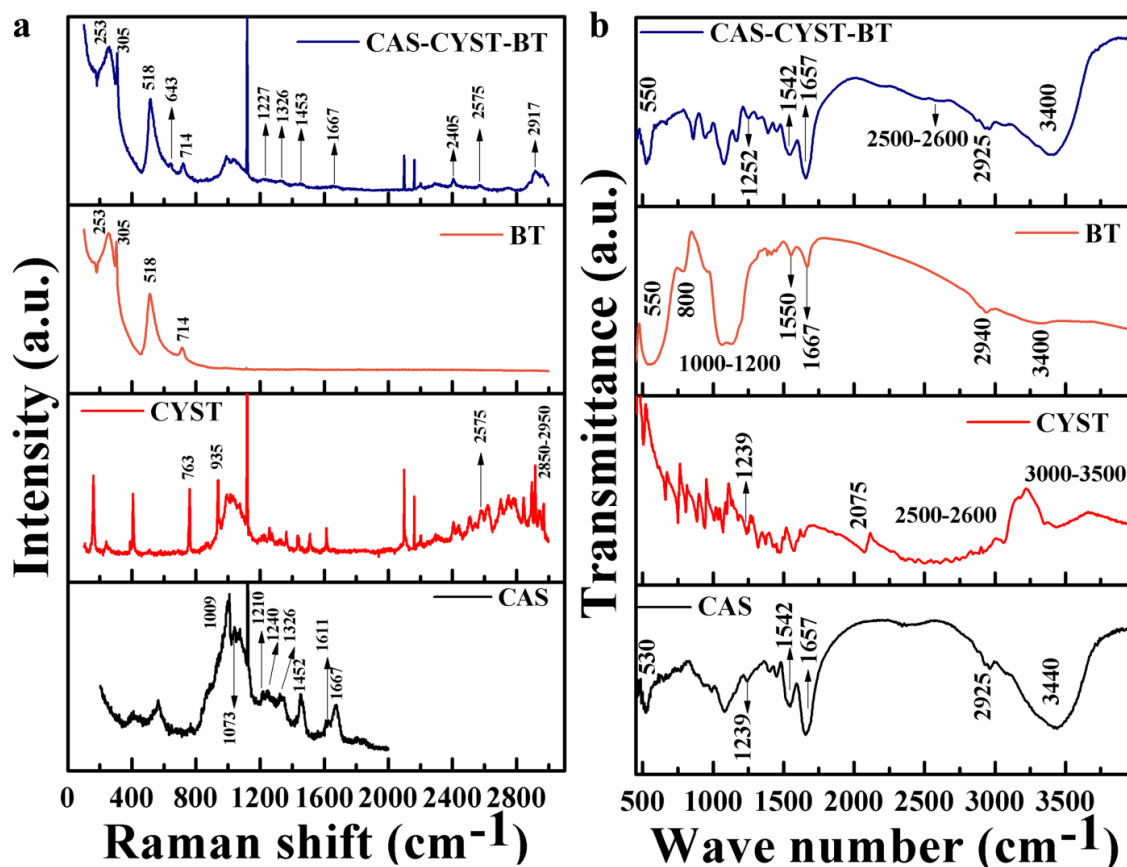


**Figure 6.2.** 514 nm excited Raman spectra (a) and FTIR spectra (b) of pristine (CAS, CYST, BT) and their conjugate (CAS-CYST-BT).

FTIR spectrum of pristine and conjugates reveal the structure as well as the conjugation between them (Figure 6.2b and Figure 6.4b). CAS micelles show amide I, amide II and amide III bands at  $1657\text{ cm}^{-1}$ ,  $1542\text{ cm}^{-1}$ , and  $530\text{ cm}^{-1}$  respectively<sup>[33]</sup>. The change in the peak position and intensity in bioconjugates compared to pristine CAS confirms the formation of conjugates. The peak at  $1230\text{ cm}^{-1}$  represents the C-N stretching vibrations and stretching of  $-\text{CH}_2-\text{CH}_3-$  group, is evident from  $2925\text{ cm}^{-1}$  peak;

-OH group's stretching vibrations could be observed at  $3440\text{ cm}^{-1}$  [16,34]. In case of the drug CYST, S-H stretching vibration is evident from peaks observed in between  $2500 - 2600\text{ cm}^{-1}$  [35]. Peaks at  $1239\text{ cm}^{-1}$  and  $2075\text{ cm}^{-1}$  are characteristic of C-N stretching mode [36]. For the amine functionalized BT NPs, signature peaks could be observed at  $550\text{ cm}^{-1}$ ,  $1550\text{ cm}^{-1}$  and  $3400\text{ cm}^{-1}$  corresponding to metal oxide stretching vibration, primary amine bending and -OH group stretching respectively. The double peak between  $1000\text{ cm}^{-1}$  and  $1200\text{ cm}^{-1}$  as well as the peaks at  $800\text{ cm}^{-1}$  and  $2940\text{ cm}^{-1}$  confirms the successful amine functionalization using (3-aminopropyl) triethoxysilane (APTES) molecule [20]. For the final conjugate of CAS-CYST-BT, signature peaks of individual components and their conjugation is well evident from the peaks observed. The CAS globular structure in the conjugate remains conserved without any disruption as could be observed from the unaltered amide I and amide II peaks at  $1657\text{ cm}^{-1}$  and  $1542\text{ cm}^{-1}$  respectively. The presence of S-H stretching vibrations in between  $2500\text{ cm}^{-1} - 2600\text{ cm}^{-1}$  and Ti-O bond stretching around  $550\text{ cm}^{-1}$  confirms the successful conjugation between all three components. The reduced intensity of S-H stretching vibration at  $2600-2500\text{ cm}^{-1}$  as observed for the conjugate suggests that -SH in cysteamine is covalently bound to CAS [35].

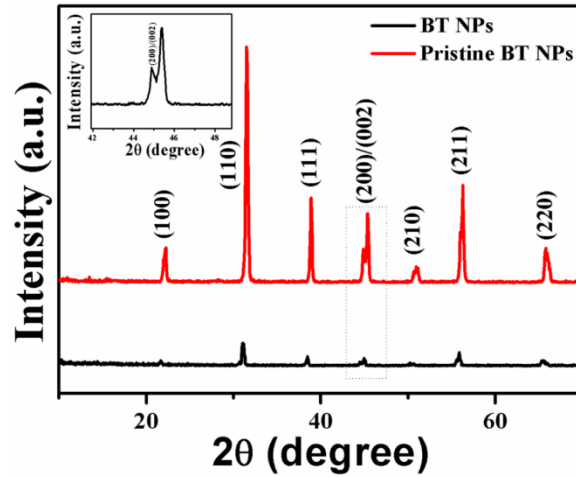


**Figure 6.3.** XRD spectra of pristine and  $\text{NH}_2$  functionalized BT NPs.

Moreover, the shift in C-N stretching vibrations from  $1239\text{ cm}^{-1}$  to  $1252\text{ cm}^{-1}$  confirms the interaction between CAS and CYST drug whereas no such interaction was observed between CAS and BT NPs (Figure 6.4b). More  $-\text{NH}_2$  exposed onto CAS is evident from the much narrower band at  $3400\text{ cm}^{-1}$ <sup>[35]</sup>. These confirm the electrostatic interaction existing between the CAS and BT NPs.

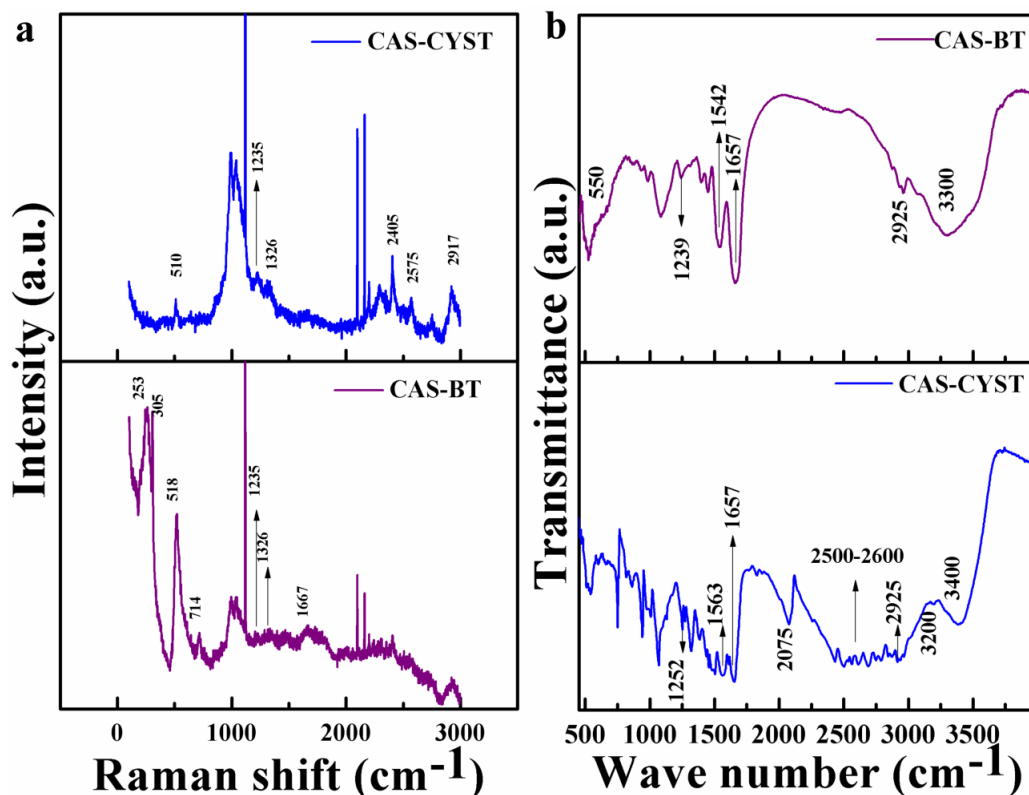


**Figure 6.4.** 514 nm excited Raman spectra (a) and FTIR spectra (b) of CAS-BT and CAS-CYST conjugates.

Further to confirm the interaction of CYST and BT with CAS individually, UV spectroscopic studies were undertaken (Figure 6.5). The 277 nm peak is the characteristic peak of CAS, and there is no shift in the peak for CAS-BT conjugates suggesting the electrostatic interaction between them. Moreover, successful conjugation between CAS and BT is evident from the presence of BT NPs characteristic peak at 568 nm. Whereas for CAS-CYST conjugates there is a slight red shift from 277 nm to 281 nm (CAS) confirming the complex formation between CAS and CYST. CYST

conjugates with the hydrophobic region of CAS.

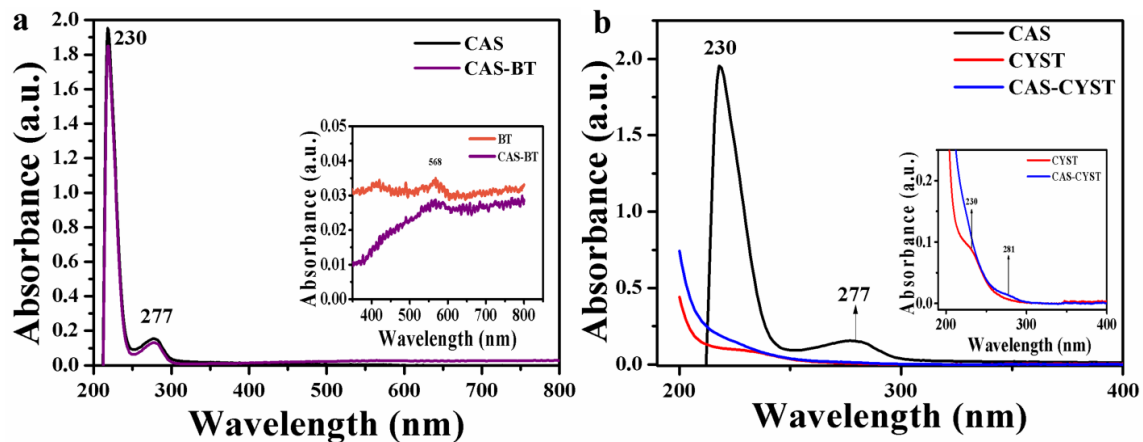


**Figure 6.5.** Absorbance spectra of (a) CAS, BT (inset) and their conjugate CAS-BT (b) CAS, CYST, and their conjugate CAS-CYST (200-800 nm range).

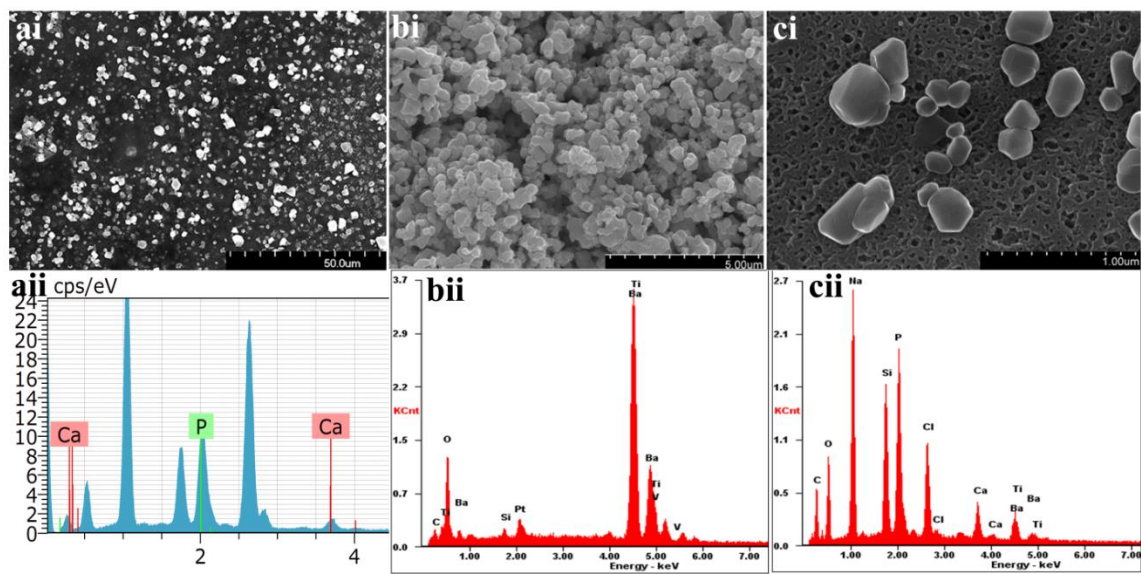


**Figure 6.6.** FESEM micrographs and corresponding EDAX spectrum of (a) CAS, (b) BT, (c) CAS-BT.

These conclusions support the FTIR and Raman results confirming successful bio conjugation between all the three individual components. FESEM micrographs of CAS, BT, CAS-BT and their corresponding EDAX profile once again confirms their successful conjugation and absence of other impurities (Figure 6.6).

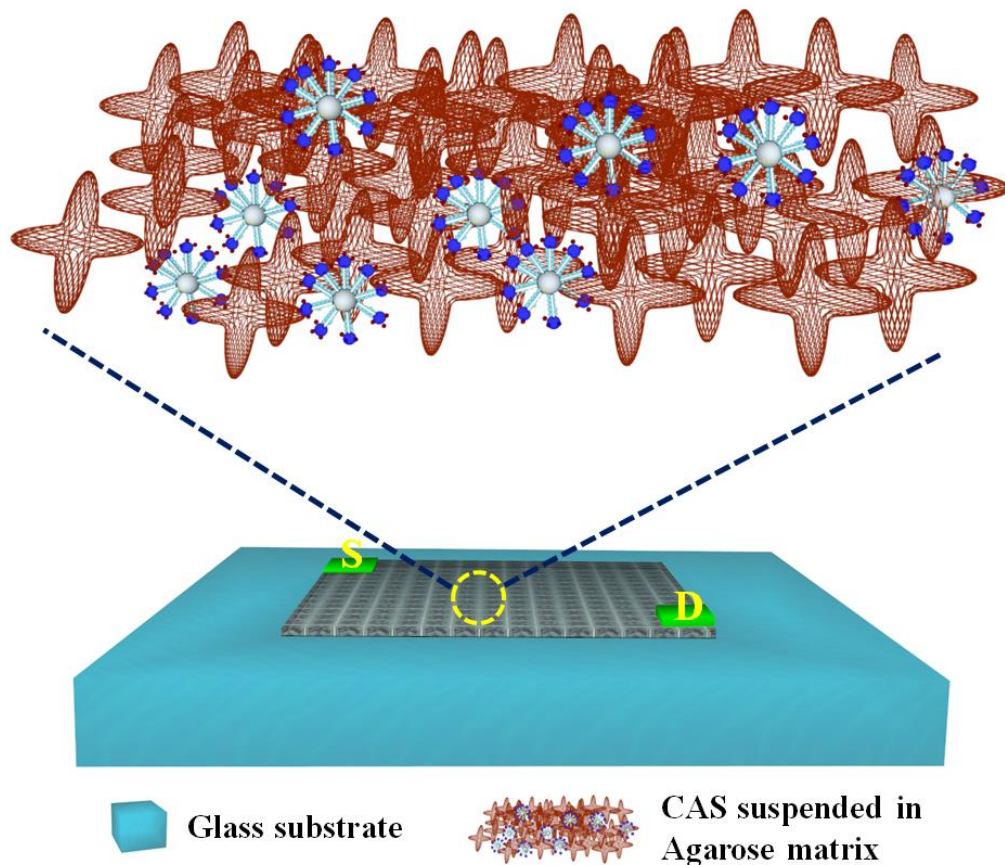


**Figure 6.7.** The schematic representation of the device structure.

### 6.3.2. pH stimuli-responsive studies

The response of the CAS and CAS-BT conjugate to external stimuli like pH were studied using an  $I$ - $V$  technique through a solid-state device with metal-protein-metal configuration (Figure 6.7). The  $I$ - $V$  characteristic curves of CAS and CAS-BT based devices in response to different pH values (pH7 to pH1) were investigated within a potential window of  $\pm 4$ V. The current response of CAS film-based sensor device has a monotonic functional relationship with continuous drop in pH value from 7 to 1.

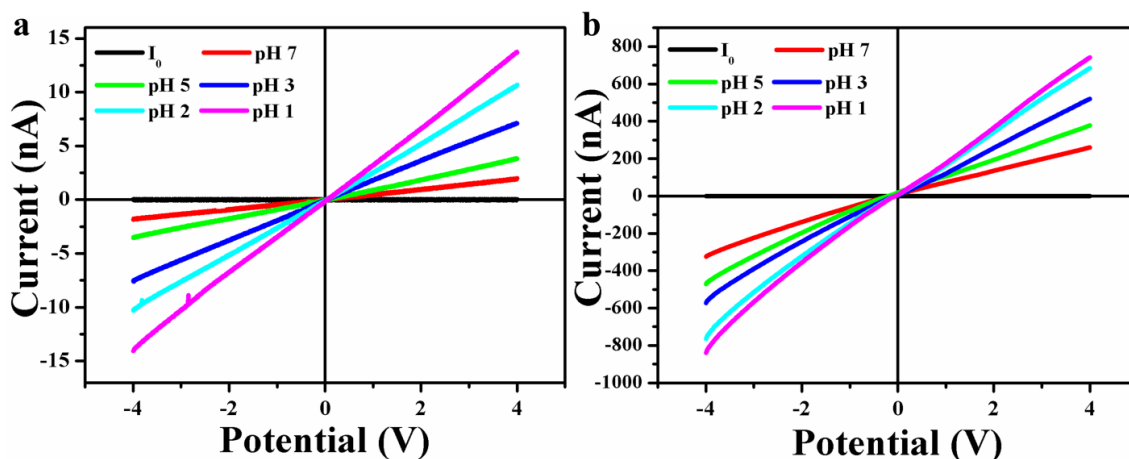


**Figure 6.8.**  $I$ - $V$  studies for pH stimuli.  $I$ - $V$  curves of (a) CAS and (b) CAS-BT film based devices in response to pH stimuli (range: pH7 to pH1).

Initially, when exposed to PBS buffer of neutral pH, there is a slight change in conductance of the device from its initial state due to the interaction of  $H^+$  and  $OH^-$  ions with the film surface (amphoteric nature)<sup>[37–39]</sup>. With the drop in pH from 7 to 1, the concentration of  $H^+$  ion increases and thus the conductance of the device increases as evident from the increase in the current value at the positive potential as shown in Figure

6.8a (+ 4V)<sup>[40]</sup>. Similar behavior could be observed for CAS-BT film-based sensor also with the exception that it has enhanced current response (Figure 6.8b) compared to the CAS film based device. This enhancement is contributed from the interaction of BT NPs having Lewis base site (R-NH<sub>2</sub>) with H<sup>+</sup> ions (Lewis acid) resulting in the release of electrons thus increased current value<sup>[37,41,42]</sup>. The *I-V* curves (at any pH value) exhibit good linear behavior proving an ohmic contact. Thus, conjugation of BT NPs with CAS does not deprive its stimuli-responsive behavior but rather enhances the property (Figure 6.9).

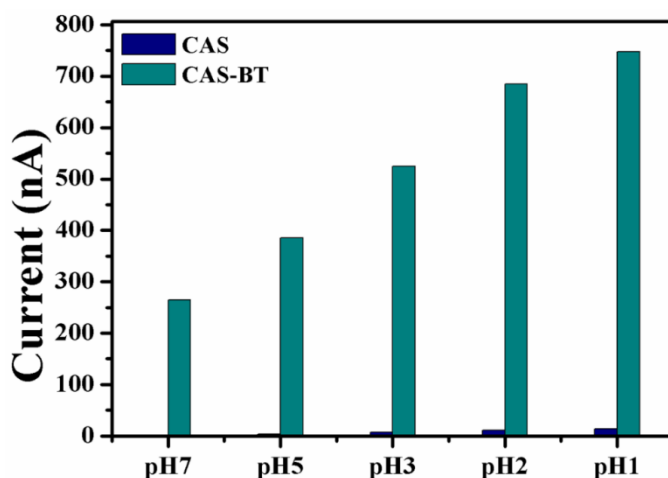


**Figure 6.9.** Comparison between CAS and CAS-BT film based devices' current response to pH stimuli (range: pH7 to pH1; @ +4V).

Conjugation with BT NPs will be advantageous in case of bioimaging applications as BT NPs are known to exhibit non-linear optical properties such as Second Harmonic Generation (SHG). This pH-responsive behavior of CAS<sup>[39]</sup> and CAS-BT conjugates confirmed through *I-V* technique may further pave the way for

smart/stimuli-responsive applications such as in biosensing, drug delivery, and theranostics. These results prompted us to use this device as a biocompatible platform for studying protein-drug interactions and proof of concept theranostic application.

### 6.3.3. Protein-drug interactions through *I-V* characteristics

The protein-drug interaction (i.e., the interaction between CAS and CYST) was analyzed through an *I-V* technique. The CAS film based device serves as the sensor platform for studying the interaction. As evident from Figure 6.10a, the device exhibits an ohmic type of behavior even in the presence of different concentrations of CYST drug (100 mg to 600 mg; normal dosage)<sup>[43]</sup>.

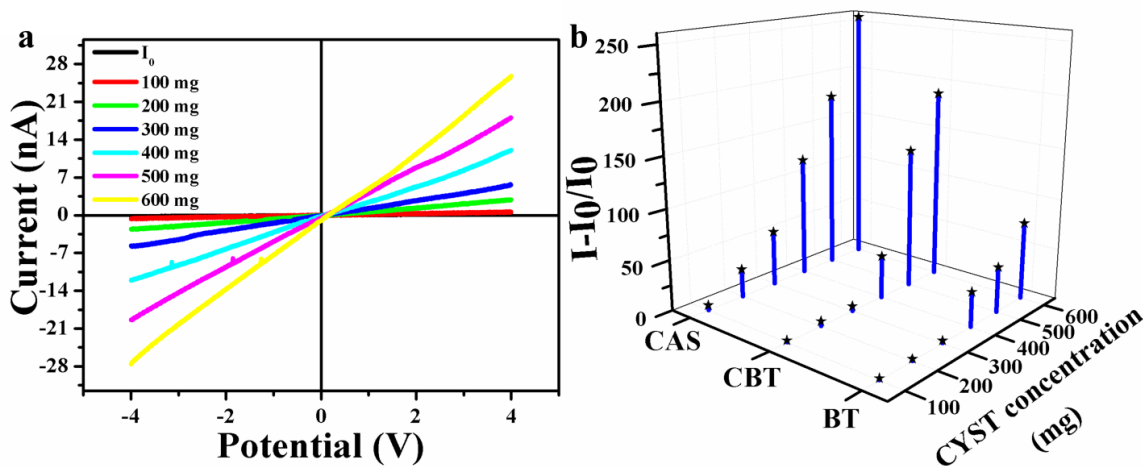


**Figure 6.10. *I-V* studies for protein-drug interaction.** (a) *I-V* curves of CAS film based device in response to different CYST drug concentration (100mg to 600mg). (b) Three-dimensional (3D) graphical representation of the response of CAS, CAS-BT

(CBT) and BT film based devices to different CYST drug concentration (100mg to 600mg) [relative change in current is denoted as  $(I-I_0/I_0)$ ].

CYST is positively charged at our experimental condition (pH 7) as its pI is around 8.2 to 8.6. Whereas, CAS is negatively charged at given experimental condition with micelle structure having hydrophilic outer surface and a hydrophobic core<sup>[14,33]</sup>. The CYST drug can conjugate with the hydrophobic core of the CAS micelles and thus can change the surface charge properties of the film and thereby reducing the resistance of the film<sup>[8]</sup>. With an increase in CYST concentration, the conductance of the sensor device increases in a monotonic functional relationship as evident from the increase in current response at the positive potential (+4V) (Figure 6.11a).

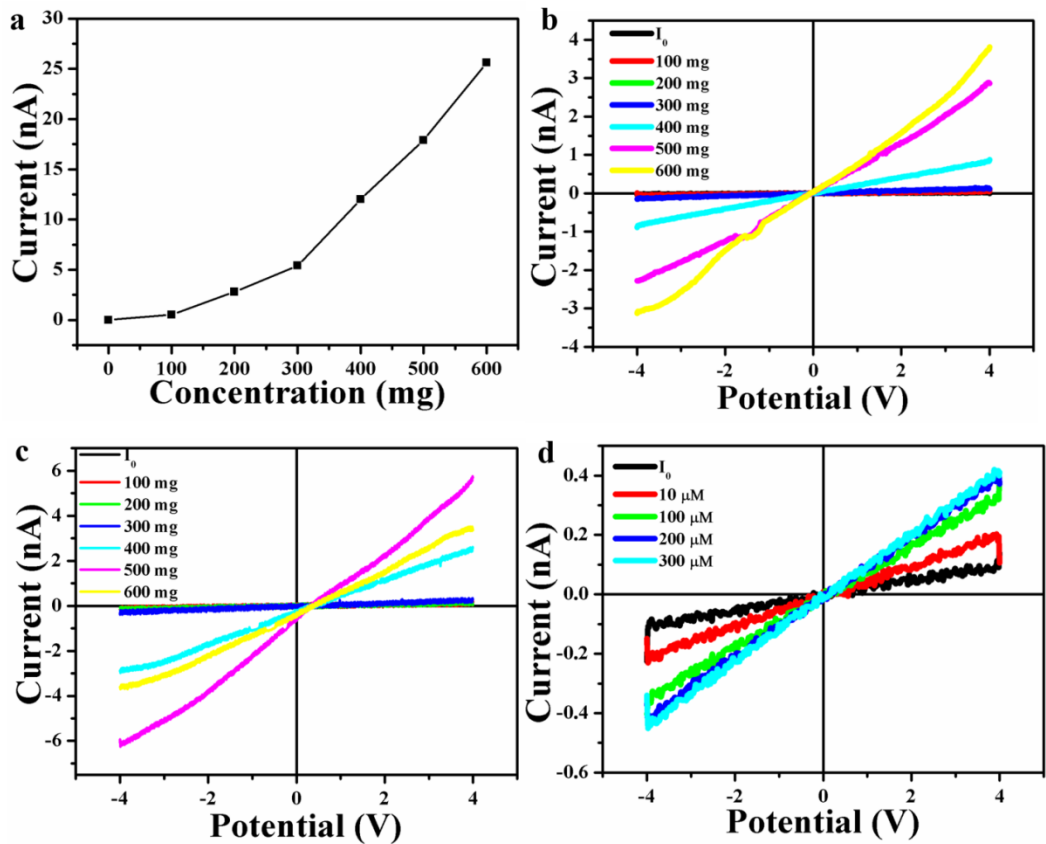


**Figure 6.11.** (a) The calibration curve obtained from figure 5a shows the monotonic functional relationship between CYST drug concentration and output current (current response of the device at +4V). (b)  $I$ - $V$  curves of the CAS-BT film based device in response to various CYST drug concentration (100 mg to 600 mg). (c)  $I$ - $V$  curves of the BT film based device in response to various CYST drug concentration (100 mg to 600 mg). (d)  $I$ - $V$  curves of the CAS-BT film based device showing no response to various concentrations of CYC (10  $\mu$ M to 300  $\mu$ M; physiological range).

There is no deviation from the ohmic behavior of the device even with the increase in CYST drug concentration. *I-V* curves confirm the conjugation between CAS and CYST which is in confirmation with the FTIR, Raman and UV analysis. A similar study was performed for CAS-BT and BT film based devices respectively and as expected their response to CYST was less compared to pristine CAS (Figure 6.11 b,c, and Figure 6.10b). Thus, there is a significant interaction between CAS and CYST, and BT NPs have no interaction with the drug in the concentration range from 100 mg to 300 mg; usual dosage level (Figure 6.11 b,c). Therefore, it is possible to harness the BT NPs conjugated to CAS to have additional functions such as imaging or targeting without hampering the interaction between CAS and drug. These results further paved the way for utilizing such a device platform for analyzing proof-of-concept theranostic applications.

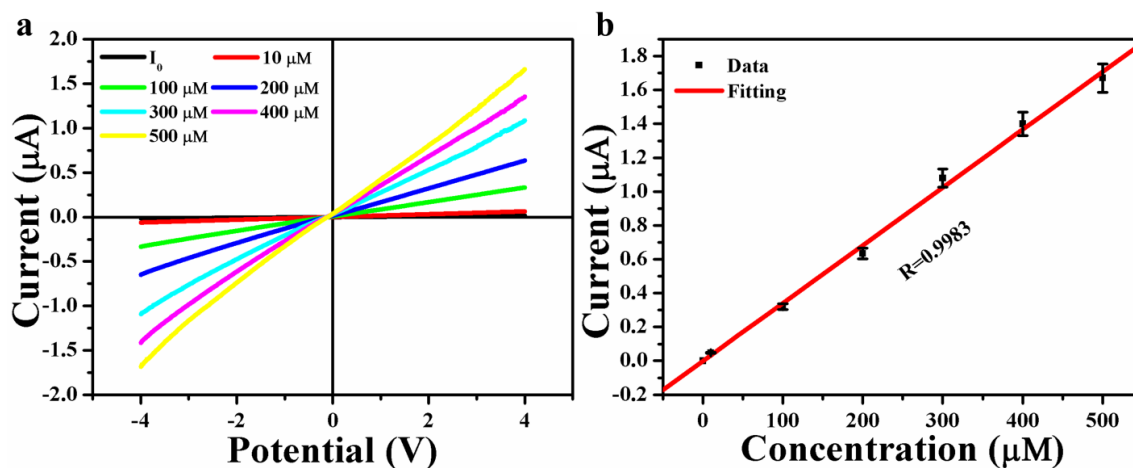


**Figure 6.12. Proof of concept theranostic platform:** (a) *I-V* curve of CAS-CYST film based device in response to different CYS concentrations (10 $\mu\text{M}$  to 500 $\mu\text{M}$ ). (b) The

current response of the device at -4V for different CYS concentrations (10 $\mu$ M to 500 $\mu$ M) (calibration plot obtained from *I-V* curves).

#### **6.3.4. Proof of concept theranostic platform**

CYST is a drug originally used for depleting cystine and treating cystinosis but has potential in treating neurodegenerative as well as cancers [43,44]. In this present study, the interaction between the target analyte (CYS) and the drug which is encapsulated inside the carrier (CAS) on an *in vitro* platform is studied for proof of concept theranostic applications. The successful interaction between the drug and CYS is well evident from the current response obtained through *I-V* curves. The interaction between CYST (drug) and CYS (analyte) has been well reported through the cystine depleting mechanism where the drug CYST forms a disulfide bond with CYS through cystine disulfide reduction. The CAS serves as the carrier for the drug CYST which has good interactions with CYS (target). CYS is negatively charged at the given pH in our experimental condition (pH- 7)<sup>[20]</sup> as well evident from its isoelectric point (pI - 5.07). CYS is one such amino acid having the role as electron transfer carrier/ mediator in biological systems and also known to exhibit proton-coupled electron transfer reactions<sup>[45]</sup>. Moreover, under physiological conditions, the sulfhydryl group of CYS undergoes partial deprotonation and thus becomes highly reactive<sup>[46]</sup>. CYS forms a disulfide bond with CYST through an oxidation process, and thus the electrons released increases the charge carrier density leading to increased current output (Figure 6.13). Hence when CYS concentration increases there is a corresponding increase in the current output obtained through *I-V* curves as shown in Figure 6.12a. There is a linear relationship



### **6.3.5. Piezoelectric response of PNGs for self-powered applications**

The ability of the material to produce electrical energy in response to a mechanical force (piezoelectricity) will render prospects in self-powered applications. BT NPs are well known for their piezoelectric property. If the combination of BT NPs with carriers like CAS micelle results in enhanced piezoelectric effect they can be applied in smart self-powered implantable devices for sensing or drug delivery applications<sup>[49-51]</sup>. Such multifunctional properties like sensing and energy harvesting will result in smart battery-less devices optimum for implantable devices. With such prospects, a piezoelectric nanogenerator was fabricated using CAS and CAS-BT film.

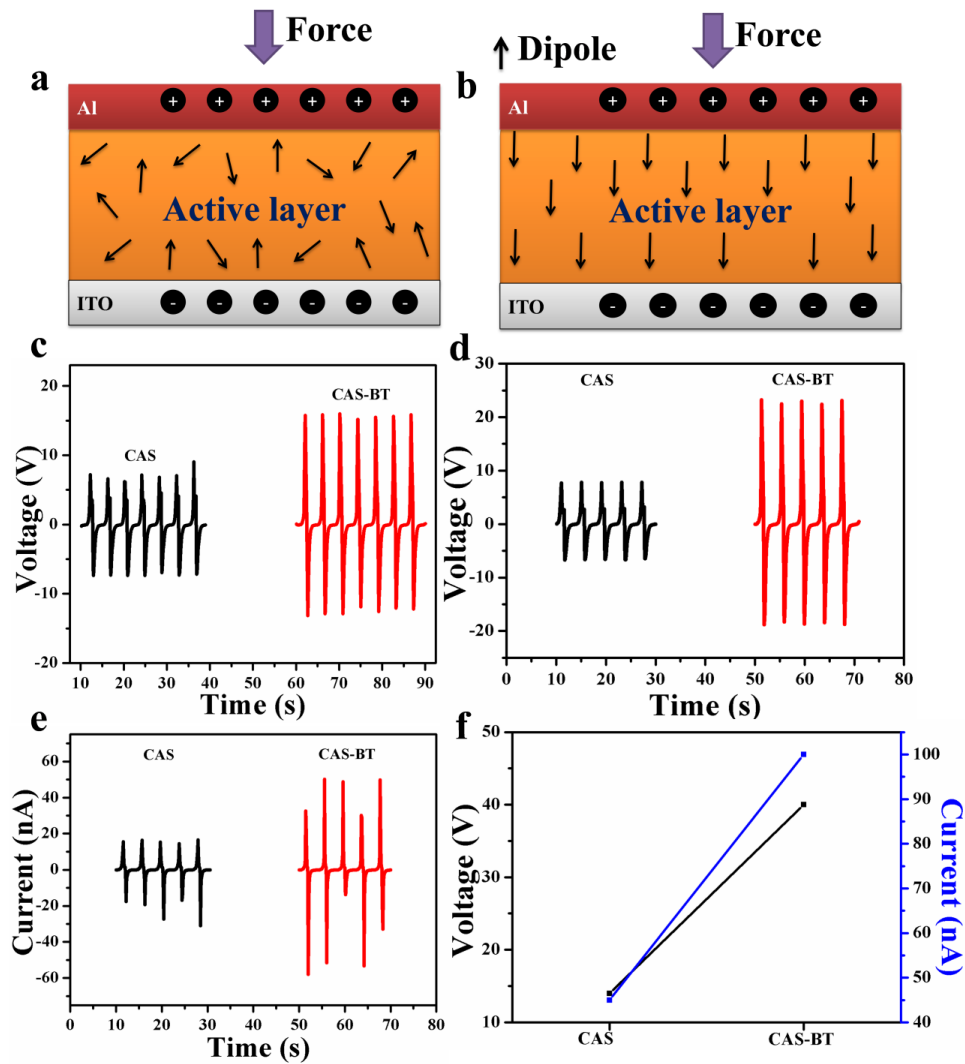


**Figure 6.14. Piezoelectric response of CAS and CAS-BT film based PNGs with prospects in self-powered applications:** Schematic representation of working mechanism of PNG (a) before and (b) after poling. Open circuit voltage ( $V_{oc}$ ) of PNGs (c) before and (d) after poling (Force = 2N). (e) Short circuit current ( $I_{sc}$ ) of PNGs after poling at an applied force of 2N. (f) Comparative graph depicting the output voltage and current of PNGs at a mechanical load of 2N.

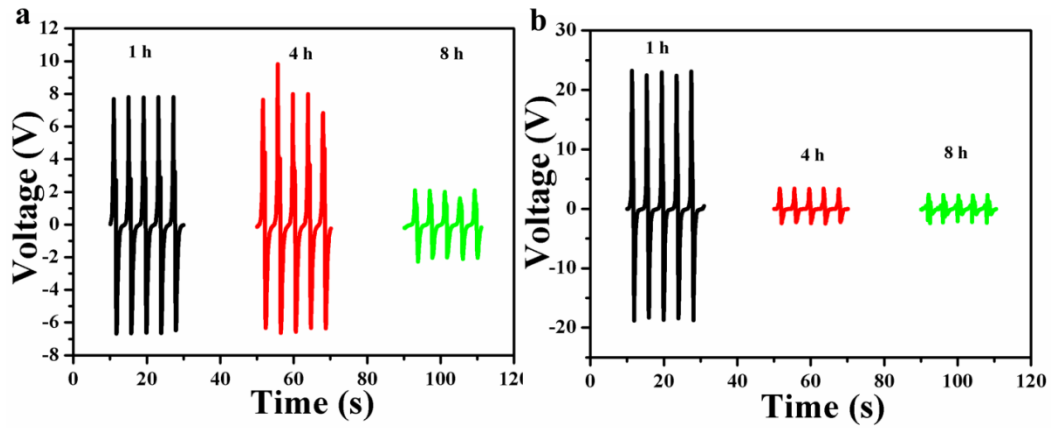


**Figure 6.15. Effect of electrical poling time:** Open circuit voltage ( $V_{oc}$ ) of CAS (a) and CAS-BT (b) film based PNGs at different poling period (time) at an electric field of 1kV (at a mechanical load of  $F = 0.2$  N).

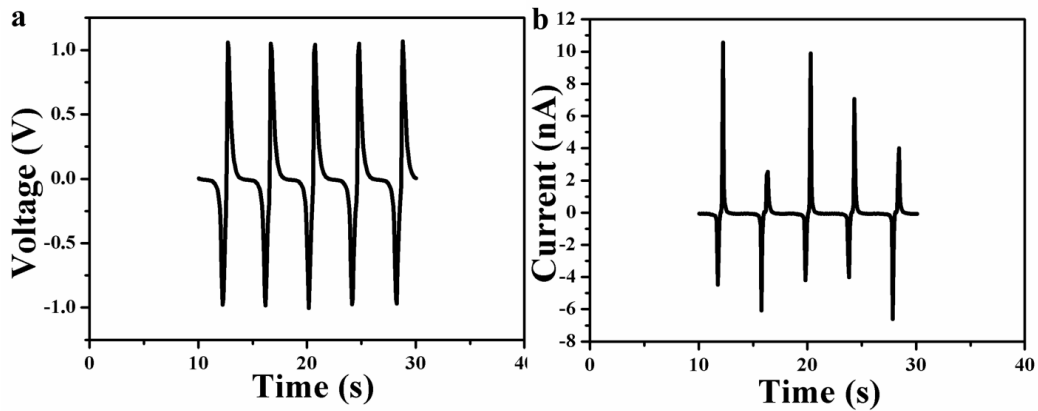


**Figure 6.16. Polarity switching test.** (a) Open circuit voltage ( $V_{oc}$ ) and (b) Short circuit current ( $I_{sc}$ ) of CAS-BT film based PNG during reverse connection (at a mechanical load of  $F = 0.2$  N).

Detailed fabrication procedure is given in experimental section, and its schematics is shown in Figure 6.14 a,b. Before electrical poling of the device, the

dipoles are not oriented (Figure 6.14 a) and thus the piezoelectric response of the device will be less compared to poled ones (Figure 6.14 c). Whereas, after poling the device at an optimized condition by applying an electric field of 1KV for 1hr, the dipoles are aligned properly (Figure 6.14b) and results in enhanced piezoelectric response compared to unpoled ones (Figure 6.14d). The average peak-to-peak open circuit voltage ( $V_{oc}$ ) of CAS-BT film based PNG before poling is  $\sim 30V$  and after poling it is enhanced to  $\sim 40V$ . Poling conditions were optimized as shown in Figure 6.15 where poling beyond 1hr causes depolarization (disorientation of dipoles). The average peak-to-peak short circuit current  $I_{sc}$  of CAS and CAS-BT film based PNG is  $\sim 45$  nA and 100 nA as shown in Figure 6.14e. A comparison between the current and voltage profile of CAS and CAS-BT film based PNG is depicted in Figure 6.14f. Polarity switching of the CAS-BT film based PNG is given in Figure 6.16, which confirms that the output is from the device and not from an external source. The piezoelectric response of these bioconjugates based devices will lead to the realization of self-powered systems finding potential application in biosensing and implantable devices.

#### **6.4. Conclusions**

In summary, we have demonstrated a biocompatible electronic platform based on CAS to investigate its response to pH and drug using a current-voltage ( $I$ - $V$ ) technique. The interaction between casein and CYST (protein-drug interactions) were studied *in vitro* on a solid-state device configuration and confirmed with spectroscopic studies. The successful conjugation between CAS, cysteamine (CYST; model drug), and amine functionalized Barium titanate nanoparticles (BT NPs) confirmed through current-

voltage ( $I$ - $V$ ) technique complies well with the spectroscopic results. The stimuli-responsive behavior of CAS and CAS-BT in pH range of 7 to 1 were also analyzed. These findings further motivated us to carry out proof of concept theranostic analysis on this electronic platform to investigate the interaction between CYS and CYST drug (100 mg to 600 mg; normal dosage) encapsulated in a carrier (CAS). Further, the piezoelectric response of the bioconjugates was investigated for prospects in self-powered applications using a piezoelectric nanogenerator (PNG). This proposed work serves to be a novel, preliminary tool for investigating the possible interactions and application in theranostics before performing invasive real-time experiments. Moreover, it leads to the realization of a multifunctional platform for transducing chemical or biological binding events into electrical signals with the potential for a highly sophisticated interface between nanoelectronics and biological information processing systems in the future.

## References

- [1] N. Sun, Y. Liu, L. Qin, G. Xu, D. Ham, *Eur. Solid-State Circuits Conf.* **2012**, 14.
- [2] B. Y. S. Kim, J. T. Rutka, W. C. W. Chan, *N. Engl. J. Med.* **2010**, 363, 2434.
- [3] M. Espinoza-Castañeda, A. de la Escosura-Muñiz, G. González-Ortiz, S. M. Martín-Orúe, J. F. Pérez, A. Merkoçi, *Biosens. Bioelectron.* **2013**, 40, 271.
- [4] K. K. Ng, J. F. Lovell, G. Zheng, *Acc. Chem. Res.* **2011**, 44, 1105.
- [5] A. E. Nel, L. Mädler, D. Velegol, T. Xia, E. M. V. Hoek, P. Somasundaran, F.

- Klaessig, V. Castranova, M. Thompson, *Nat. Mater.* **2009**, 8, 543.
- [6] Z. Zhang, C. Liu, J. Bai, C. Wu, Y. Xiao, Y. Li, J. Zheng, R. Yang, W. Tan, *ACS Appl. Mater. Interfaces* **2015**, 7, 6211.
- [7] A. K. Shalek, J. T. Gaubblomme, L. Wang, N. Yosef, N. Chevrier, M. S. Andersen, J. T. Robinson, N. Pochet, D. Neuberg, R. S. Gertner, I. Amit, J. R. Brown, N. Hacoen, A. Regev, C. J. Wu, H. Park, *Nano Lett.* **2012**, 12, 6498.
- [8] Y. Cui, Q. Wei, P. Park, C. M. Lieber, H. Park, *Science (80-. )*. **2001**, 293, 1289.
- [9] M. A. C. Stuart, W. T. S. Huck, J. Genzer, M. Müller, C. Ober, M. Stamm, G. B. Sukhorukov, I. Szleifer, V. V. Tsukruk, M. Urban, F. Winnik, S. Zauscher, I. Luzinov, S. Minko, *Nat. Mater.* **2010**, 9, 101.
- [10] A. Manuscript, **2010**.
- [11] R. Elnathan, M. Kwiat, F. Patolsky, N. H. Voelcker, *Nano Today* **2014**, 9, 172.
- [12] R. W. Noble, D. F. Waugh, *J. Am. Chem. Soc.* **1965**, 87, 2236.
- [13] D. F. Waugh, R. W. Noble, *J. Am. Chem. Soc.* **1965**, 87, 2246.
- [14] A. Sahu, N. Kasoju, U. Bora, *Biomacromolecules* **2008**, 9, 2905.
- [15] F. Zhang, J. Ma, Q. Xu, J. Zhou, D. Simion, G. Carmen, J. Wang, Y. Li, *ACS Appl. Mater. Interfaces* **2016**, 8, 11739.
- [16] J. Huang, L. Wang, R. Lin, A. Y. Wang, L. Yang, M. Kuang, W. Qian, H. Mao,

- ACS - Appl. Mater. interfaces* **2013**, *5*, 4632.
- [17] R. Mezzenga, P. Schurtenberger, A. Burbidge, M. Michel, *Nat. Mater.* **2005**, *4*, 729.
- [18] Y. Liu, R. Guo, *J. Colloid Interface Sci.* **2009**, *332*, 265.
- [19] N. Kamiya, Y. Shiotari, M. Tokunaga, H. Matsunaga, H. Yamanouchi, K. Nakano, M. Goto, *Chem. Commun. (Camb)*. **2009**, 5287.
- [20] S. Selvarajan, N. R. Alluri, A. Chandrasekhar, S. J. Kim, *Biosens. Bioelectron.* **2017**, *91*, 203.
- [21] S. Selvarajan, N. R. Alluri, A. Chandrasekhar, S. J. Kim, *Sensors Actuators, B Chem.* **2017**, *253*, 1180.
- [22] B. Nanogenerator, **2013**, 11016.
- [23] C.-L. Hsieh, R. Grange, Y. Pu, D. Psaltis, *Biomaterials* **2010**, *31*, 2272.
- [24] I. Ron, L. Sepunaru, S. Ltzhakov, T. Belenkova, N. Friedman, I. Pecht, M. Sheves, D. Cahen, *J. Am. Chem. Soc.* **2010**, *132*, 4131.
- [25] P. Thoniyot, M. J. Tan, A. A. Karim, D. J. Young, X. J. Loh, *Adv. Sci.* **2015**, *2*, n/a.
- [26] G. Hwang, J.-M. Kim, D. Hong, C.-K. Kim, N.-S. Choi, S.-Y. Lee, S. Park, *Green Chem.* **2016**, *14*.

- [27] N. C. Maiti, M. M. Apetri, M. G. Zagorski, P. R. Carey, V. E. Anderson, *J. Am. Chem. Soc.* **2004**, *126*, 2399.
- [28] D. Michael Byler, H. M. Farrell, H. Susi, *J. Dairy Sci.* **1988**, *71*, 2622.
- [29] J. Hao, M. J. Han, J. Li, X. Meng, *J. Colloid Interface Sci.* **2012**, *377*, 51.
- [30] L. Riauba, G. Niaura, O. Eicher-Lorka, E. Butkus, *J. Phys. Chem. A* **2006**, *110*, 13394.
- [31] Q. Ma, H. Zhang, W. Liu, J. Ge, J. Wu, S. Wang, P. Wang, *RSC Adv.* **2016**, *6*, 85285.
- [32] H. Hayashi, T. Nakamura, T. Ebina, *J. Phys. Chem. Solids* **2013**, *74*, 957.
- [33] K. K. Lai, R. Renneberg, W. C. Mak, *Green Chem.* **2016**, *18*, 1715.
- [34] J. Sangeetha, J. Philip, *Colloids Surfaces A Physicochem. Eng. Asp.* **2012**, *406*, 52.
- [35] Y. Cai, G. Du, G. Gao, J. Chen, J. Fu, *RSC Adv.* **2016**, *6*, 98147.
- [36] J. U. Lee, W. Lee, S. S. Yoon, J. Kim, J. H. Byun, *Appl. Surf. Sci.* **2014**, *315*, 73.
- [37] Q. Kuang, C. Lao, Z. L. Wang, Z. Xie, L. Zheng, *J. Am. Chem. Soc.* **2007**, *129*, 6070.
- [38] B. Saravanakumar, S. Soyoon, S.-J. Kim, *ACS Appl. Mater. Interfaces* **2014**, *6*, 13716.

- [39] A. O. Elzoghby, W. S. Abo El-Fotoh, N. A. Elgindy, *J. Control. Release* **2011**, *153*, 206.
- [40] F. Patolsky, C. M. Lieber, *Mater. Today* **2005**, *8*, 20.
- [41] N. R. Alluri, S. Selvarajan, A. Chandrasekhar, S. Balasubramaniam, J. H. Jeong, S. J. Kim, *Sensors Actuators, B Chem.* **2016**, *237*, 534.
- [42] S. Selvarajan, N. R. Alluri, A. Chandrasekhar, S. J. Kim, *Sensors Actuators, B Chem.* **2016**, *234*, 395.
- [43] M. Besouw, R. Masereeuw, L. Van Den Heuvel, E. Levtchenko, *Drug Discov. Today* **2013**, *18*, 785.
- [44] *Plant Breed.* **1963**.
- [45] C. J. Gagliardi, C. F. Murphy, R. A. Binstead, H. H. Thorp, T. J. Meyer, *J. Phys. Chem. C* **2015**, *119*, 7028.
- [46] J. L. Hammond, A. J. Gross, P. Estrela, J. Iniesta, S. J. Green, C. P. Winlove, P. G. Winyard, N. Benjamin, F. Marken, *Anal. Chem.* **2014**, *86*, 6748.
- [47] E. Bald, R. Glowacki, J. Drzewoski, *J. Chromatogr. A* **2001**, *913*, 319.
- [48] H. Refsum, P. M. Ueland, S. Kvinnsland, *Cancer Res* **1986**, *46*, 5385.
- [49] V. V. Lemanov, S. N. Popov, G. A. Pankova, *Phys. Solid State* **2011**, *53*, 1191.
- [50] V. S. Bystrov, I. Bdikin, A. Heredia, R. C. Pullar, E. Mishina, A. S. Sigov, A. L.

Kholkin, *Web Source* **2012**, 187.

[51] V. V. Lemanov, *Ferroelectrics* **2000**, 238, 211.

[52] J. Ćulić-Viskota, W. P. Dempsey, S. E. Fraser, P. Pantazis, *Nat. Protoc.* **2012**, 7, 1618.

# CHAPTER VII

## Conclusions and Future Outlook

### 7.1 Conclusions

This chapter describes the overall conclusions of the proposed work in this thesis and suggestions for future work. From the research undertaken, it is evident that BaTiO<sub>3</sub> nanoparticles can be employed for biosensing applications. Moreover, the multifunctional properties of BaTiO<sub>3</sub> nanoparticle are advantageous for developing smart biosensing systems. By the term smart biosensing system, it means integration of more than one device, for example in the proposed work it's the integration of sensor device and piezoelectric nanogenerator for developing self-powered biosensors (both external and internal integration). Further, the findings have paved way for developing solid-state device based biocompatible platform for studying protein-drug interactions and also for proof-of-concept theranostics. All these results prove the multifunctional property of BaTiO<sub>3</sub> nanoparticles and its potential in developing smart biomedical devices for diagnostic purposes. The introduction about the proposed work and the synthesis methodology are given in chapters I and II. Chapter III deals with the glucose biosensing property of BaTiO<sub>3</sub> nanoparticles though non enzymatic method. Stimuli responsive behavior and direct detection of cysteine are briefed in chapter IV. Fabrication of active sensor; internally integrated one stop-device for biomolecule detection is described in detail in chapter V. chapter VI is about the construction of a

solid-state biocompatible electronic platform for elucidating protein-drug interactions and proof-of-concept theranostic studies. Here is the detailed summary of the research undertaken for this thesis work.

Considering the multifunctional property of the BaTiO<sub>3</sub> nanoparticles with special attention towards biological applications, first study was undertaken to develop a self-powered glucose sensor, where the non-enzymatic glucose sensing property of the BT NPs is reported. The main focus in this chapter III is to investigate the semiconducting properties of the BT NPs in sensing glucose. BT NPs synthesized through solid state reaction were used for this study. The change in resistance across the device with the introduction of different glucose concentrations were analyzed through (current-voltage) *I-V* technique. Further, self-powered glucose sensor was realized by external integration of the sensor to that of a piezoelectric nanogenerator.

This preliminary investigation of the BT NPs ability in biosensing further prompted to study its stimuli responsive behavior. The ability of the BT NPs to respond to different stimuli such as pH will be of immense help in developing smart, multifunctional biosensors. Therefore, the NH<sub>2</sub> functionalized BT NPs were employed in detecting Cysteine molecules as discussed in chapter IV. Direct detection of cysteine could have considerable significance over the currently available approaches. In this chapter, investigation on the self-powered cysteine sensor is demonstrated by externally integrating a Ag/BT-NH<sub>2</sub> (Agarose/amine-functionalized BaTiO<sub>3</sub> NPs) film-based cysteine sensor with a piezoelectric nanogenerator (BT/Ag PNG).

As the previous two works were focused on external integration of the sensor and piezoelectric nanogenerator, chapter V describes about the internal integration of the sensor and piezoelectric nanogenerator. Here, a stand-alone, fully integrated, one stop device was used for detecting biomolecule (glucose). Al/BT/ITO piezoelectric nanogenerator (Aluminum (Al)/Barium titanate (BT)/Indium Tin Oxide (ITO) was fabricated as an active biosensor for detecting glucose molecules. The novelty in this work lies in the fact that the active sensor has dual functions both as biosensor and energy harvester. The sensor does not require an external power source for operation rather functions as an active sensor. The piezoelectric output produced from this nanogenerator serves as the energy source as well as the biosensing signal.

Chapter VI deals with the investigation of BT NPs in proof of concept theranostic application. Casein micelle (CAS) based solid-state device through metal-protein-metal electrical junctions designed for elucidating protein-drug interaction as well as proof-of-concept theranostics are the highlights of this chapter VI. This biocompatible electronic platform has multifunctionality, transducing interactions between protein and drug/analyte into electrical signals providing a sophisticated interface between nanoelectronics and biological information processing systems. Agarose biopolymer serves as the matrix for device fabrication in the present work because of its ability to form a three-dimensional network and being inert to biomolecules at the same time serving as an alternate electrode material. The successful conjugation between CAS, cysteamine (CYST; model drug), and amine functionalized Barium titanate nanoparticles (BT NPs) confirmed through current-voltage (*I-V*)

technique complies well with the spectroscopic results. Conjugates pH-responsive behavior and the interaction between CAS and CYST (protein-drug) were confirmed through this multifunctional biosensing platform. Moreover, CAS-CYST conjugate based solid-state device demonstrated a good response to cysteine (CYS) analyte observed through *I-V* curves, led to the realization of proof-of-concept theranostics. Additionally, investigation of the piezoelectric response of the bioconjugates for prospects in the self-powered application was demonstrated using piezoelectric nanogenerator (PNG). All of the above mentioned investigations presented in the thesis provide an unconventional and facile alternative for diagnostic and therapeutic applications.

## 7.2. Suggestions for future work

The present work has laid a foundation for understanding the potential of BaTiO<sub>3</sub> nanomaterial in biological applications especially in developing smart biosensing systems. The study may further pave way for advanced applications such as developing smart implantable biomedical devices as described below.

- Realization of multifunctional nanomaterials like BaTiO<sub>3</sub> in developing smart medical devices.

BaTiO<sub>3</sub> nanomaterial has multifunctionalities including sensing, bio imaging, piezoelectric and semiconducting properties, nanovectors, cytocompatibility, stimuli responsive behavior etc all of which can be utilized for developing such smart devices.

- Development of fully integrated active sensor as one stop device.

Active sensor is the one which functions without an external power supply. Hence, in the proposed work, the device (sensor) itself serves as power source and sensing system (dual functions). This results in one stop device (one device with multifunctionality).

- Development of piezoelectric based nanogenerators as biomechanical energy harvesters *in vivo*.

Piezoelectric nanogenerators can convert any mechanical energy in to electrical energy. Hence, even tiny biomechanical motions inside human body are feasible to be harvested using such devices. These devices can be implanted *in vivo* and the energy as produced can be harnessed.

- Development of biocompatible and biodegradable piezoelectric nanogenerators.

Biocompatible and biodegradable materials are no-brainer when comes to implantable devices. Hence piezoelectric nanogenerators are made / packed with such materials.

- Developing smart diagnostic systems for implantable application.

The term smart implies more than one function such as combination of sensing, energy harvesting, bioimaging etc. Such a device with one-stop solution is highly favourable for implantable devices.

- To realize a biocompatible electronic platform; a single platform with multiple functions such as both diagnosing and therapeutic value (theranostics). Such development will open new avenues for sophisticated interface between

nanoelectronics and biological information processing systems for next generation biomedical devices.

## APPENDIX A: List of Publications

1. **S. Selvarajan**, N. R. Alluri, A. Chandrasekhar and S.J. Kim; *Unconventional active biosensor made of piezoelectric BaTiO<sub>3</sub> nanoparticles for biomolecule detection*; ***Sensors and Actuators B: Chemical*** (IF: 5.401).
2. **S. Selvarajan**, N. R. Alluri, A. Chandrasekhar and S.J. Kim; *Direct detection of cysteine using functionalized BaTiO<sub>3</sub> nanoparticles film based self-powered biosensor*; ***Biosensors and Bioelectronics.***, 2017, **91**, 203–210. (IF: 7.780).
3. **S. Selvarajan**, N. R. Alluri, A. Chandrasekhar and S.J. Kim; *BaTiO<sub>3</sub> nanoparticles as biomaterial film for self-powered glucose sensor application*; ***Sensors and Actuators B: Chemical.***, 2016, **234**, 395–403. (IF: 5.401).
4. Nagamalleswara Rao Alluri, **Sophia Selvarajan**, Arunkumar Chandrasekhar, Saravanakumar Balasubramaniam, Ji Hyun Jeong, Sang-Jae Kim, *Self-powered pH sensor using piezoelectric composite worm structures derived by ionotropic gelation approach*; ***Sensors and Actuators B: Chemical***, 2016, **237**, 534-544. (IF: 5.401)
5. C. Arunkumar, [Nagamalleswara Rao Alluri](#), B. Saravanakumar, **S. Sophia**, [S. J. Kim](#), *Microcrystalline cellulose ingrained polydimethylsiloxane triboelectric nanogenerator as a self-powered locomotion detector*, ***Journal of Materials Chemistry C***, 2017, **5**, 1810-1815. (I.F = 5.2565)
6. Arunkumar Chandrasekhar, Nagamalleswara Rao Alluri, Balasubramaniam Saravanakumar, **Sophia Selvarajan**, Sang-Jae Kim, *Human Interactive*

*Triboelectric Nanogenerator as a Self-Powered Smart Seat*, **ACS applied materials & interfaces**, 2016, 8, 9692-9699. **(I.F = 7.501)**

7. Nagamalleswara Rao Alluri, Arunkumar Chandrasekhar, Venkateswaran Vivekananthan, Yuvasree Purusothaman, **Sophia Selvarajan**, Ji Hyun Jeonga and Sang-Jae Kim, *Scavenging Biomechanical Energy using High-performance, Flexible BaTiO<sub>3</sub> Nanocube/PDMS Composite Films*, **ACS Sustainable Chemistry and Engineering**, 2017, 5, 4730-4738. **(I.F = 5.951)**
8. [Nagamalleswara Rao Alluri](#), [Sophia Selvarajan](#), Arunkumar Chandrasekhar, [Balasubramaniam Saravanakumar](#), [Ji Hyun Jeong](#), [Sang-Jae Kim](#), *Piezoelectric BaTiO<sub>3</sub> /alginate spherical composite beads for energy harvesting and self-powered wearable flexion sensor*, **Composites Science and Technology**, 2017, 142, 65-78. **(I.F = 4.873)**
9. Nagamalleswara Rao Alluri, **Sophia Selvarajan**, Arunkumar Chandrasekhar, Balasubramaniam Saravanakumar, Gae Myoung Lee, Ji Hyun Jeong, Sang-Jae Kim, *Worm structure piezoelectric energy harvester using ionotropic gelation of barium titanate-calcium alginate composite*, **Energy**, (2016) 1146–1155. **(I.F = 4.52)**

#### List of submitted papers

1. **Sophia Selvarajan**, Nagamalleswara Rao Alluri, Arunkumar Chandrasekhar, Sang-Jae Kim; “*Biocompatible electronic platform for monitoring protein-drug interactions with potential in theranostics.*”

## APPENDIX-B: Conference Presentations

1. **Sophia Selvarajan**, Nagamalleswara Rao Alluri, Arunkumar Chandrasekhar, Sang-Jae Kim, “Multifunctional biosensor for monitoring protein-drug interactions with potential in theranostics”. **The 10<sup>th</sup> International Conference on Advanced Materials and Devices (ICAMD 2017)**, December 5-8, 2017, Jeju, Korea. [Poster] **[Best poster award]**.
2. **Sophia Selvarajan**, Nagamalleswara Rao Alluri, Arunkumar Chandrasekhar, Sang-Jae Kim, “Casein Micelle based Biocompatible Electronic Platform for Monitoring Protein-Drug Interactions” **The 4<sup>th</sup> International Conference on Advanced Electromaterials (ICAE 2017)**, November 21-24, 2017, Jeju, Korea. [Poster].
3. **Sophia Selvarajan**, Nagamalleswara Rao Alluri, Arunkumar Chandrasekhar, Sang-Jae Kim, “Piezoelectric nanogenerators for energy harvesting and biosensing applications”, **The 18<sup>th</sup> Korean Micro-Electro-Mechanical Systems Conference (KMEMS)**, March 30- April 1, 2017, Jeju, Korea. [Poster].
4. **Sophia Selvarajan**, Nagamalleswara Rao Alluri, Arunkumar Chandrasekhar, Sang-Jae Kim, “BaTiO<sub>3</sub> film based nanogenerator as a self-powered/active biosensor for glucose detection”, **Materials Challenges in Alternative and Renewable Energy**, February 20-24, 2017, Jeju, Korea. [Poster].
5. **Sophia Selvarajan**, Nagamalleswara Rao Alluri, Arunkumar Chandrasekhar, Sang-Jae Kim, “Self-powered biosensor for direct detection of cysteine using functionalized BaTiO<sub>3</sub> Nanoparticles”, **The 13<sup>th</sup> International Conference on Nanotek and Expo**, December 5-7, 2016, Phoenix, USA. [Poster] **[Best poster award]**.

6. **Sophia Selvarajan**, Nagamalleswara Rao Alluri, Arunkumar Chandrasekhar, Sang-Jae Kim, “Biothiol responsive film based self-powered sensor for non-invasive analysis”, **The 4<sup>th</sup> International Conference on Electronic Materials and Nanotechnology for Green Environment (ENGE)**, November 6 - 9, 2016, Jeju, Korea. [Poster].
7. **Sophia Selvarajan**, Nagamalleswara Rao Alluri, Arunkumar Chandrasekhar, Sang-Jae Kim, “Self-powered reaction based cysteine sensor and its application for sensing in urine sample.” **The 18<sup>th</sup> International Symposium on the Physics of Semiconductors and Applications (ISPSA)**, July 3-7, 2016, Jeju, Korea. [Poster] [**Best poster award**].
8. **Sophia Selvarajan**, Nagamalleswara Rao Alluri, Arunkumar Chandrasekhar, Sang-Jae Kim, “Self-powered glucose sensor based on polycrystalline BaTiO<sub>3</sub> film”. **The 9<sup>th</sup> International Conference on Advanced Materials and Devices (ICAMD)**, December 7-9, 2015, Jeju, Korea. [Oral presentation].
9. **Sophia Selvarajan**, Nagamalleswara Rao Alluri, Arunkumar Chandrasekhar, Sang-Jae Kim, “Nonenzymatic Self-Powered Glucose Sensor based on Polycrystalline thick film of BaTiO<sub>3</sub> Nanoparticles”. **The 3<sup>rd</sup> International Conference on Materials and Reliability (ICMR 2015)**, November 23-25, 2015, Jeju, Korea. [Poster].

## Declaration

I, **SOPHIA SELVARAJAN**, hereby declare that the thesis entitled “**Development of Piezoelectric Barium Titanate Nanoparticles based Smart Biosensing Systems**”, submitted to the Jeju National University, in partial fulfillment of the requirements for the award of the **Degree of Doctor of Philosophy in Department of Advanced Convergence Technology and Science** is a record of original and independent research work done and published by me during the period September 2014 to February 2018 under the supervision and guidance of **Prof. Sang Jae Kim**, Department of Mechatronics Engineering, Jeju National University. This thesis solely based on our publication in reputed journals, and it has not been formed for the award of any other Degree / Diploma / Associateship / Fellowship to any candidate of any University.

**SOPHIA SELVARAJAN**

